The Hashemite Kingdom of Jordan
Scientific Research Support Fund
The Hashemite University

JJEES

Jordan Journal of Earth and Environmental Sciences

Volume (10) Number (3)

JJEES is an International Peer-Reviewed Research Journal

ISSN 1995-6681 jjees.hu.edu.jo September 2019

Jordan Journal of Earth and Environmental Sciences (JJEES)

JJEES is an International Peer-Reviewed Research Journal, Issued by Deanship of Scientific Research, The Hashemite University, in corporation with, the Jordanian Scientific Research Support Fund, the Ministry of Higher Education and Scientific Research.

Editorial Board:

Associate Editorial Board: (Arranged Alphabetically)

International Advisory Board: (Arranged Alphabetically)

Editorial Board Support Team:

Submission address:

Manuscripts should be submitted electronically to the following e-mail:

jjees@hu.edu.jo

For more information and previous issues:

www.jjees.hu.edu.jo

Hashemite Kingdom of Jordan

Scientific Research Support Fund

Hashemite University

Jordan Journal of Earth and Environmental Sciences

JJEES

An International Peer-Reviewed Scientific Journal

Financed by the Scientific Research Support Fund

Volume 10 Number (3)

http:// jjees.hu.edu.jo/

ISSN 1995-6681

Cover page photo: Dead Sea dramatic retreat. Environmental impact of continuous drop of Dead Sea level, by the Geologist Khaled Moumani

المجلة الأردنية لعلوم الأرض والبيئة
Jordan Journal of Earth and Environmental Sciences (JJEES)
http://jjees.hu.edu.jo

Hashemite University

Deanship of Scientific Research

TRANSFER OF COPYRIGHT AGREEMENT

Journal publishers and authors share a common interest in the protection of copyright: authors principally because they want their creative works to be protected from plagiarism and other unlawful uses, publishers because they need to protect their work and investment in the production, marketing and distribution of the published version of the article. In order to do so effectively, publishers request a formal written transfer of copyright from the author(s) for each article published. Publishers and authors are also concerned that the integrity of the official record of publication of an article (once refereed and published) be maintained, and in order to protect that reference value and validation process, we ask that authors recognize that distribution (including through the Internet/WWW or other on-line means) of the authoritative version of the article as published is best administered by the Publisher.

To avoid any delay in the publication of your article, please read the terms of this agreement, sign in the space provided and return the complete form to us at the address below as quickly as possible.

Article entitled:----------

Corresponding author: ----------

To be published in the journal: Jordan Journal of Earth & Environmental Sciences (JJEES)

I hereby assign to the Hashemite University the copyright in the manuscript identified above and any supplemental tables, illustrations or other information submitted therewith (the "article") in all forms and media (whether now known or hereafter developed), throughout the world, in all languages, for the full term of copyright and all extensions and renewals thereof, effective when and if the article is accepted for publication. This transfer includes the right to adapt the presentation of the article for use in conjunction with computer systems and programs, including reproduction or publication in machine-readable form and incorporation in electronic retrieval systems.
Authors retain or are hereby granted (without the need to obtain further permission) rights to use the article for traditional scholarship communications, for teaching, and for distribution within their institution.

☐ **I am the sole author of the manuscript**

☐ **I am signing on behalf of all co-authors of the manuscript**

☐ **The article is a 'work made for hire' and I am signing as an authorized representative of the employing company/institution**

Please mark one or more of the above boxes (as appropriate) and then sign and date the document in black ink.

Signed:_____ **Name printed:** _____

Title and Company (if employer representative) : _____

Date: _____

Data Protection: By submitting this form you are consenting that the personal information provided herein may be used by the Hashemite University and its affiliated institutions worldwide to contact you concerning the publishing of your article.

Please return the completed and signed original of this form by mail or fax, or a scanned copy of the signed original by e-mail, retaining a copy for your files, to:

Deanship of Scientific Research
The Hashemite University P.O. Box 150458, P.C.13115, Zarqa, Jordan
Tel.: 00962 53903333/ Ext. 4235
Fax: 00962 53826823
E-mail: jjees@hu.edu.jo

Subscription

Jordan Journal of Earth & Environmental Sciences (ISSN 1995-6681)
An International Peer- Reviewed Research Journal
Published by the Deanship of Scientific Research - The Hashemite University

Name:	الاســـــــــــم:
Specialty:.....	التخصـــــــــص:
Address:.....	العنـــــــــوان:
P.O. Box:.....	صنـــدوق البريـــــد:
City & Postal Code:	المدينة: الرمز البريدي:
Country:.....	الـــــــــــدولة:
Phone:.....	رقـــم الهاتـــــف:
Fax No:.....	رقـــم الفاكـــــس:
E-mail:.....	البريـــد الإلكترونـــي:
Method of payment:	طريقـــــة الدفـــع:
Amount Enclosed:.....	المبلـــغ المرفـــق:
Signature:.....	التوقيـــــــــع:

Cheques should be paid to Deanship of Research - The Hashemite University

I would like to subscribe to the Journal:

For

- ☐ One year
- ☐ Two years
- ☐ Three years

One year Subscription Rates

	Inside Jordan	Outside Jordan
Individuals	10JD	70$
Students	5JD	35$
Institutions	20JD	90$

Correspondence

Subscriptions and sales:

Professor Fayez Ahmad
Deanship of Scientific Research
The Hashemite University P.O. Box 150458, P.C.13115, Zarqa, Jordan
Tel.: 00962 53903333/ Ext. 4235
Fax: 00962 53826823
E-mail: jjees@hu.edu.jo

JJEES
Jordan Journal of Earth and Environmental Sciences

JJEES

JJEES (2019) 10 (3): 127-135
ISSN 1995-6681

Jordan Journal of Earth and Environmental Sciences

A Regional Study of Frequency Maximum Daily Flows of the Upper Senegal River Basin (Guinea, Mali, Senegal and Mauritania)

Cheikh Faye

Assane Seck University of Ziguinchor, Department of Geography, Senegal.

Received 4 February 2019; Accepted 21 April 2019

Abstract

Frequency analysis of extreme events is among the preferred tools for estimating flood flows and their return periods. In a frequency analysis, the observations must be independent and identically distributed. These assumptions are not often respected, and the parameters of the frequency distributions to be adjusted are time-dependent or co-variable. The objective of this article is to make a statistical analysis of the maximum daily flow of six hydrometric stations located in the upper Senegal River basin. Four frequency distributions were thus retained in this analysis and adjusted in conjunction with the maximum daily flow: the generalized extreme value frequency distribution (GEV), the Pearson type 3 frequency distribution, the Gumbel frequency distribution, and the Log-normal frequency distribution. The comparison between these distributions was ensured through the calculation of adjustment indices, the robustness of simulation method, the visual test, and particularly the chi-square test. The results from the four methods are not significantly different. However, after classifying the frequency distributions, the statistical quality of the adjustment was taken into account. Thus, the Pearson type 3 frequency distribution was chosen to estimate the maximum flow quantiles in the upper Senegal River basin for different return periods.

Keywords: annual maximal flow, statistical adjustment, frequency analysis, estimation, Senegal River basin

1. Introduction

The extreme values are often the maxima of a certain quantity over a given period, characterized either by maximum values (flood) or minimum values (low water). Floods are most often described by three main characteristics: peak, volume, and duration. There has been a renewed interest in research and studies of floods over the last decades. This can be explained by the concerns of the scientific community and decision-makers regarding the increasingly high frequency of the appearance of devastating floods (Meddi and Abbes, 2014). In many studies, this is linked to climate change (Burn, 1998; Vastila et al., 2010; Roy et al., 2001). The effect of climate change on hydrological variables related to extreme events (maximum annual rainfall, maximum annual flow, etc.) can be done by studying the existence of trends in the series observed, or by analyzing the dependence variables studied with other climate variables or indices, called covariates (Katz, 1999).

There are various approaches to studying and predicting floods. Below is the typology proposed by Lang and Lavabre (2007):

- Statistical processing performed on observed flow samples to determine given return period rates.
- Empirical formulations based on observed flow samples to determine volume and duration.
- The use of deterministic transfer and production functions (e.g. the Soil Conservation Service (SCS) method and rational method).

The statistical treatment of hydrometric data is the preferred approach for hydrologists to analyze the risk associated with extreme hydrologic events. Thus, many frequency distributions are often applied in different parts of the world to estimate quantiles of maximum flow rates. Among these frequency distributions are the frequency distribution of Gumbel long used in Algeria, the frequency distribution of the extreme values generalized (GEV) in Great Britain, the Lognormale frequency distribution in China, the frequency distribution Log-Pearson type III (LPIII) in the United States, the Lognormale frequency distribution in the Chéllif basin in Algeria, and the Gamma frequency distribution in Spain (Meddi and Abbes, 2014).

The Senegal River basin (the valley and the delta in particular) is periodically affected by floods and floodings. These extreme events (devastating floods) punctuate the climatic variability which acts directly on the national economy, because of the low level of control of the waters and the bad conditions of the filling of the reservoirs. The city of Saint Louis (in Senegal), located in the delta, has undergone the effects of large and repeated floods. Significant floods and overflows of the Senegal River are indicated in travelers' accounts, historical documents, and ancient maps well before 1903 (beginning of the first measurements of water depth). The major recorded floods are those of 1827, 1841, 1843, 1853 (Kane, 2002), resulting in extremely large overflows of the river to the point that homes were full of water up to the first floor (Hardy, 1921). In the Senegal River basin, water resources can become a problem because of their

* Corresponding author e-mail: cheikh.faye@univ-zig.sn

overabundance as was the case with the devastating floods of 1890, 1906, and 1950 (Roche, 2003); hence, their studies are of great importance.

Flood hazard studies provide decision-makers in the planning field with the necessary elements for decision-making. The methods of regional frequency analysis make it possible to estimate, for a given site, and on the basis of the regional information, the quantiles of period of return. These studies are very often used for the design and sizing of hydraulic structures such as water retaining structures, anti-erosion structures, and sewerage networks (Onibon et al., 2004). They are also used more generally to allow an overall description of the characteristics of the spatial structure of the different hydrological phenomena in a region. They were initially developed for the estimation of flood flows (Cunnane, 1988, Ouarda et al., 2001). For the purposes of hydraulic modeling, these studies include the estimation of extreme flood flows corresponding to the return periods of 25, 50, and 100 years, respectively representing high, medium and low recurrences (Meddi and Abbes, 2014). Estimations of extreme event flows are a topic of growing interest in water sciences.

Prior to the statistical modeling of series, it is taken for granted that the following approaches are detrmined (1) the way of constituting a sample, (2) a frequency distribution, (3) a method of estimating parameters and quantiles and (4) a scheme that allows the joint use of local and regional data (WMO, 1989). For the constitution of the samples, one can retain either the maximum values of each year, or all the data above a previously fixed threshold, and for a given time step (Ferrier, 1992). The methodology based on the choice of maximum values for each year is generally preferred by both researchers and designers (Cunnane, 1987) because it is easier to apply and is often more statistically effective. For these reasons, it was also maintained in this analysis. This article is interested in finding a frequency distribution capable of accounting for the maximum daily discharge regime, and the estimation of parameters and quantiles for the prevention of flood risks. Thus, the main objective is to find a theoretical frequency distribution that can show a good presentation of the distribution function of the studied process. Also, this study shows how to adjust several frequency distributions from the maximum flows in the basin and choose the best one, that is the most suitable to evaluate the quantiles of the flood flows through the visual test (graphical quality of adjustment) and the chi test.

2. Study area

The Senegal River, some 1,700 km long, drains a basin of 300,000 km^2, straddling four countries that are upstream, downstream, namely Guinea, Mali, Senegal, and Mauritania (Figure 1). It ranges from 10° 20 'to 17° N and from 7° to 12° 20' W and is made up of several tributaries; the main ones being Bafing, Bakoye and Falémé which take their sources in Guinea and form the top basin (OMVS / GEF / BFS Project, 2008) (Figure 1). The Senegal River thus formed by the junction between Bafing and Bakoye, receives the Kolimbiné then Karokoro on the right and Falémé on the left, 50 km upstream of Bakel. In the southern part of the basin, the density of the surface hydrographic network testifies to the impermeable nature of the terrain (Michel, 1973; Rochette, 1974).

Like the entire intertropical band, the Senegal River basin has experienced a climate upheaval since the 1970s (Faye, 2013). The various studies on this basin have already shown the effects of climate change with changes in its hydrological regime from 1970 (Hubert et al., 1989; Dione 1996; Nicholson et al., 2000; Ardoin-Bardin, 2004; Sow, 2007; Faye, 2013 ; 2015; Faye et al., 2015a; Faye et al., 2015b; Faye, 2017). To remedy the effects of climate change and cope with the changes in its hydrological regime, a set of developments (Diama and Manantali) was started, completely transforming the hydrological dynamics of the Senegal River basin.

The basin is generally divided into three entities: the upper basin, the valley, and the delta which are strongly differentiated by their topographical and climatological conditions. The upper basin, the current study area, extends from the sources of the Senegal River (Fouta Djalon) to the confluence between the Senegal River and Falémé (downstream of Kayes and upstream of Bakel). It is roughly made up of the Guinean and Malian parts of the river basin, and provides almost all of the water supply (more than 80 % of the inflow) from the river to Bakel because it is relatively wet (OMVS / FEM / BFS project, 2008). Rain falls between April and October in the mountainous part of the extreme south of the basin, especially in the Guinean part of the basin, and causes the annual flood of the river which takes place between July and October.

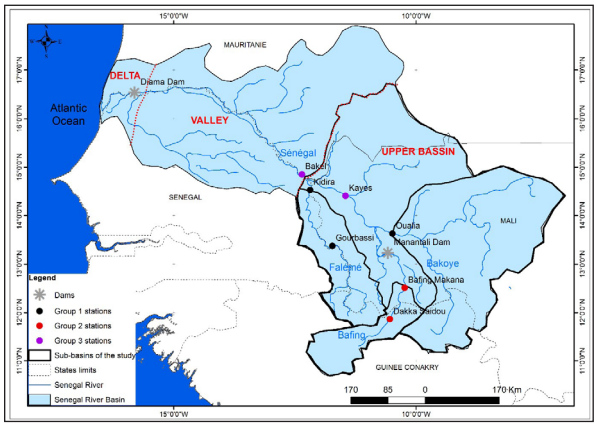

Figure 1. Location of the Senegal River basin and its Upper basin

3. Data and Methods

3.1. Data

The database of stations in the upper Senegal River basin to be maintained for this study should contain a series of daily flows which meet two important criteria: the length of the chronicles on the one hand (cover the largest period of time possible), and the quality of data on the other hand (the least possible missing data). This has been the case at the six stations selected for this study. The hydrometric data in this study were provided by the Senegal River Development Organization (OMVS). These data concern the daily flows (from 1950 to 2014) from which the annual daily maximum flows are calculated. Figure 2 shows the evolution of the maximum instantaneous flow rates observed for the selected stations.

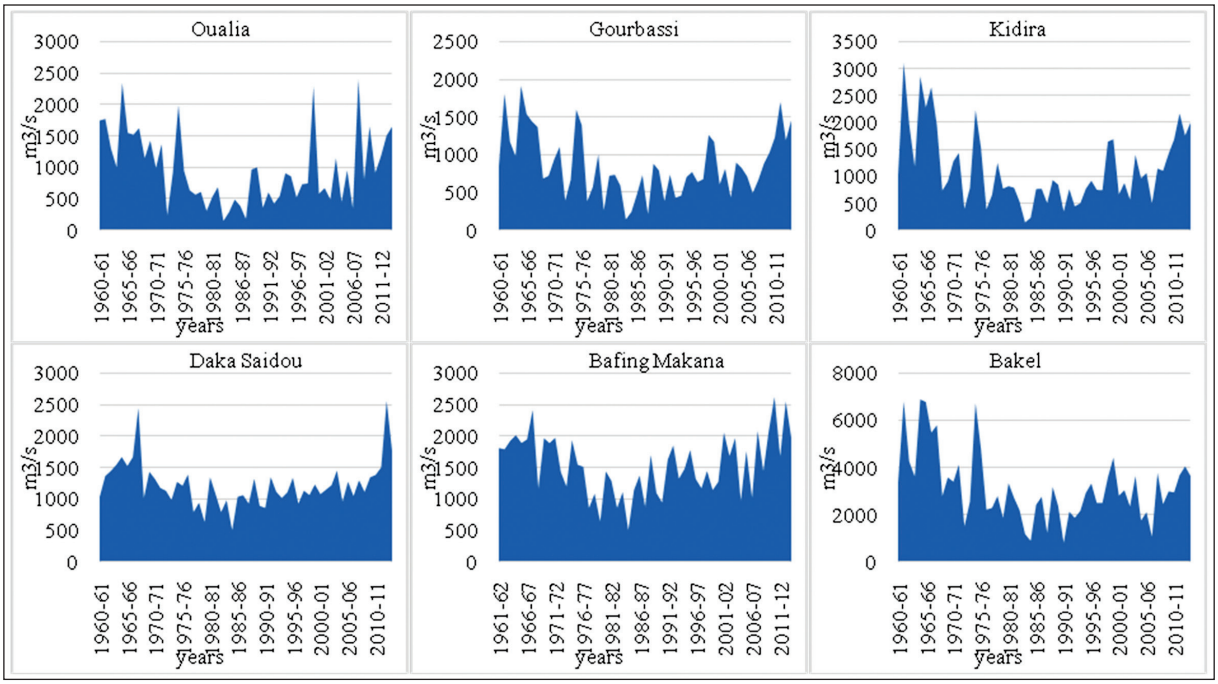

Figure 2. Evolution of annual maximum daily discharges of stations selected in the upper Senegal River basin

3.2. Methods

3.2.1. Statistical Homogeneity Test by Principal Component Analysis

Principal component analysis (PCA) is a statistical technique used (Faye, 2014; Baba-Hamed and Bouanan, 2016) to reduce the number of variables to those that are most significant among a set of variables. It is used to find a link between variables and individuals in order to group them into homogeneous regions. One of the objectives of the PCA is to obtain useful information from a data matrix, and to provide a graphical representation of the data to facilitate analysis. The mathematical procedure of principal component analysis is in fact a multivariate statistical method that serves as a data processing. In this study, all the modules for stations of the upper Senegal River basin were submitted to the principal component analysis in order to determine the affinities between these sub-basins.

3.2.2. Statistical Frequency Distributions for Frequency Analysis of Extreme Flows

Frequency analysis of extreme flows is a statistical analysis that consists of predicting the probability of occurrence of an event of a given importance based on the knowledge of past events, that is flow measurements recorded during a chronicle of several years. In this sample, it is, then, a question of selecting the relevant events which will serve to establish a statistical frequency distribution to represent the studied phenomenon at best. There are different ways to calculate the variables of a theoretical frequency distribution to fit on a sample (Ruf, 2004). The methods used here are those of the moments and that of the maximum likelihood. In this study, the following frequency distributions are used (Table 1):

- Generalized Extreme Value (GEV) frequency distribution: The GEV distribution is recommended for flood studies because it gives good adjustments to the series.
- Gumbel's frequency distribution (doubly exponential frequency distribution): It is adapted to the study of the maximum value of a variable having many achievements over a period (for example by studying floods above a threshold).
- Pearson type 3 frequency distribution: It adjusts easily, but sometimes gives too low probability to a high flood; it works here for the study of variables with positive skewness.
- Log normal frequency distribution: It is recommended by some hydrologists who justify it by the fact that a hydrological event is the result of a large number of factors. The normal log frequency distribution works particularly well when there is a complex varied diet and when there is no regularity of the diets.

Table 1. Probability Density Function of Selected frequency distributions

Frequency distribution	Probability density function	Parameters
GEV	$f(x)=\frac{1}{\alpha}\left[1\frac{k}{\alpha}(x-u)\right]^{\frac{1}{k}-1}\exp\left[-\left[1\frac{k}{\alpha}(x-u)\right]^{\frac{1}{k}}\right]$	α, u, k
Gumbel	$f(x,\alpha,u)=\frac{1}{\alpha}\exp\left[-\left[-\frac{x-u}{\alpha}-\exp\left(-\frac{x-u}{\alpha}\right)\right]\right]$	α, u
Log normal	$f(x,\alpha,u)=\frac{1}{x\sigma\sqrt{2\pi}}exp\left[\frac{[Lnx-u]^2}{x\sigma^2}\right]$	u, σ
Pearson type 3	$f(X)=\frac{\alpha^{\lambda}}{\Gamma}e^{-\alpha(x-m)}(X-m)^{\lambda-1}$	α, λ, m

k: shape parameter; α: scale parameter; μ:location parameter; m: the original parameter $m \leq X \leq \infty$; $\lambda > 0$; λ: the shape parameter; X: a random variable

Many techniques exist to compare the four methods of analysis of the frequency distributions of probability and to choose the best one. The chi-square adequacy test has been adopted and remains a good way to judge the quality of an adjustment. Since tests are tools used to facilitate decision-making, they can sometimes help separate two models, but most often, they show comparable results for two well-adjusted frequency distributions (Habibi et al., 2013).

3.2.3. Definition of a Flow Calculation Tool

From the results, an attempt has been made to establish a general flow calculation formula accepted by many authors (Ruf, 2004). For a given frequency, the flood discharge of a watercourse has its logarithm, which increases linearly according to that of the drained surface:

$$Q = A.S^n \quad or$$
$$Log\ Q = Log\ A + n\ Log\ S$$

This simple formula chosen therefore only considers the factors A and n which will be representative of the basin as well as its surface S. The factors A and n may still vary according to the geographical position of the basins which will vary, among others, the abundance of precipitation. This formula will be tested on the decennial flows and the centennial flows to define a preliminary tool of the study of the extreme flows.

4. Results and Discussion

4.1. Establishment of Groups of Stations and Homogeneity Tests

For the decomposition of the study area into homogeneous groups of stations, the principal component analysis that was used allowed the upper basin to be subdivided into homogeneous groups of stations. Thus, three main groups stand out and provide a better understanding of the spatiotemporal dynamics of the functioning of the hydrosystem of the upper Senegal River basin (Table 2 and Figure 3).

- Group 1 consists of natural (uncontrolled) reaches of Faleme (at Gourbassi and Kidira) and Bakoye (at Oualia);
- Group 2 is composed of the natural reaches of the Bafing upstream of the Manantali dam (in Dakka Saidou and Bafing Makana);
- Group 3 consists of the semi-artificialized reach after the confluence of Bafing, Bakoye and Falémé (in Kayes and Bakel).

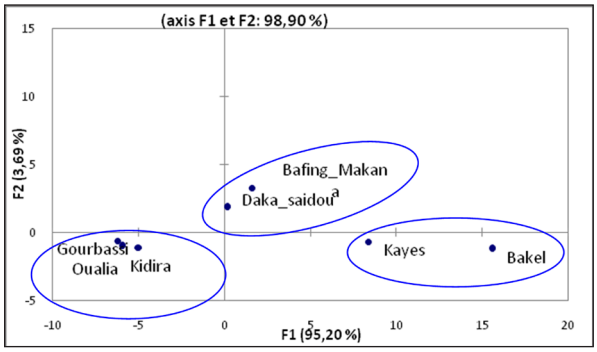

Figure 3. Homogeneity test of different groups compared

Table 2. Results of the homogeneity test of the different basins

regions	basins	Stations	Area km2	Module m³/s	FMAX m³/s	Axis 1	Axis 2
Group 1: natural diversions (uncontrolled)	Bakoye	Oualia	84700	118	945	-5.92	-1.01
	Falémé	Gourbassi	17100	108	863	-6.22	-0.64
		Kidira	28900	140	1149	-4.96	-1.09
Group 2: upstream reaches dam	Bafing	Dakka Shelpou	15700	233	1236	0.19	1.83
		Bafing Makana	22000	258	1549	1.61	3.27
Group 3: semi-artificialized bays	Senegal	Kayes	157400	436		8.36	-0.70
		Bakel	218000	597	3173	15.6	-1.21

In this distribution, the basins of the third group (made up of the Senegal River basin) stand out clearly from the basins of the other groups because of their larger surface area (157400 km² in Kayes and 218000 km² in Bakel) and, therefore, their largest flow past average (436 m³/s at Kayes and 597 m³/s at Bakel). In return, the basins of the second group (composed of the sub-basins of the Bafing upstream of Manantali) are distinguished from those of the first group because of a larger flow elapsed (233 m³/s in Dakka Saidou and 258 m³/s to Bafing Makana) related to their more southern position. The situation of the basins of the first group, which isolates themselves, is attributed to their lower flow (108 m³/s Gourbassi and 140 m³/s and Kidira on the Falémé, 118 m³/s in Oualia on the Bakoye).

4.2. Application and Choice of the Best Frequency Distribution for Maximum Flows

After the establishment of homogeneous groups, the identification of a regional distribution probability frequency distribution, which is better suited to the annual peak flow series of the stations in each group, was made using the chi-square test (Table 3). This also makes it possible to evaluate the impact of the exclusive use of frequency distributions such as Gumbel and Log Normale in civil engineering and hydraulic engineering studies (Meddi and Abbes, 2014).

Table 3. Values of the p-value on the four models applied with the chi-square test

regions	stations	GEV	Gumbel	Normal Log	Pearson type III
Group 1	Oualia	<0.0001 *	.6338	<0.0001 *	<0.0001 *
	Gourbassi	0.0011 *	.6338	<0.0001 *	0.0002 *
	Kidira	<0.0001 *	.6338	<0.0001 *	<0.0001 *
Group 2	Dakka Saidou	<0.0001 *	.6338	<0.0001 *	<0.0001 *
	Bafing Makana	.9586	.6338	<0.0001 *	<0.0001 *
Group 3	Bakel	<0.0001 *	.6338	<0.0001 *	<0.0001 *

** significant test (risk of error of 0.05)*

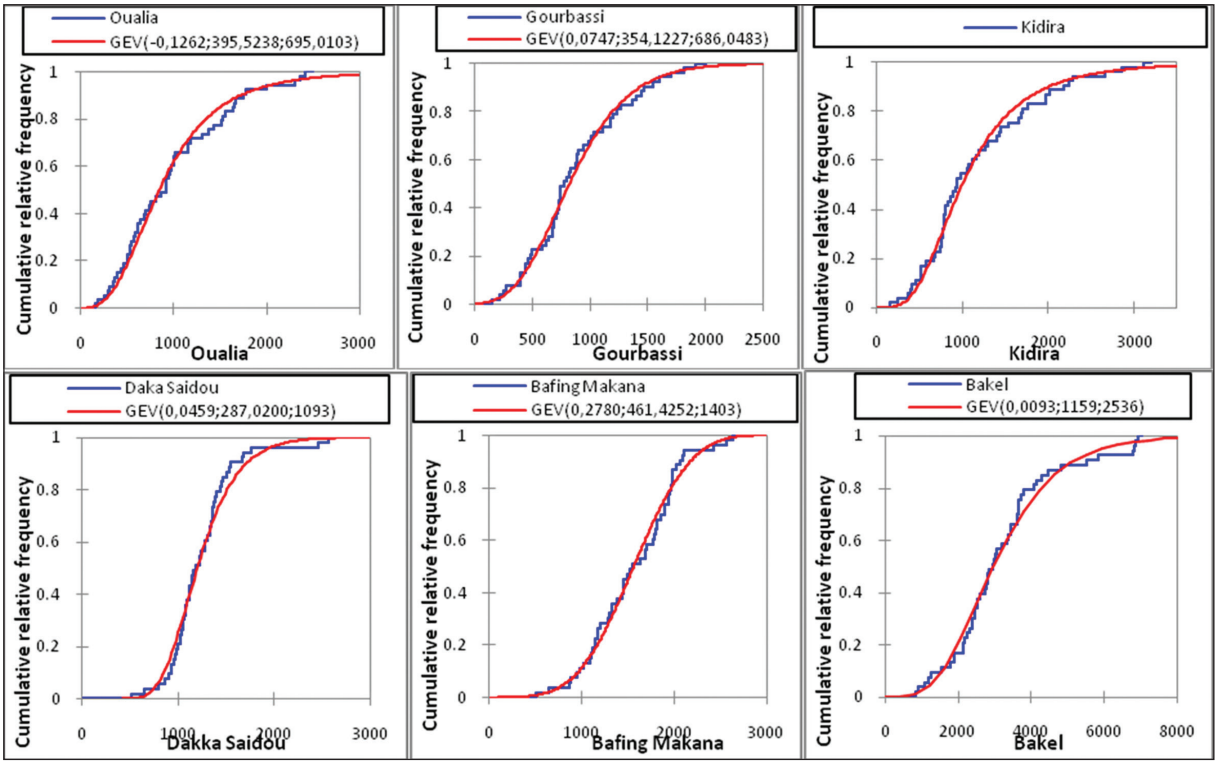

Figure 4. Observed and Simulated Values of the GEV Distribution Function Applied to Annual Daily Maximum Flows in the Upper Senegal River Basin from 1960 to 2014

Of the four distributions considered by visual examination, the frequency distributions of Normal Log, Pearson Type 3, and GEV are well adjusted to the values of the maximum daily flow rates of the six stations and have the advantage of being model simple frequencies, evidenced by the values of p-values which are less than the risk of error of 0.05. These frequency distributions are the distributions of which the adjustment to the regional data of three groups is the most satisfactory. In addition, they are more suitable for estimating quantiles of flood flows in the basin compared to Gumbel's frequency distribution whose p-values are all greater than 0.05 (Table 3). Indeed, the hypothesis of Gumbel's frequency distribution for the six series studied is therefore rejected at the level of significance of 5 %. One of the three frequency distributions that gave the best adjustment of the daily maximum hydrometric series of the stations of the upper watershed of the Senegal River, through the visual test (graphic quality of adjustment) and the chi-square test is the GEV frequency distribution presneted in Figure 4. The results of the frequency distributions of Lognormal, Pearson type 3 and GEV, therefore, allow the estimation of flow quantiles at sites for which no measurement is available (Onibon et al., 2004).

4.3. Estimation of the Parameters of the Distribution Functions

In Tables 4, 5, and 6, the estimated values of the distribution function parameters at the maximum annual flow rates are recorded for each of the three best fit models described above. Of these four frequency distributions usually applied to the study and the frequency analysis of the maximum daily flows, the generalized frequency distribution of the GEV extremes and the Pearson type 3 frequency distribution have three parameters each; those of the extreme values (Gumbel and normal log) have two only. By way of illustration, the maximum likelihood method is used to estimate the parameters of the GEV frequency distribution, while that of the moments is used to estimate the parameters of the normal Log frequency distribution and that of Pearson type 3.

Table 4. Parameter Values estimated by the Maximum Likelihood Method of the GEV frequency distribution

Parameters	Oualia	Gourbassi	Kidira	Daka Saidou	Bafing Makana	Bakel
k	-0,12	0,07	-0,16	0,04	0,27	0,009
beta	395	354	427	287	461	1159
μ	695	686	827	1092	1402	2536

Table 5. Parameter Values estimated by the Moment Method of the Normal Log frequency distribution

Parameters	Oualia	Gourbassi	Kidira	Daka Saidou	Bafing Makana	Bakel
μ	6.69	6.63	6.88	7.08	7.30	7.96
σ	0.64	0.55	0.62	0.27	0.33	0.48

Table 6. Parameter values estimated by the moment method of the Pearson type 3 frequency distribution

Parameters	Oualia	Gourbassi	Kidira	Daka Saidou	Bafing Makana	Bakel
k	2.86	4.23	2.88	12.0	11.2	4.62
beta	340	204	401	102	139	691

Although several authors in the literature have recommended the use of the General Extreme Value (GEV) frequency distribution for the regional frequency analysis of extreme rainfall events (Sveinsson et al., 2002), in this study, the Pearson type 3 has been favored in the search for the best result to model the distribution of the extreme flood flows of the stations of the basin.

4.4. Frequency Analysis of Annual Maximum Daily Flows

As stated in the introduction, the central objective of this study is the development of a regional frequency analysis method for extreme flows. This section is devoted to the presentation of the results of the application of the procedure proposed above for the estimation of the quantiles associated with the annual maximum daily discharges of the stations of each group. After classifying these frequency distributions, based on the criteria of posterior probability, the Pearson type 3 frequency distribution was selected to model annual maximum flow rates. Thus, for each station, the return period quantiles are calculated, using the parameters of the Pearson type 3 frequency distribution (Table 7 and Figure 5).

Table 7. Frequency Flow Values of annual daily peak flows in the upper basin of the Senegal River from 1960 to 2014 following the distribution of Pearson type 3

Stations	Return period (in years)							
	1	2	5	10	20	50	100	200
Oualia	616	1090	1556	1867	2158	2524	2791	3052
Gourbassi	629	977	1309	1525	1725	1973	2153	2326
Kidira	736	1299	1871	2258	2623	3083	3421	3750
Dakka Saidou	998	1334	1641	1835	2011	2198	2380	2549
Bafing Makana	1305	1698	2043	2196	2516	2701	2829	3067
Bakel	2256	3522	4764	5584	6348	7300	7990	8662

The estimation of extreme flows corresponding to quantiles of return periods are commonly used in hydrology (Onibon et al., 2004). The annual discharge series of the basin have been adjusted to different statistical frequency distributions, and the Pearson type 3 frequency distribution presents the best fit for all the stations studied in the basin by the graphical method. However, the estimates often introduce a gap that is characterized by underestimation or overestimation of quantiles. The Pearson type 3 frequency distribution fitted better to a series of asymmetry coefficients and the standard values and the frequency distribution results show a better intensity of the bond. On the other hand, even though Gumbel's frequency distribution is one of the two most used frequency distributions in hydrology (with the normal frequency distribution), it could not model the series of maximum annual flow rates because it was rejected at the first stage of its application. Considered to model the extreme flows, the good estimates of the annual maximum flow rates by the Pearson type 3 frequency distribution can help managers and engineers in the dimensioning of the hydraulic structures as well as the management of the risks. These results are in concordance with those from Riad et al. (2006) in Morocco and López and Francés (2012) in Spain where the Gamma frequency distribution (or Pearson type 3) is better adapted to model annual maximum flow rates. These results also confirm those found by Meddi and Abbes (2014) for some Algerian watersheds.

4.5. Implementation of a Flow Calculation Tool

Based on the results, a general formula for calculating discharge rates on decadal frequency and centennial frequency flows has been tested to obtain a preliminary tool for the study of extreme flows (Ruf, 2004). All the stations studied, which have a hydrological significance because of their extended time of observation and the validity of their calibration curves in the studied domains, have been represented (Figure 6).

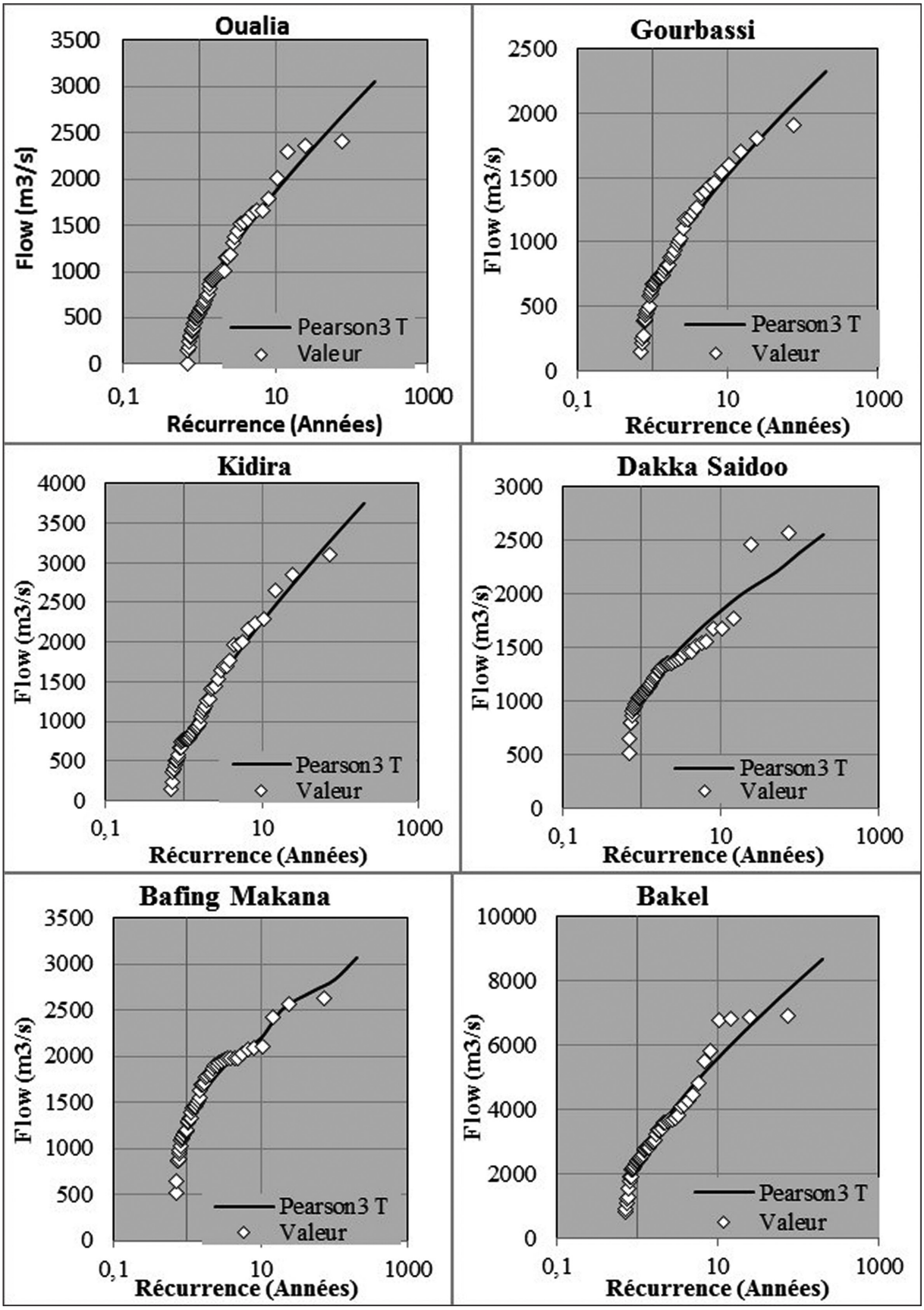

Figure 5. Statistical Adjustments to the Pearson Type 3 Distribution of Annual Maximum Daily Flows in the Upper Senegal River Basin from 1960 to 2014

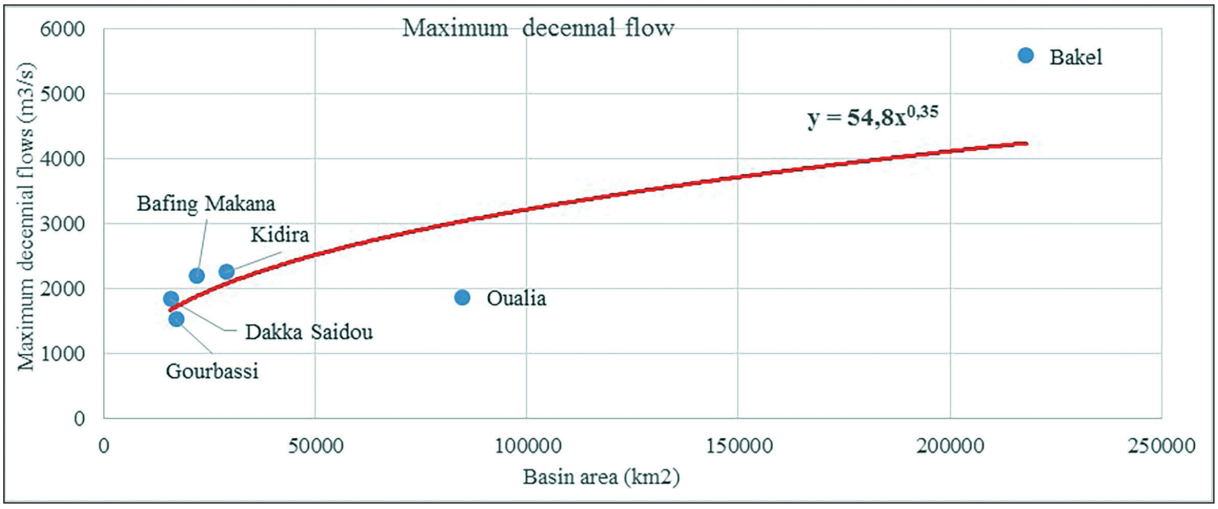

Figure 6. Variation of the maximum decadal flow according to the surface of the basin

Compared to the variation of the maximum decadal discharge according to the surface of the basin, and unlike the other stations of the high basin, the stations of Bakel and Oualia are not disperesed on the trend of the curve. However, these envelope curves could be used as a tool for estimating flows on ungauged basins in Senegal; the general formula is as follows:

$y = 54.8\ x^{0.35}$

These tools are general, and characterize general phenomena. Moreover, they can be used as approximation tools which must be taken with the necessary precautions with regard to their accuracy (Ruf, 2004). They can however be useful during a pre-study for example. Finally, although the estimates are correct despite the remaining errors on the calibration curves (measurement errors), the irregularity of the African tropical regimes does not make us immune to major errors in the major watersheds.

5. Conclusions

The main focus of this work was to find a frequency model capaable of accounting for the regime of extreme flows of the upper watershed of the Senegal River. The basin is subdivided into three homogeneous zones or groups in terms of the average annual flows elapsed. The statistical estimation of extreme flood flows can be done in two ways: the annual maxima method and the values above a threshold method. Based on the length of the series, the first approach was chosen. One of the drawbacks of this procedure is the choice of an insignificant event when no significant flood is recorded during a hydrological year (Meddi and Abbes, 2014). The usual distributions used to adjust the maximum daily flow rates: GEV, the Gumbel, Log normal and Pearson type 3 have given similar results (between GEV, Log normal and Pearson type 3 which are more suitable for the test. on the stations of the three groups), and sometimes different results (using Gumbel compared to the other frequency distributions). From the results of the graphical visual criterion and the chi-square test, it appears that the maximum daily flow rates of the six hydrometric stations preferentially follow the Pearson type 3 frequency distribution, followed closely by the GEV and Normal log. As for Gumbel's frequency distribution, it was not able to model the annual maximum flow series and the high values tended to be overestimated or underestimated. After the classification of the frequency distributions, and based on the criteria of the posterior probability, the selected Pearson type 3 frequency distribution made it possible to model the annual maximum flows and to calculate the quantiles of the period of return. The decennial and centennial frequency rates obtained provided the means, from a power equation, to define the preliminary tool for estimating decennial and centennial flows on Senegal's ungauged basins.

References

Ardoin-Bardin, S. (2004). Variabilité hydroclimatique et impacts sur les ressources en eau de grands bassins hydrographiques en zone soudano sahélienne. Thèse de doct. Univ. Montpellier II. 440 p.

Baba Hamed, K.n and Bouanan, A. (2016). Caractérisation d'un bassin versant par l'analyse statistique des paramètres morphométriques : Cas du bassin versant de la Tafna. (Nord-ouest algérien). Geo-Eco-Trop., 40, 4 : 277-286.

Burn, D.H., (1998). Climatic Change Impacts on Hydrologic Extremes and the implications for reservoirs. Dans Proceedings of the II International Conference on Climate and Water, 1, 2aI, 273-281.

Cunnane, C. (1987). Review of Statistical Models for Flood Frequency Estimation Paper pres. In : Inst. Symp. on Flood Frequency and Risk Analysis. Baton Rouge. La., Publ. in Singh, V.P. (Ed.), Hydrologie Fréquency Modelling, Reidel Publ. Co., Dordrecht : 49-95.

Cunnane, C. (1988). Methods and merits of regional flood frequency analysis. J. Hydrol. 100, 269–290.

Dione, O. (1996). Evolution climatique récente et dynamique fluviale dans les hauts bassins des fleuves Sénégal et Gambie. Thèse de doctorat, Université Lyon 3 Jean Moulin, 477 p.

Faye, C. (2013). Evaluation et gestion intégrée des ressources en eau dans un contexte de variabilité hydroclimatique : cas du bassin versant de la Falémé. Thèse de Doctorat, Université Cheikh Anta Diop de Dakar, 309 p.

Faye, C. (2014). Méthode d'analyse statistique de données morphométriques : corrélation de paramètres morphométriques et influence sur l'écoulement des sous-bassins du fleuve Sénégal. Cinq Continents, 4(10), 80-108.

Faye, C. (2015). Caractérisation des basses eaux : les effets durables du déficit pluviométrique sur les étiages et le tarissement dans le bassin du Bakoye. Espaces et Sociétés en Mutation (Numéro Spécial), 109-126.

Faye, C. (2017). Variabilité et tendances observées sur les débits moyens mensuels, saisonniers et annuels dans le bassin de la Falémé (Sénégal), Hydrological Sciences Journal – Journal des sciences hydrologiques, 62 (2), 259 à 269.

Faye, C., Diop, E.S., Mbaye, I. (2015a). Impacts des changements de climat et des aménagements sur les ressources en eau du fleuve Sénégal : caractérisation et évolution des régimes hydrologiques de sous-bassins versants naturels et aménagés. Belgeo, 4, 1-22.

Faye, C., Sow, A.A., Ndong, J.B. (2015b). Étude des sècheresses pluviométriques et hydrologiques en Afrique tropicale : caractérisation et cartographie de la sècheresse par indices dans le haut bassin du fleuve Sénégal. Physio-Géo - Géographie Physique et Environnement, 9, 17-35.

Ferrier, J.P. (1992). Analyse statistique de pluies maximales journalières. Comparaison de différentes méthodes et application au bassin Guadalhorce (Espagne). Hylrol. continent., 7 (1), 23-31.

Habibi, B., Meddi, M., Boucefiane, A. (2013). Analyse fréquentielle des pluies journalières maximales Cas du Bassin Chott-Chergui. Revue « Nature & Technologie ». C- Sciences de l'Environnement, 08, 41-48.

Hardy, G. (1921). La mise en valeur du Sénégal de 1817 à 1854. Paris, Larose, 376 p.

Hubert, P., Carbonne, J.P., Chaouche, A. (1989). Segmentation des séries hydrométéorologiques. Application à des séries de précipitations et de débits de l'Afrique de l'Ouest. Journal of Hydrology, 110, 349-367.

Kane, A. (2002). Crues et inondations dans la basse vallée du fleuve Sénégal. Gestion intégrée des zones inondables tropicales, IRD Éditions, 2002, 197-208.

Katz, R.W. (1999). Extreme value theory for precipitation: sensitivity analysis for climate change. Adv. Water Resour., 23, 133-139.

Lang, M., and Lavabre, J. (2007). Estimation de la crue centennale pour les plans de prévention des risques d'inondations. Versailles, Editions Quae, 2007. 152 p.

López, J., and Francés, F. (2012). Non-stationary flood frequency analysis in continental Spanish rivers, using climate and reservoir indexex as external covariates.. 3rd STAHY International Workshopon statical methods for hydrology and water resources managment. October1-2, 2012 Tunis, Tunisia.

Meddi, M., and Ben Abbes, A.S. (2014). Analyse statistique et prévision des débits de crues dans le bassin versant de l'Oued Mekerra (Ouest de l'Algérie). Revue « Nature & Technologie ». C- Sciences de l'Environnement, 10, 21-31.

Michel, P. (1973). Les bassins des fleuves Sénégal et Gambie : Etude géomorphologique. Mémoires ORSTOM n° 63-3tomes, 752 p.

Nicholson, S.E., Some, B., Kone, B. (2000). An analysis of recent rainfall conditions in West Africa, including the rainy seasons of the 1997 El Nino and the 1998 La Nina years. Journal of Climate, 13, 2628–2640.

OMVS, Projet FEM/Bassin du fleuve senegal, (2008). Plan d'Action Stratégique de Gestion des Problèmes Environnementaux Prioritaires du Bassin du Fleuve Sénégal, Version finale, 133 p.

Onibon, H., Ouarda, T.B.M.J., Barbe, M., St-Hilaire, A., Bobee, B., Bruneau, P. (2004). Analyse fréquentielle régionale des précipitations journalières maximales annuelles au Québec, Canada / Regional frequency analysis of annual maximum daily precipitation in Quebec, Canada, Hydrological Sciences Journal, 49:4, 717-735.

Ouarda, T.B.M.J., Girard, C., Cavadias, G.S., Bobée, B. (2001). Regional flood frequency analysis with canonical correlation analysis. J. Hydrol. 254(1–4), 157–173.

Riad, S., Jacky, Mania, Bouchaou, L. (2006). Variabilité hydroclimatique dans les bassins-versants du Haut Atlas de Marrakech (Maroc). Science et changements planétaires / Sécheresse, 17 (3), 443-6.

Roche, P.A. (2003). L'eau, enjeu vital pour l'Afrique, Afrique contemporaine, n°205, printemps 2003 (http://www.cairn.info/revue-afrique-contemporaine-2003-1-page-39.htm)

Rochette, C. (1974). Monographie hydrologique du fleuve Sénégal. Coll. Mém. ORSTOM, 1442 p.

Roy, L., Leconte, R., Brissette, F.B., Marche, C. (2001). The impact of climate change on seasonal floods of a southern Quebec River Basin. Hydrol. Process. 15, 3167–3179.

Ruf, L. (2004). Caractérisation du régime hydrologique des fleuves guyanais : Etude fréquentielle et outil de calcul des débits. Rapport de Stage Ingénieur Maître, IUP Département ENvironnement Technologies et Sociétés (DENTES), 30 p.

Sow, A.A. (2007). L'hydrologie du Sud-est du Sénégal et de ses Confins guinéo-maliens : les bassins de la Gambie et de la Falémé, Thèse doctorat d'Etat Es lettres et sciences humaines, UCAD, FLSH, Département de Géographie, 1232 p

Sveinsson, O.G.B., Salas, J., Duane, C.B. (2002). Regional frequency analysis of extreme precipitation in northeastern Colorado and the Fort Collins flood of 1997. J. Hydrol. Engng. 7(1), 49–63.

Vastila, K. , Kummu, M., Sangmanee, C., Chinvanno, S. (2010). Modelling climate change impacts on the flood pulse in the Lower Mekong floodplains. Journal of Water and Climate Change, 01.1, 2010.

World Meteorological Organization (1989). Statistical Distributions for Flood Frequency Analysis. WMO-Operational Hydrology Report, n" 33, 73 p.

JJEES

JJEES (2019) 10 (3): 136-144
ISSN 1995-6681

Jordan Journal of Earth and Environmental Sciences

A GIS-based Hydrogeological and Geophysical Study for the Analysis of Potential Water Infiltration in the Upper Yarmouk River Basin, North Jordan

Muheeb Awawdeh[1*], Rasheed Jaradat[1], Khaldoon al Qudah[1], Nizar Abu-Jaber[2], Mohsen Awawdeh[3]

[1] Yarmouk University, Department of Earth and Environment Sciences, Jordan
[2] German Jordanian University, Department of Civil and Environmental Engineering, Jordan
[3] King Faisal University, Department of Social Studies, Saudi Arabia

Received 15 November 2018, Accepted 20 January 2019

Abstract

Groundwater resources in semi-arid climates in countries like Jordan have experienced deterioration both in quantity and quality. This paper aims at locating potential groundwater recharge areas in the Upper Yarmouk River Basin (UYRB) using weighted overlay method in ArcGIS. The input data for this analysis included geology, soil, land use/ land cover, slope, lineament density, and drainage density.

The results classified the study area in terms of its water infiltration potential into five categories, in which zones of high and very high infiltration potential represented 36 % of the investigated area. The maximum infiltration potential dominated the north, east, and southwest parts of the study. This is most probably due to the major influence of soil types, land cover and lineaments in the southwest, and the increased role of drainage density and topography in the north and eastern parts. The water infiltration potential was successfully validated using data from rainfall simulations and Vertical Electrical Soundings, suggesting that the moisture content of the upper 10m of the soil column is within the range 33-48%. The adopted model can be seen as a guide for water resources security and protection.

Keywords: Groundwater, Infiltration, Geographic Information System, Jordan.

1. Introduction

Water is one of the most essential commodities for mankind (Arkoprovo et al., 2012). Dominated by arid and semi-arid climates, Jordan suffers from a scarcity in natural water resources amid the increasing population growth. Economic developments and population increase have caused greater demand on water resources that resulted in a wide disparity between water supply and demand. In semi-arid regions, the partitioning of precipitation into surface runoff, infiltration and potential recharge are highly variable in space and time (Diiwu, 2004). It has been reported that about 93.9 % of the total rainfall in Jordan is lost and about 3.9 % only infiltrates to recharge the groundwater (Hadadin et al., 2010). Although the largest available source of fresh water in Jordan is obtained from groundwater, unsustainable practices of overdrawing put the water situation at risk in terms of quality and quantity (Odeh et al., 2019). Development and urbanization increase storm water runoff rates and volumes while decreasing infiltration. Moreover, climatic changes may provide even greater challenges in the future (Mohammad et el., 2018). Thus, water resources in Jordan need better management and protection strategies.

Infiltration occurs in areas where the permeability of the terrain, along with other factors, allows the rapid penetration of surface waters (Schneider et al., 2001). Part of this water percolates through the unsaturated zone of the soil and, and on reaching the water table, it recharges the aquifer. Groundwater recharge through infiltration is a very complex process which involves, but not limited to, rainfall, topography, soils, vegetation, climate, and land use (Al Kuisi and El-Naqa, 2013; Kahsay et al., 2018).

It has now become crucial to target recharge zones for artificial recharge in addition to identifying natural recharge zones in order to safeguard the water future. Artificial recharge is one of the effective techniques used for the management of groundwater resources (Raviraji et al., 2017). Ababneh (2013) found that the infiltration rate is increasing along an east -west transect in reference to soil characteristics across the Upper Yarmouk River Basin (UYRB). Al Qudah et al. (2015) have determined that the recharge rate in the UYRB ranges between 20 % and 37% of the amount of precipitation in contrast to other rates reported in previous studies (Bajjali, 2008; El -Naser, 1991; Water Authority of Jordan, 1989). Even the drier eastern areas of the basin show a notable evidence of the recharge in some areas (Abu-Jaber and Kharabsheh, 2008). This research is based on new findings (Ababneh, 2013; Al Qudah et al., 2015) and aimed at identifying the areas with the highest potential for surface water infiltration in the UYRB based on several key hydrogeological parameters.

* Corresponding author e-mail: awawdeh@yu.edu.jo

2. The Study Area

The study area is about 75 km2 (Fig. 1), with elevations ranging from 1,200 m in the highlands of Ajloun in the south down to 500 m west of the city of Ramtha in the north. Physiographically, the study area consists of the northern extension of the Ajloun highlands to the south and southwest, which grade into the Houran Plains to the north and northeast. Mediterranean climates dominate the southwest, receiving up to 600 mm/a of rain in the Ajloun highlands and around 470 mm/a in Irbid farther to the north. To the east, the climate becomes semi-arid to arid, and rainfall diminishes to about 215 mm/a in Ramtha and 150 mm/a in Mafraq (JMD, 2013). The rainfall is seasonal, falling mostly during the winter season over the months from October to April each year, with considerable annual rainfall variability. The main recharge area for the regional aquifer (B2/A7 Aquifer) is in the Ajloun highlands (Salameh, 2004). The northern end of the study area marks the start of Wadi Shallaleh, where groundwater discharges into Yarmouk River.

Geologically (Figure 2), the study area is dominated by the Upper Cretaceous Ajloun and Balqa Groups (Natural Resources Authority, 1993 and 1997). They consist of marine limestone, silicified limestone, marl and phosphorite formations. The Ajloun highlands are composed of the Upper Cretaceous limestones and dolostones that are largely karstified (Al Qudah et al., 2015). The Turonian Wadi Es Sir Formation (A7), with the overlying Campanian silicified limestone known as the Amman Formation (B2), makes up the major aquifer in the area known as the B2/A7. The Wadi Es Sir formation (Turonian) is a massive limestone formation that is highly karstified and the Amman formation (Santonian-Campanian) is a silicified limestone that has limited exposure in the northern extent of the Ajloun highlands. The southern part of the Houran Plains in Jordan are largely covered by soil which is underlain by the Muwaqqar Chalk Marl (MCM) Formation (B3). This formation (Maastrichtian) acts as an aquiclude because of the low permeability imparted by the marly clay layers creating a confined aquifer situation for the B2/A7 aquifer in that area. The Um Rijam Formation (B4) overlays the MCM Formation and consists of alternating chert and limestone beds. It acts as an aquifer in the Ramtha area, although its limited extent precludes it from being considered a regional water resource. The piezometric maps for the aquifer show a flow from the southwest towards the northeast, discharging at the springs of Wadi Shallaleh into the Yarmouk River. Although, the B2/A7 is generally viewed to obtain most of its recharge in the Ajloun Highlands, there is a strong isotopic evidence of recharge in the Nuymeh area (20 -25 km NE) as well (Bajjali, 2006). In addition, recharge has been identified farther to the east towards Mafraq (Abu-Jaber and Kharabsheh, 2008). This aquifer is the most important indigenous source of water in the Irbid Governorate (Bajjali, 2008).

Towards the east and northeast, flat plains, known as the Houran Plains, are spread with a thick red soil from the area which turns to a more yellow soil in the eastern reaches of the basin. The soils are Mediterranean red to brown soils, that consist of expandable clays (i.e. Montmorillonite). They tend to be thin in the higher area to the west and achieve thicknesses of several meters in the lower areas to the east (Al Qudah, 2015).

The study area is traditionally agricultural where olive groves, vineyards, and orchards are common in the Ajloun highlands, and crops such as wheat and barley are planted in the Houran Plains. These plains are gradually being converted for residential and commercial uses. Dense oak tree forests cover Ajloun highlands. However, about one fourth of the study area is urbanized, including mainly the cities of Irbid, Huson, Aidoon, Nuymeh, and Sareeh.

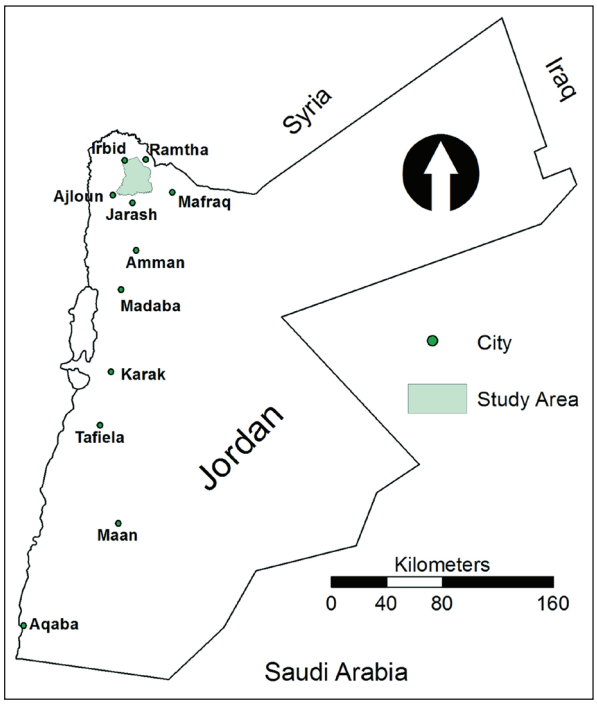

Figure 1. Location of the Upper Yarmouk River Basin, north Jordan.

3. Methods

Modeling areas with potential water infiltration is based on the concept of aquifer system contamination vulnerability. In other words, the most sensitive areas to the risk of contamination are the same areas of maximum infiltration, thus having the most favorable conditions for recharge of aquifer systems (Brito et al., 2006). Accordingly, the evaluation of areas with the highest infiltration must consider the hydrogeological characteristics of the terrain such as topography, land cover, and lineaments (Brito et al., 2006). Awawdeh and Jaradat (2010) evaluated the aquifers vulnerability to contamination in the Yarmouk River Basin. Many other studies assessed groundwater vulnerability to contamination in northern Jordan (Margane et al., 1999; Awawdeh and Nawafleh, 2008; Nawafleh et al., 2011, Awawdeh et al., 2015).

For this study, the proposed infiltration model is based on the selection and integration of information in a GIS system (ArcGIS 10.3). It combines several key hydrogeological parameters which describe the infiltration potential of present ground conditions.

Six hydrogeologyical parameters were taken into account to characterize the terrain infiltration potential

including geology, soil, land cover, slope, lineaments, and drainage system. After data collection and editing, classes of each parameter were rated from 1 to 10 based on their relative effect on the infiltration capability, with rating 1 being the least infiltration potential and rating 10 being the highest. Different weights 1-5 (Table 1) were assigned to each parameter representing their relative importance in the conceptual infiltration model. Rates and weights were based on previous studiesand opinions of local experts.

It is well-established that GIS techniques can be successfully applied for the investigations of groundwater. Therefore, raster GIS layers of the hydrogeological parameters were algebraically combined in terms of weighted overlay methods to derive the potential infiltration model (Raviraji et al., 2017).

The model yields a numerical index that defines the variations in infiltration potential. The high infiltration potential index values define areas with maximum infiltration potential, while the low index values define little infiltration potential (impermeable areas). The final map has classified the study area into having very low, low, moderate, high, and very high infiltration capacities.

Table 1. Assigned weights for various hydrogeological parameters.

Parameters	Weights (1-5)
Soil	4
Land Use Land Cover	4
Geology	3
Slope	3
Drainage Density	3
Lineament Density	2

The next step was validating the groundwater potential model by using rainfall simulations (Al Qudah et al. 2015) and the near-surface geophysical technique (Vertical Electrical Sounding –VES). The aim of these tests was to develop a better understanding of the infiltration potential along model validation.

In this study, the geophysical investigation included eight vertical electrical soundings (VES) carried out using ARES GF-Instruments Resistivity meter adopting the Schlumberger electrode configuration. The VES points were located at different locations across a N-S profile (Figure 8). The prime goal was to investigate the electrical stratification and infiltration potential down to a depth of 10-15m along the investigated profile. Collected field data are given in Table 6. The Res1DINV inversion software (Loke, 2010) was used for data inversion of the observed apparent resistivity values, where the inversion process was carried out assuming no specific initial inversion model, in that the software was allowed to use the same number of layers and thicknesses to allow for a valid comparison between the investigated points. The root mean square was used as a measure of fit.

To check the validity of the modeled infiltration potential, the value of soil moisture-content was estimated from electrical resistivity values and laboratory-based experiments using linear or non-linear regression analyses (Ozcep et al. 2009; Bahatt et al., 2014; Kazmi et al., 2016).

4. Results and Discussion

4.1 The Physical Conditions of the Basin

Figure 2 shows the detailed geology of the study area. The study area is dominated by Wadi Es Sir Formation in the southern parts (29 %), and by Amman Silicified Limestone in the middle (18 %). Soil dominates (41%) the northern part of the basin. The rating values for each formation (Table 2) were assigned based on the general characteristics of each formation.

The soil map (Figure 3) was modified after the National Soil Map and Land Use project (Ministry of Agriculture, 1994). The available data were processed and evaluated to extract appropriate information on soil texture. It is believed that more details are required to yield a more accurate soil-texture map; therefore, data from recent studies (Ababneh, 2013; Al Qudah et al., 2015) were also considered to reflect more accurate soil-texture properties. Accordingly, most of the area is dominated by silt loam and sandy soils. Table 3 lists the rating values of each soil type.

The land use/ land cover (LULC) map was digitized from Google Earth. There are six main classes of LULC in the area: agriculture, bareland, forest, orchard (mainly olive), rangeland, and urban (Figure 4). Table 4 shows the area coverage for each LULC class and its rating value. Most of the area is occupied by either rangeland (30 %), agriculture (24 %), urban (18 %), or orchard (17 %).

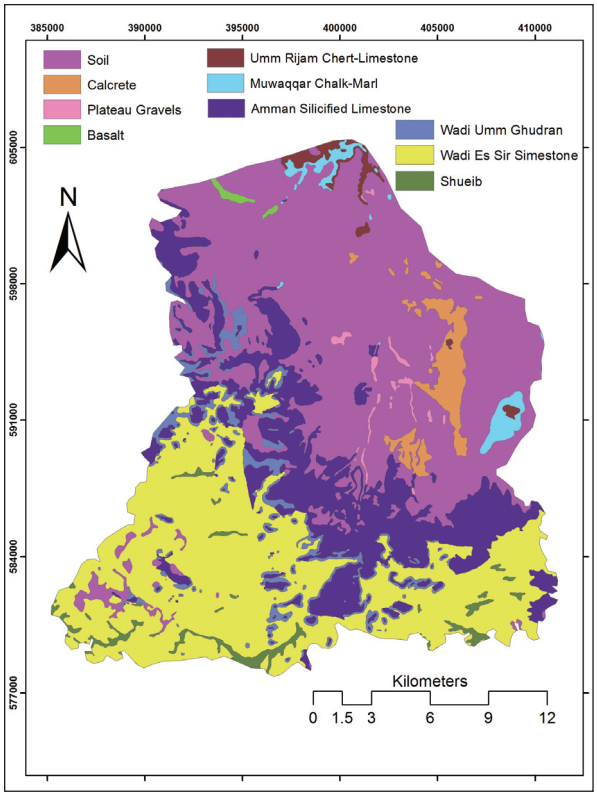

Figure 2. Geology of the upper part of the Upper Yarmouk River Basin (modified after the Natural Resources Authority, 1993 and 1997).

Table 2. Rating values of the geology map.

Formation	Rating value	Area Coverage (%)
Soil	6	41.19
Calcrete	1	2.68
Plateau Gravels	8	0.58
Basalt	7	0.23
Umm Rijam Chert-Limestone	5	0.92
Muwaqqar Chalk-Marl	3	1.28
Amman Silicified Limestone	6	18.37
Wadi Umm Ghudran	4	3.97
Wadi Es Sir Limestone	6	29.29
Shueib	3	1.50

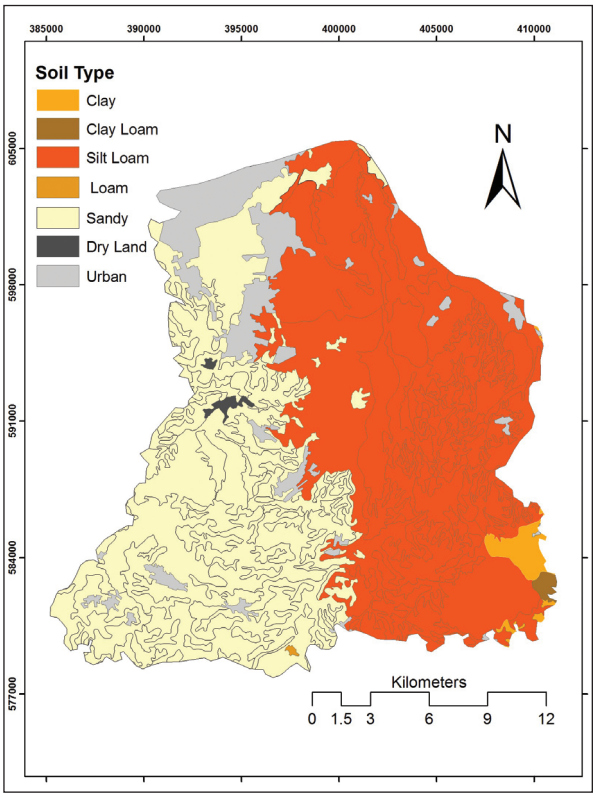

Figure 3. Soil types of the upper part of the Upper Yarmouk River Basin (modified after the Ministry of Agriculture, 1994).

Table 3. Ratings of the soil types in the upper part of the Yarmouk River Basin.

Soil Type	Rating value
Clay	3
Clay loam	2
Silt Loam	5
Loam	5
Sandy	7
Bareland	2
Urban	2

The topographic maps (1:50,000) of the Natural Resources Authority (1993 and 1997) were digitized and interpolated in GIS to derive the digital elevation model for the study area. Generally, the elevations are decreasing towards the north. A slope map (Figure 5) was derived and assigned rating values as shown in Table 5. The slope ranged from flat areas mainly in the east to 60° in the highlands. The lineaments density was calculated, classified, and rated as showed in Figure 6. The surface lineaments mapped here are those linear features observed on satellite images from Google Earth and are believed to concentrate recharge and flow. The density of lineaments is highest in the south western part of the study area, where slope is greater.

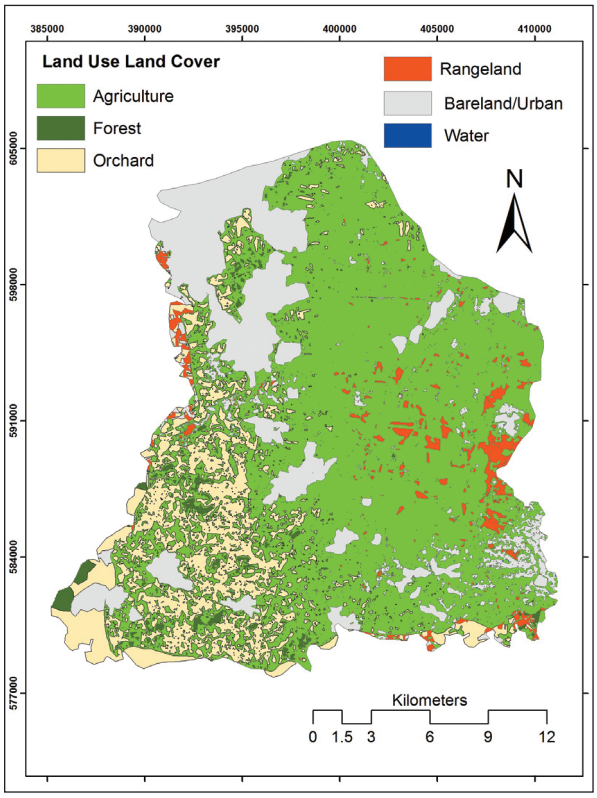

Figure 4. Land use/ land covers in the upper part of the Upper Yarmouk River Basin.

Table 4. Ratings of the land use/ land cover in the upper part of the Yarmouk River Basin.

Class	Rating Value	Area Coverage (%)
Agriculture	6	24.12
Bareland	3	1.81
Forest	9	7.63
Orchard	7	17.43
Rangeland	5	30.57
Urban	3	18.14

Table 5. Rating of slopes in the upper part of the Yarmouk River Basin.

Topography (C) %	Rating
0-2	1
3-4	2
5-6	3
7-9	4
10-12	5
13-15	6
16-18	7
19-21	8
22-25	9
>25	10

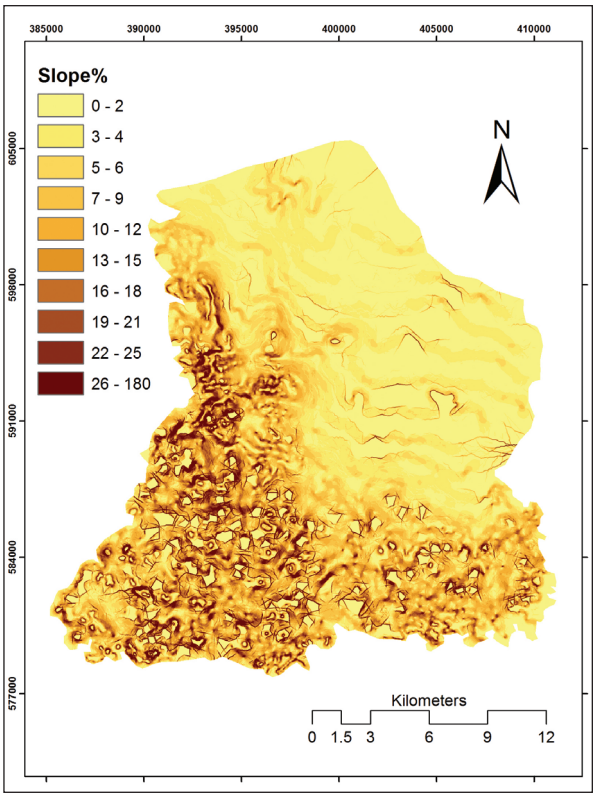

Figure 5. Topography of the upper part of the Upper Yarmouk River Basin.

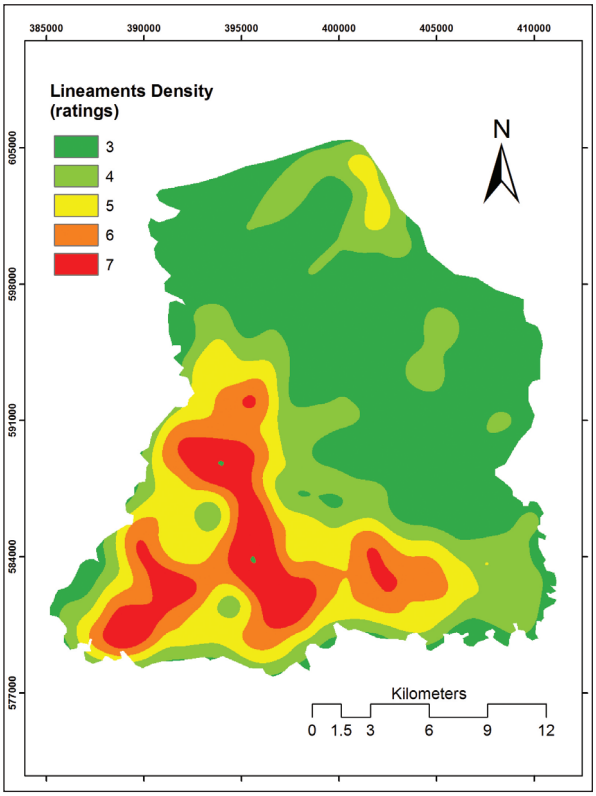

Figure 6. Ratings' map of the lineaments density in the upper part of the Yarmouk River Basin.

Images from Google Earth were also the source data to map the drainage network. The drainage density map was calculated, classified and rated appropriately (Figure 7). Drainage density was highest in the east; close to Wadi Nuymeh in the east and to Wadi Shalaleh in the north.

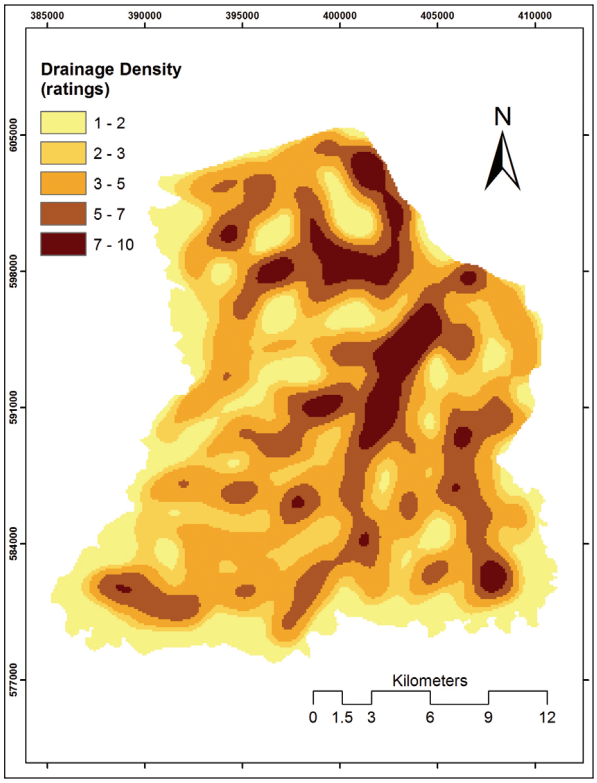

Figure 7. Drainage density rating of the upper part of the Yarmouk River Basin.

4.2 Mapping of the Potential Infiltration Areas

After successful integration of all the thematic maps, an output raster map was obtained indicating the zones with potential infiltration. The infiltration potential index was reclassified into five categories (Figure 8): very low (9.30 %), low (24 %), moderate (30.60 %), high (26.37 %) and very high (9.70 %).

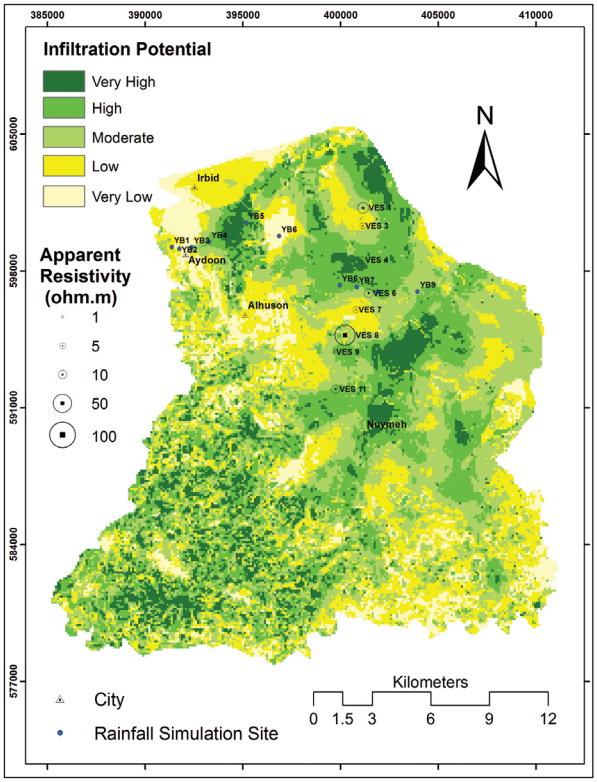

Figure 8. Potential infiltration of the upper part of the Upper Yarmouk River Basin.

Most of the areas in the high infiltration potential category are found along a southwest northeast axis and in the eastern parts of the study area. This can be attributed to the role of soil types, land cover, and lineaments in the southwest, and to the role of drainage density and topography in the north and eastern parts. About 36 % of the study area is categorized into having a high to very high infiltration potential.

4.3 Model Validation

Data from experimental rainfall field simulations (Al Qudah et al., 2015), in addition to geophysical field investigations (Vertical Electrical Soundings) were processed and used to validate the results of the infiltration potential index map (Figure 8).

Rainfall field simulations proved that water in the area penetrates the soil quickly with relatively little runoff (Al Qudah et al., 2015). The loss of moisture through the summer months occurs more likely through the drainage to deeper zones (recharge) than from evaporation. This is verified by the lack of soil carbonate accumulation in most of the soils in the area (Al Qudah et al., 2015).

The results of the inversion process are illustrated in Figure 9, indicating a variable electrical stratification. Several low electric resistivity values were encountered, almost in all of the investigated VES locations, suggesting wet conditions from potential groundwater local infiltration processes. This conclusion was valid for all of the investigated points except resulting in elevated resistivity values. A weighted average resistivity value representing the first 10m of each VES point was calculated (Table 7), using the following equation:

$$Average\ Res._{10m} = \frac{10}{\sum_{i=1}^{n}\left(\frac{h}{\rho_i}\right)} \quad \text{.....eq.(1)}$$

where h is the thickness of each resistivity layer, and ρi is the resistivity of that layer.

Figure 8 illustrates the comparison between the posted average inverted resistivity values for the upper 10m and the potential infiltration map, suggesting a good fit (70 %) between the infiltration potential classes and the computed average resistivity values. Al Qudah et al. (2015) described the soil of the study area as a silty-silty loam soil type with the soil-moisture content variying between 18-27 % for the upper 1m of the soil column. However, it is expected that the moisture content increases with depth due to increased water retention as deeper sections of soil and weathered bedrock material were approached. Nusier and Alawneh (2002) presented a water moisture-content variation with depth and seasonality variations of selected uncovered soil locations down to a depth of 10m, indicating that water content ranges between 20 % and 40%. Additionally, they showed that the depth of the zone of seasonal moisture-content variation is at about 3 m, below, and the moisture content tends to increase with depth (Figure 10).

Table 6. Field results of vertical electrical sounding (VES).

	AB/2	MN/2	Apparent Resistivity (ohm.m)							
	(m)	(m)	VES 1	VES 3	VES 4	VES 6	VES 7	VES 8	VES 9	VES 11
1	1	0.2	6.24	13.57	23.09	11.35	14.74	8.69	13.68	8.39
2	1.3	0.2	5.65	13.07	21.63	10.31	14.29	10.9	6.68	7.17
3	1.7	0.2	6.5	13.93	23.63	8.69	11.75	13.84	7.51	7.46
4	2.2	0.2	7.84	14.05	19.89	8.43	10.44	17.87	3.3	7.23
5	2.8	0.2	7.31	11.42	19.04	9.01	7.99	22.55	3.46	7.31
6	3.7	0.2	9.92	9.05	11.81	8.72	6.4	30.4	3.21	6.5
7	4.7	0.2	10.92	8.21	10.52	10	5.59	39.2	2.88	7.12
8	3.7	1	17.2	9.62	12.24	14.04	6.63	30.87	4.3	6.54
9	4.7	1	20.53	8.5	10.79	16.04	5.61	40.7	3.77	7.12
10	6.1	1	25.08	7.1	9.13	18.15	5.23	49.95	3.87	8.02
11	8	1	29.76	6.47	8.13	19.4	5.42	63.06	3.97	9.48
12	10.3	1	34.63	6.37	8.2	21.6	6.02	73.24	4.35	11.9
13	13.4	1	39.19	6.11	8.5	24.25	7.16	94.6	5	12.69

It would be a valid assumption to check the validity of the modeled infiltration potential, if a general estimate for the value of soil moisture-content within the soil column is given based on estimated resistivity values. Several studies investigated the potential to estimate the moisture of soil-water content from electrical resistivity values from field VES and laboratory-based experiments using linear or non-linear regression analyses (Ozcep et al. 2009; Bahatt et al., 2014; Kazmi et al., 2016). Some of these equations were developed assuming general types of soil, while other equations were developed for specific types such as sandy or silt-sand soils. Table 8 presents the estimated moisture contents using the Average Res. 10m values. Comparing the estimated results with those presented by Al Qudah (2015) and Nusier and Alawneh (2002), it can be said that the models of silty-sand (Kazmi et al., 2016) and all soil types (Ozcep et al., 2009) correlate well with the soils of the study area, suggesting a moisture content within the range of 33-48%. However, soil samples from a location within a close distance to the rock outcrops (i.e. VES-8) showed very low moisture-content values (15%).

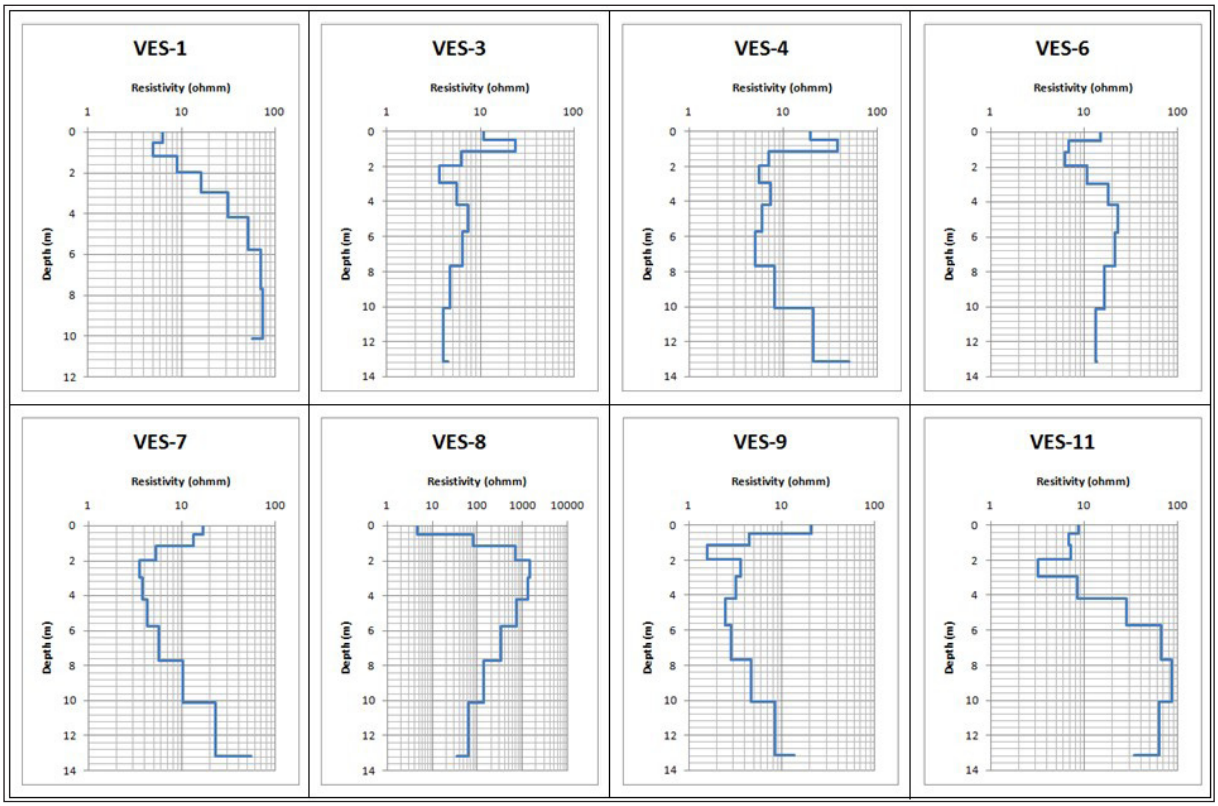

Figure 9. 1D inversion results of the collected Vertical Electrical Resistivity.

Table 7. Average resistivity values (Average Res.$_{10m}$) estimated for the upper 10m.

No.	ID	Average Res.$_{10m}$ (Ohm.m)
1	VES-1	20.86
2	VES-3	5.9
3	VES-4	6.99
4	VES-6	14.04
5	VES-7	5.65
6	VES-8	70.18
7	VES-9	3.17
8	VES-11	12.24

Table 8. Estimated moisture content using Average Res.$_{10m}$ based on several regression models. ([1]Bahhat et al. (2014), [2]Kazmi et al. (2016), [3]Ozcep et al. (2009)).

No.	ID	Estimated Moisture Content (%)			
		Sand[1]	All Soil[2]	Sity-sand soil[2]	All soil types[3]
1	VES-1	26.06	42.02	39.00	34.52
2	VES-3	28.51	58.43	44.87	44.51
3	VES-4	28.32	55.90	44.08	43.70
4	VES-6	27.15	46.60	40.84	38.76
5	VES-7	28.55	59.10	45.07	44.70
6	VES-8	19.39	30.62	33.37	14.92
7	VES-9	28.98	68.72	47.75	46.63
8	VES-11	27.44	48.30	41.48	39.97
Minimum:		19.4	30.6	33.4	14.9
Maximum:		29.0	68.7	47.8	46.6
Average:		26.8	51.2	42.1	38.5

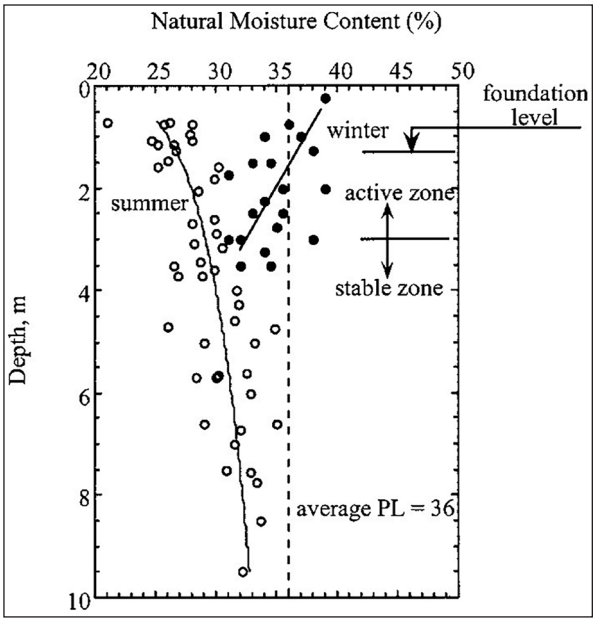

Figure 10. Seasonal variation of natural moisture content with depth of several locations representing uncovered Irbid soil samples (Nusier and Alwaneh, 2002).

5. Conclusions

The approach adopted by the current study has enabled the mapping of areas with potential water infiltration in a very important basin in northern Jordan. The combination of several essential hydrological parameters into a final map summarizes the most favorable conditions for recharging aquifer systems, and provides important strategic information as well for the location of priority protection areas because of the vulnerability of the aquifer to potential contamination. The water infiltration potential was successfully validated using data from rainfall simulations and geophysical surveying, suggesting that the moisture content of the upper 10m of the soil column is within the range of 33-48 %.

With increasing urbanization, there would be fewer areas available to storm water for infiltration. This model can be seen as a guide for water resources' security and protection strategies against the vulnerability of the aquifers and for land-use planning. Priority protection areas (high potential infiltration areas) must be considered seriously by the decision-making authorities. The authors suggest installing various groundwater recharge structures like boulder dams, check dams, percolation tanks, recharge pits etc., in appropriate locations to ensure high amounts of groundwater recharge.

Acknowledgments

We would like to thank the Jordanian Scientific Recearch Fund for their generous support of this project (3/2008).

References

Ababneh, E. (2013). Spatial variations in soil properties and infiltration rate in top soil a long a semi-arid transect, North Jordan. MSc thesis Yarmouk University, Irbid.

Abu-Jaber, N., and Kharabsheh, A. (2008). Ground water origin and movement in the upper Yarmouk Basin, Northern Jordan. Environmental geology, 54(7): 1355-1365.

Al Kuisi, M., and El-Naqa A. (2013). GIS based spatial groundwater recharge estimation in the Jafr basin, Jordan-application of wetspass models for arid regions. Rev Mex Cienc Geol, 30(1): 96–109.

Al Qudah, K., Abu-Jaber, N., Jaradat, R., Awawdeh, M. (2015). Artificial rainfall tests, soil moisture profiles and geoelectrical investigations for the estimation of recharge rates in a semi-arid area (Jordanian Yarmouk River Basin). Environmental Earth Sciences, 73: 6677–6689.

Arkoprovo, B., Adarsa, J, Prakash, S. (2012). Delineation of groundwater potential zones using satellite remote sensing and geographic information system techniques: a case study from Ganjam district, Orissa, India. Res. J. Recent Sci., 1(9): 59–66.

Awawdeh, M., Obeidat, M., Zaiter, G. (2015). Groundwater Vulnerability Assessment in the Vicinity of Ramtha Wastewater Treatment Plant, North Jordan. Applied Water Science, 5: 321–334.

Awawdeh, M., and Jaradat, R. (2010). Evaluation of Aquifers Vulnerability to Contamination in the Yarmouk River Basin, Jordan, Based on DRASTIC Method. Arabian Journal of Geosciences, 3(3): 273-282.

Awawdeh, M., and Nawafleh, A. (2008). A GIS -based EPIK Model for Assessing Aquifer Vulnerability in Irbid Governorate, North Jordan. Jordan Journal of Civil Engineering, 2(3): 267-278.

Bajjali, W. (2008). Evaluation of groundwater in a three-aquifer system in Ramtha area, Jordan: recharge mechanisms, hydraulic relationship and geochemical evolution. Hydrogeol. Journal, 16: 193–1205

Bhatt, S., and Jain, P. (2014). Correlation between electrical resistivity and water content of sand – a statistical approach. American International Journal of Research in Science, Technology, Engineering and Mathematics, 6(2): 115-121.

Brito, M., Costa, C., Almeida, J., Vendas, D., Verdial, P. (2006). Characterization of maximum infiltration using GIS tools. Engineering Geology, 85:14–18.

Diiwu, J. (2004). Groundwater-surface water interaction as a component of the ecohydrology of semi-arid regions. J. Environment systems, 30(2): 91-104.

El-Naser, H. (1991). Groundwater of the deep aquifer systems in NW Jordan: hydrogeological and hydrogeochemical quasi 3-D modeling. PhD Thesis, University of Wurzburg.

Hadadin, N., Qaqish, M., Akawwi, E., Bdour, A. (2010). Water shortage in Jordan— Sustainable solutions. Desalination, 250: 197–202.

JMD (Jordan Meteorological Department). Website. http://www.jmd.gov.jo. (2013). Accessed 2 Feb 2013.

Kahsay, G., Gebreyohannes, T., Gebremedhin, M., Gebrekirstos, A., Birhane, E., Gebrewahid, H., Welegebriel, L. (2018). Spatial groundwater recharge estimation in Raya basin, Northern Ethiopia: an approach using GIS based water balance model. Sustainable Water Resources Management.

Kazmi, D., Qasim, S., Siddiqui, F., Azhar, S. (2016). Exploring the Relationship between Moisture Content and Electrical Resistivity for Sandy and Silty Soils. International Journal of Engineering Science Invention, 5(6): 33-35.

Loke, M. (2010). RES1D version 1.00.08, 1-D resistivity, IP and SIP inversion and forward modeling, Geotomo software, https://www.geoelectrical.com.

Margane, A., Hobler, M., Subah, A. (1999). Mapping of groundwater vulnerability and hazards to groundwater in the Irbid Area, N Jordan. Z Angew Geol, 45(4): 175–187.

Ministry of Agriculture. (1994). The soils of Jordan. National Soil Map and Land Use project. Hunting Technical Services Ltd, and Soil Survey and Land Research Center, Amman, Jordan.

Mohammad, A., Jung, H., Odeh, T., Bhuiyan, C., Hussein, H. (2018). Understanding the impact of droughts in the Yarmouk Basin, Jordan: monitoring droughts through meteorological and hydrological drought indices. Arabian Journal of Geosciences, 11(5): 103.

Natural Resources Authority. (1997). Geological Map of Irbid 3155 II, sheet No.15. Geology Directorate, Amman.

Natural Resources Authority. (1993). Geological Map of Jerash 3154 I, sheet No.27. Geology Directorate, Amman.

Nawafleh, A., Awawdeh, M., Salameh, E. (2011). Assessment of Groundwater Vulnerability to Contamination in Irbid Governorate, North Jordan. DIRASAT, 38(2).

Nusier, O., and Alawneh, S. 2002. Damage of Reinforced Concrete Structure due to Severe Soil Expansion, Journal of Performance of Constructed Facilities, 16(1): 33-41.

Odeh, T., Mohammad, A., Hussein, H., Ismail, M., Almomani, T. (2019). Over-pumping of groundwater in Irbid governorate, northern Jordan: a conceptual model to analyze the effects of urbanization and agricultural activities on groundwater levels and salinity. Environmental Earth Sciences, 78(1): 40.

Ozcep, F., Tezel, O., Asci, M. (2009). Correlation between electrical resistivity and soil-water content: Istanbul and Golcuk. Int. J. Phys. Sci., 4(6): 362–365.

Raviraj, A., Kuruppath, N., Kannan, B. (2017). Identification of Potential Groundwater Recharge Zones Using Remote Sensing and Geographical Information System in Amaravathy Basin. Journal of Remote Sensing and GIS, 6:4.

Salameh, E. (2004). Using environmental isotopes in the study of the recharge-discharge discharge mechanisms of the Yarmouk catchment area in Jordan. Hydrogeol. J. 12: 451–463

Schneider, M., Forrest, I., Wallis, G., Maclean, B., Beukeboom, T., Armstrong, B., Leach, R.; Simpson, H., Graul, P., Armstrong, C., Salter, J., Grant, B., Schmidt, M., Hern, D., Teahen, G., Bateman, D., Reid, S. (2001). Perth County Groundwater Study – Final Report– Upper Thames River Conservation Authority, Ausable–Bayfield Conservation Authority, Maitland Valley Conservation Authority.

Water Authority of Jordan (WAJ) (1989) North Jordan water resources investigation project. Yarmouk basin water resources study final technical report, Amman

JJEES

Jordan Journal of Earth and Environmental Sciences

JJEES (2019) 10 (3): 145-151
ISSN 1995-6681

Geological and Hydrogeological Implications of Gravity Data in the Aqra Plain Iraqi Kurdistan Region

Nazar Numan[1] and Fadhil Ghaeb[2*]

[1] American University of Kurdistan (Duhok) / Department of Petroleum Engineering
[2] Tishk International University -TIU- (Erbil) / Petroleum and Mining Engineering Department

Received 24 January 2019; Accepted 30 April 2019

Abstract

A geophysical gravity survey was conducted in the Aqra plain in the Iraqi Kurdistan Region. The survey included 116 stations taken along the main highways and some unpaved roads. The objective of the survey was to study the structural situation of the subsurface and the effects of its geological structures on underground water to detect any gas seeps in some parts of the plain. Simple analyses of the present data were integrated with the observed surface geological features. Basement rocks underneath the plain seem to dip towards the north and northeast with a depth ranging from 5.5 to 6.5km. Gas seeps are shown to be related to a major fault between the two villages of Ruvia and Malabarwan. The condition of groundwater is fairly correlated with the residual gravity data and inferred faults. These faults are oriented in two directions, N-S and E-W.

Keywords: Gravity, groundwater, Aqra-Iraq, prospecting.

1. Introduction

In the Kurdistan Region of Iraq, the Aqra plain is located between Maqlub Mountain (30 km northeast of Mosul City) and Aqra Mountain (80km to the northeast of Mosul City). The Aqra plain has a huge aquifer that supports agriculture; some of the water wells dug in this plain are artesian. Many oil companies had carried out oil and gas exploration projects in this area over the last decade, but unfortunately, their data are not available for public use. The present study provides a gravimetric geophysical data addition to supplement other types of geophysical data for evaluating the subsurface structural framework of the region.

The objective of this work is to draw a preliminary picture in order to understand the subsurface geological structures. For this purpose, gravity prospecting was carried out in the area since gravity is among the cheapest geophysical, non-invasive, non-destructive remote-sensing methods. It is also a passive method of investigation, that is; no external energy needs to be put into the ground in order to acquire data. The collected data (from points at the surface) of gravitational attraction exerted by the earth are corrected and processed to give maps that can be interpreted in terms of geology. The strength of the gravitational field is directly proportional to the mass and, therefore, to the density of subsurface materials (Reynolds, 1997). Anomalies in the earth's gravitational field result from lateral variations in the density of subsurface materials and the distance to these bodies from the measuring equipment (Mariita, 2007).

116 gravity station measurements were carried out along the main streets and some unpaved roads. The surveyed area covers about 500 Km^2 within the almost flat areas of the plain (Fig. 1A).

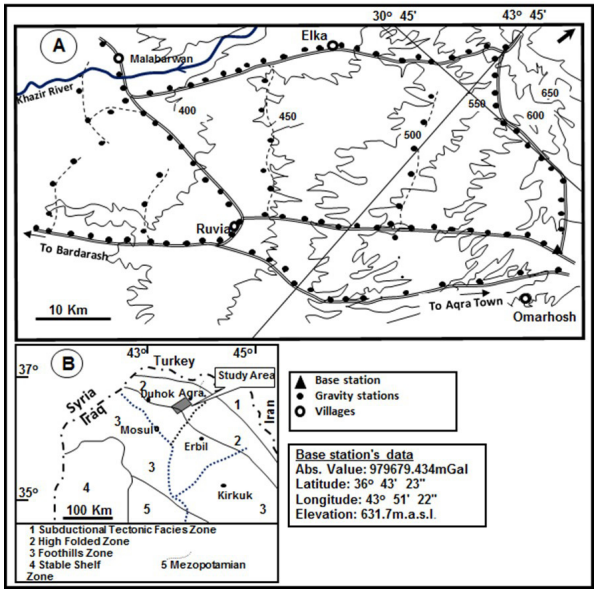

Figure 1. Location of the study area and tectonic map of Iraq

2. Geomorphology, Tectonics and Geology

The dominant geomorphology of the area is related to river deposits bounded from the extreme northern corner by ridges of the southern limb of Aqra Anticline (out of the scope of the studied part of the area) and truncated by the river Khazir in the western corner. Some of the seasonal valleys are also present. A maximum elevation of about 700 m above sea level is observed in the north and northeastern parts, while it is estimated at about 400 m in the western and southwestern parts.

According to the tripartite subdivision of the Iraqi territories (Bolton, 1958; Dunnington, 1958), the Aqra area

* Corresponding author e-mail: fadhil.ali@ishik.edu.iq

is located within the Folded Zone, which is equivalent to the same nomenclature given by Buday (1973) and Buday and Jassim (1987) in another bipartite subdivision (Fig. 1B and Fig. 2). The latter authors subdivided the Folded Zone into the Foothills Zone and High Folded Zone. In view of the application of the plate tectonic paradigm into the geology of Iraq, Numan (1997) and Numan (2001) employed new terminology for the tectonic subdivisions of Iraq (Fig. 2). The Folded Zone consists of (a) Foothill Zone of the quasi-platform foreland in which successive major anticlines are separated by 40-50 km wide areas of sub-horizontal or very broadly folded strata and (b) the High Folds Zone of the foreland basin towards the north and northeast. The Aqra Anticline forms the northeastern boundary of the Foothills Zone, and it is suggested that it was formed by the basement uplifts in stages before the Lower Miocene ages as a horst combined by a reverse fault on its southern flank (Ditmar et al., 1971). Numan (1984) subdivided the basement underneath the Folded Zone into two major blocks on the bases of the total thickness of the sedimentary cover and two distinctive trends of anticlinal structures on the two basement blocks, mostly E-W, Taurus trending anticlines over the Mosul block (including the Aqra area) and NW-SE Zagros trending anticlines over the Kirkuk block. This regional change in the trending of the anticlines occurs abruptly along the Greater Zab River (about 10km to the southeast of the area), which is the line of demarcation between the two blocks.

The study area is located between two major anticlines both trending almost E-W (Fig. 2). These are the Maqlub Anticline to the west and the Aqra Anticline to the east. The broad area (about 50 Km) between these two structures implies the presence of a gigantic broad syncline as suggested by Al-Omari and Sadek, (1973) (Fig. 2). The southern limbs of both anticlines are of high dip, and are even overturned in some locations.

Most parts of the Aqra plain are characterized by surficial expectedly thick Quaternary and alluvial deposits that overlie the older formations, which crop out in and around the area of study (Fig. 3). Table 1 lists a brief resume of the lithostratigraphic descriptions for the study area (Bellen et al., 1959).

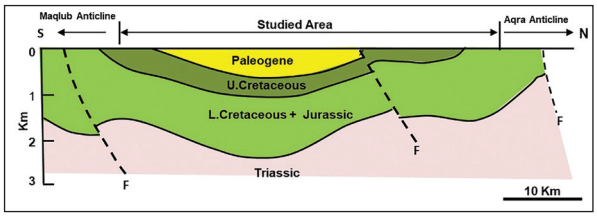

Figure 2. Cross-section between Maqlub and Aqra anticlines showing the studied area (modified after Al-Omari and Sadek, 1973)

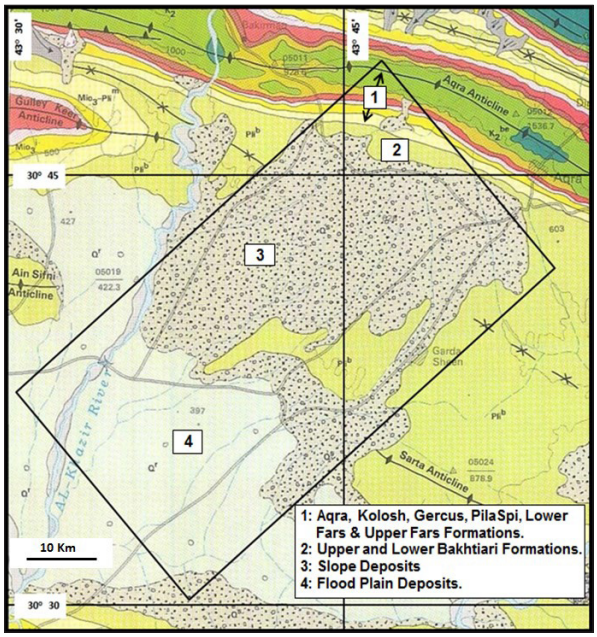

Figure 3. Geological map of Aqra area

Table 1. A brief formation descriptions in the area (Bellen et. al., 1959):

Formation Name	Age	Description
Aqra Limestone*	(Maastrichtian)	Reefal recrystallized bituminous limestone
Khurmala*	Paleocene	Bedded limestone
Kolosh*	L. Eocene	Siltstone and silty marl
Gercus*	M. Eocene	Mudstones, sandstones and siltstones
Pila Spi*	M. and U. Eocene	Crystalline dolomitic and chalky limestone.
Lower Fars	M. Eocene	Limestone, marl and gypsum
Upper Fars	U. Miocene	Loosely packed claystone and sandstone
Lower Bakhtiari	L. Pliocene	Sandstone, claystone and siltstone
Upper Bakhtiari	U. Pliocene	Conglomerate, siltstone and claystone
Slope deposits and Surface alluvium	Recent	Gravelly, sandy and silty clay

**: Not cropping out in the study area, but present underneath the plain (i.e. syncline structure).*

3. Fieldwork and Data Reduction

The fieldwork through the course of this study involved the collection of gravity data and making some geological observations in order to do more realistic interpretations. LaCoste and Romberge gravimeter (model G) and Garmin GPS were used to measure gravity, coordinates, and elevation. Rock samples were also collected to calculate densities in order to carry out corrections. The mean density of surface rocks was calculated to be 2.173 gm/cm^3 [details are given by Ghaib, (2001) and is shown in Table 2]. The local base station which was established at one of the crossroads (Fig. 1A) was tied to the Shaqlawa primary base station, some 100 Km to the southeast of Aqra town (details of looping process are again given by (Ghaib, 2001). The datum for gravity corrections was taken at the elevation of 250 m above sea level. Free air, Bouguer and Terrain

corrections were also carried out.

Types of error due to gravimeter, density, elevation, and location were checked in details and given in Table 3. The total error was found to be ± 0.3 mGal (Ghaib, 2001) according to a formula given by Bhimasankaram and Gaur (1977).

Table 2. Mean density of the cropped out rocks at the north-eastern part of the area.

Formation name	Mean density (gm/cm^3)	Formation name	Mean density (gm/cm^3)
Upper Bakhtiari	2.41	Pilaspi	2.45
Lower Bakhtiari	2.31	Gercus	1.93
Upper Fars	2.34	Kolosh + Khormala	2.47
Lower Fars	2.27	Cretaceous rocks	2.57

4. Bouguer Anomaly Map

The Bouguer anomaly map of the Aqra area (Fig. 4) shows minimum systematic indications for the synclinal trough. This reveals that the synclinal trough in between the two anticlines (Aqra and Maqlub) is never simple. Generally, the gravity values decrease towards the north and northeast (i.e. towards the Aqra Anticline). The most conspicuous anomaly extends between Malabarwan and Ruvia villages. It is a linear anomaly separating two groups of anomalies in the south and north. It has a maximum amplitude of about 7 mGal and a mean gradient of 1.2 mGal/km. On the surface and along the whole trend of this anomaly, two phenomena are noted in the field. The first is the presence of gas leakage around the Malabarwan village while the second is the artesian flow of water in most of the water wells that are drilled around the Ruvia village in contrast to the other parts of the Aqra Plain. The two phenomena clearly follow the above-mentioned linear anomaly. Moreover, the Khazir river course in the western corner also shows an abrupt bend when truncated by this anomaly (see figure 8). The best geological interpretation for this anomaly is that it delineates a fault. The general increase of gravity values towards the west probably reflects the effect of the northern limb of Maqlub Anticline.

To the north of Malabarwan anomaly, another nearly closed two-dimensional negative anomaly exists to the south of Elka village (Fig. 4). It has a minimum gravity value of –48 mGal with a NE-SW direction swinging to an almost N-S direction (approximately perpendicular to the anticline) in the northern corner of the area. The Elka anomaly is bounded from the northwest and east by two linear, high gradient anomalies likely reflecting two faults, trending NE-SW and N-S respectively.

In the eastern corner of the Aqra area, another two-dimensional, ENE trending negative anomaly is present north and northwest of the Omarhosh village. It has a minimum value of –52 mGal, which is again bounded by the linear contour lines from the northwest and the southeast.

Although the Aqra area is bounded by two surface anticlines (i.e. Aqra and the Maqlub), the pattern of anomaly shape and distribution does not show a clear indication of the presence of a gigantic syncline between the above two widely separated anticlines of the type described by Parsons (1955) and later reiterated by Al-Omari and Sadek (1973).

The thickness of the sedimentary cover overlying the basement complex, i.e. the depth to the basement is calculated from gravity data using the best approximation density contrast between the sedimentary cover and the basement, which is 0.18 gm/cm^3 (Ghaib, 2001). Using this value in the simple slab equation of Bouguer, the depth of basement in the Aqra area ranges from 5.5 to 6.5 km becoming deeper towards the north and northeast. This inferred thickness of the sedimentary cover coincides with value of the sedimentary cover thickness for the Mosul Basement Block (which includes the present study area) obtained by Numan (1984) using isopach maps and lithostratigraphic data.

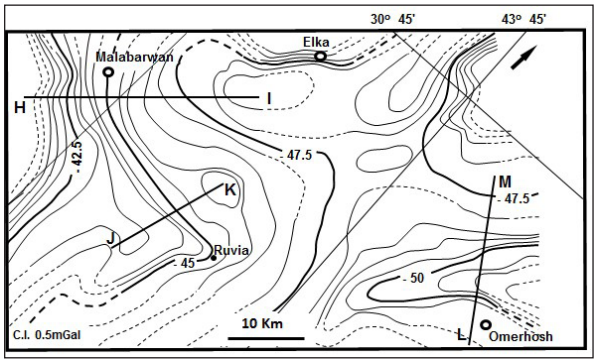

Figure 4. Bouguer anomaly map of the studied area, note the cross sections taken in this study, their descriptions are given in the text.

5. Regional and Residual Anomaly Maps

The contour smoothing method was applied to separate the regional and residual anomalies. The regional anomaly map (Fig. 5) most probably reflects the deep effects of the basement surface and its topography. This regional Bouguer anomaly map shows a regional gravity gradient towards the NNE and NE (about 0.8 mGal/km decreasing to about 0.6 mGal/km in the central part indicating a north and northeastward dip of the basement-sedimentary cover interface).

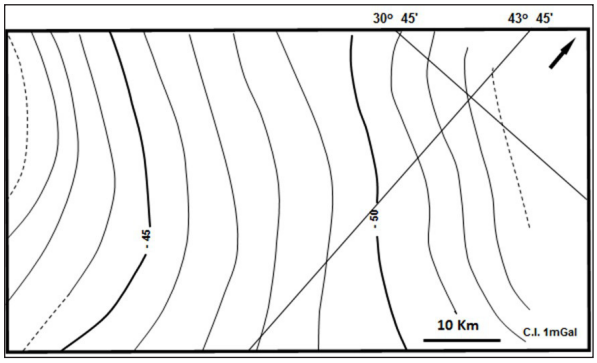

Figure 5. Regional anomaly map of the studied area

The residual anomaly map (Fig. 6) shows many positive

and negative anomalies. Two negative closed anomalies occupy together the central part in approximately E-W direction (Omarhosh and Malabarwan). This central area is consistent with a low gradient on the regional map (Fig. 6). The area by definition represents a sedimentary trough between the Aqra and the Maqlub anticlines that bound it from the north and south respectively.

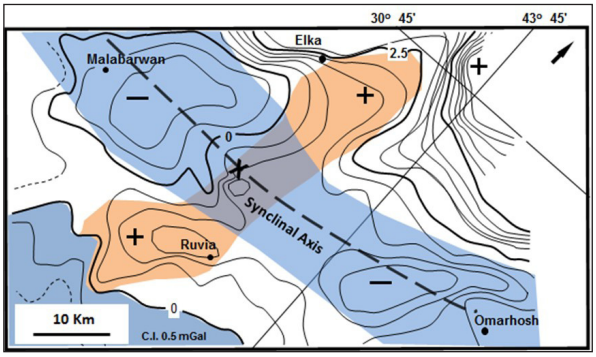

Figure 6. Residual anomaly map of the studied area

On the other hand, two positive anomalies occupy both the northern and southern parts of the studied area. The northern anomaly, trending in an E-W direction, has a high gradient. It is interpreted as being due to a rapid change of density that is related to the overturned southern limb of the Aqra anticline and/or the suggested fault (Fig. 2), while the southern Ruvia positive anomaly trending E-W again is mostly related to a local positive structure.

A special structural situation can be observed as reflected by the distribution of positive and negative anomalies within the synclinal area. In addition to the two negative anomalies mentioned above which both can reflect the general axis direction of the syncline, two positive anomalies are observed as if they cut each other perpendicularly (Fig. 6). This situation of cross-cutting negative and positive anomalies is envisaged to be the result of the syncline in this area whose axis is trending in an E-W direction and a positive anomaly trending in N-S direction. Nevertheless, the positive N-S trending anomaly can be the result of one of three possibilities as follows:

1. An N-S trending compositional variation in the basement rocks. This is in line with the N-S trends in the Precambrian rocks of the Arabian Shield and are manifested by the Najd and Hejaz orogenies in Saudi Arabia (Brown and Coleman, 1972; Shackleton, 1986) as well as the N-S trending Assyntic orogeny in the Precambrian rocks in Iran (Stocklin, 1968). According to Shakleton (1986), the N-S trending Najd and Hejaz orogenies are marked by zones of ophiolites (having high specific gravity) which resulted from collisions of Proterozoic tectonic plates. The positive anomaly in the study area may have resulted from such an N-S ophiolite zone in the basement rocks.
2. There is also an N-S trending fault system such as the Sinjar Sharaf Divide (Ditmar et al., 1971; Buday and Jassim, 1987) in Iraq. These N-S lineaments can also be discerned on satellite imagery (Numan and Bakos, 1997). The N-S trending positive anomaly in the study area could be stemming from two adjacent N-S trending faults that resulted in uplifting a basement corridor in the form of an N-S trending horst structure. Such a structure may lead to an N-S trending positive anomaly in the basement rocks (Fig. 7).
3. The third possibility requires an N-S trending rotational fault in the basement rocks. The rotational movement on the vertical fault plane would raise parts of the basement along the N-S trend of the fault plane, (Fig. 7). The presence of the positive anomalies cross-cutting the zone of negative anomalies calls for further geophysical exploration for oil and gas.

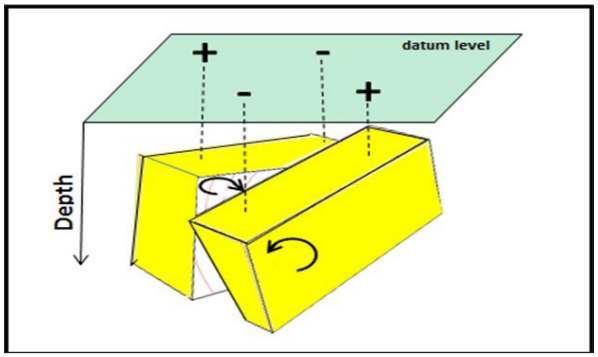

Figure 7. Example of rotated block along vertical faults

6. Quantitative Interpretation

The first step in this interpretation is the visual inspection of the Bouguer map to choose the profile across the anomaly of interest. The second is to estimate approximately the horizontal extension, depth, shape, and thickness of the target using one or more of the rapid methods of calculation such as those described by Bott and Smith (1958); Skeels (1963); and Grant and West (1965). The third step is to construct a geometric n-sided polygon, which satisfies the abovementioned estimations and is consistent with the geologic situation.

For the preliminary estimations and the final calculations as well, the density of different rock units of the causative bodies and the surroundings should be known as precisely as possible in order to calculate the density contrast which is the cause of the gravity anomaly.

The gravity anomaly, observed over a layered sedimentary basin, is close to that calculated over a basin, with the same configuration and depth, but is filled with homogenous (none layered) sediments with a density equal to that of the real layered basin. Accordingly, it is not necessary to composite the effects of the layers separately. In relatively thick successions, the density contrast approaches a minimal value with an increasing depth (Litinsky, 1989).

For each version of the geophysical models of a profile, trials of the gravity effect of an anomaly source are carried out with the density contrast kept constant. In this study, the densities which were calculated by Ghaib (2001) were utilized in modeling, using a computer program based on Talwani et al., (1959) which is one of the familiar methods that are widespread and are used all over the world. The amount of fault dip can hardly be defined in quantitative gravity interpretations. A description of the interpreted profiles across three anomalies (Fig. 8) is given bellow:

A. The Malabarwan Anomaly: Profile (H-I) (Figs. 4 and 8A) extends for about 13 km cutting the linear anomaly around the Malabarwan village. The

anomaly reaches a maximum amplitude of 8 mGal and reflects a typical fault shape. The interpretational model represents a normal fault which throws the Upper Cretaceous formations (Footwall) against the Paleogene formations (Hanging Wall). The density contrast between these two groups is 0.25 gm/cm3. There are many surface indications for the presence of this fault; some of them are discussed in the previous sections. The most conspicuous of these indications is the gas seepages noticed south of the village of Malabarwan. The fault apparently offsets Upper Cretaceous rocks and possibly continues downward to a hydrocarbon reservoir that supplies the leaking gas through the fault plane or a fault zone.

B. The Ruvia Anomaly: Profile (J-K) (Figs. 4 and 8B) extends for about 7 km and cuts the eastern end of the Malabarwan anomaly in the NNE-SSW direction. The anomaly shows an amplitude of 2 mGal. The model is designed on the same basis of profile (H-I) as a normal fault which throws the same groups of formations. The density contrast, in this case, is taken to be (0.17) gm/cm3 because the left-hand side block contains a part of the Lower Cretaceous succession of higher density. Mutib et al., 2019 interpreted this anomaly in another traverse trending N-S and concluded the anomaly to be reflected by a small anticline bounded by two faults. Depending on this study, it seems that the other fault might be present farther to the south-southwest.

C. The Omarosh Anomaly: Profile (L-M) (Figs. 4 and 8C) extends for about 10 km in the N-S direction, and cuts the Omarosh negative anomaly. It has a maximum amplitude of 3 mGal. The anomaly is expected to arise from the contrast in density between the Lower Cretaceous and the Upper Cretaceous rocks which is (– 0.17) gm/cm3. The model which satisfies the observed anomaly is in the form of a local graben of a 2.3 km width and a vertical displacement of about 0.5 km.

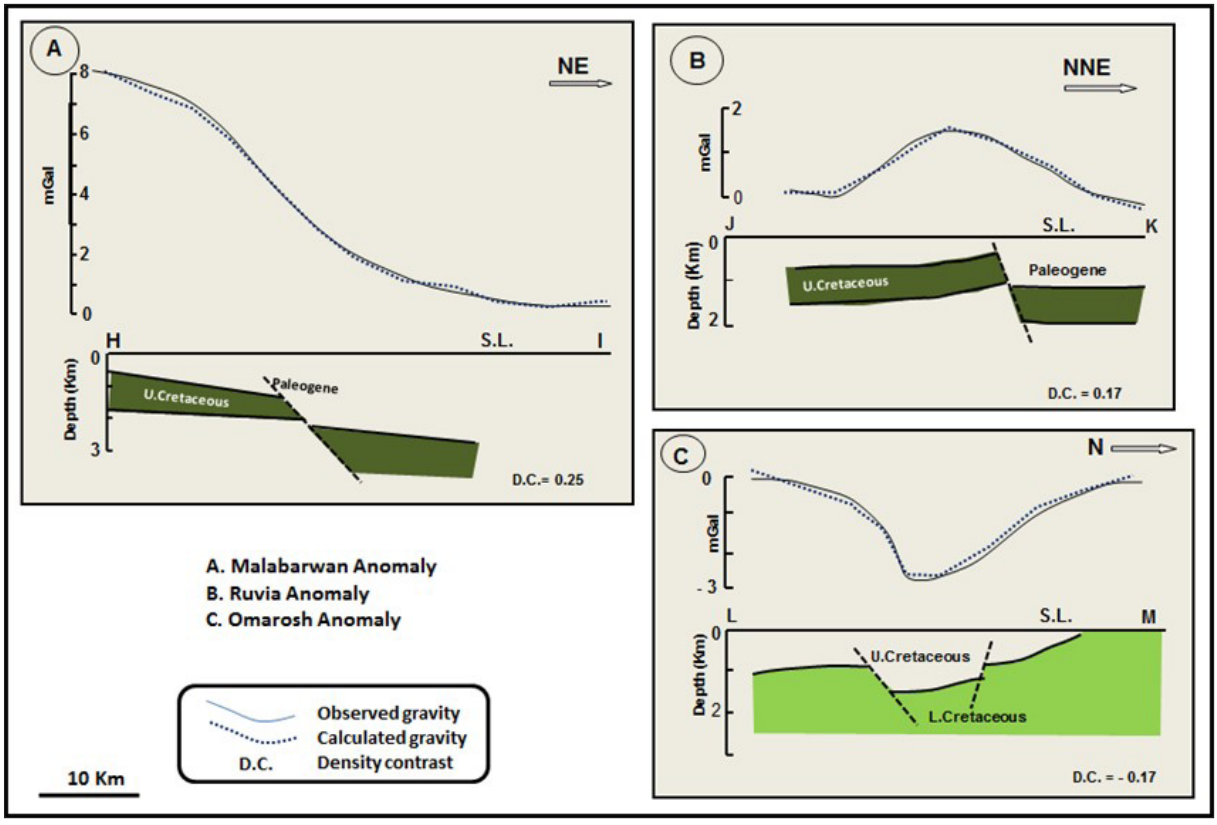

Figure 8. Quantitative Interpretation of main Bouguer anomalies used in interoperating the results of this study.

7. Geological and Hydrogeological significance

The subsurface structure of the Aqra Plain has been described in the past by Al-Omari and Sadek, 1973 as consisting of one gigantic syncline that is 50 km wide. However, the results obtained by this study show that the subsurface structure of the Aqra Plain is more complex than one major syncline with a 50 km width. There are normal faults, grabens as well as a possible horst structure in the basement rocks in the study area and they have been so pronounced to the point that they have appeared on the Bouguer anomaly map. The total thickness of the sedimentary cover was inferred from this study to be between 5.5 and 6.5 km. This finding coincides with the thickness calculated by Numan (1984) from regional isopach maps for this area.

Moreover, the lithostratigraphic data from the surrounding areas based on surface geology as well as the subsurface data from oil wells indicate the thickness of the Pre-Quaternary deposits to the basement rocks to be around 5.5 km. If this 5.5 km succession was to be thrown into a gigantic syncline that is 50 km wide, this synclinal fold geometry would require the thickness of the Quaternary deposits in the presumed syncline to be at least several kilometers more, and since in reality the total thickness of the sedimentary cover is just 5.5 to 6.5 km and most of it is

Pre-Quaternary, the gigantic syncline model does not work. In fact, the subsurface strata have to be sub-horizontal with flexure and very gentle folds including the faults that have been described. The area of study follows the pattern for the Foothill Zone of the quasi platform Foreland where major anticlines are widely separated (40-50 km) by intervening plain areas that have sub-horizontal strata to mild flexures in the strata. This is also exemplified by the Sheikh Ibrahim anticline (to the west of the study area) that is followed by the Bashiqa anticline with an intervening 40 km distance to the northeast of Sheikh Ibrahim. The Mosul area separates those two mentioned anticlines, and the outcrops of the strata under the Mosul City are demonstrably horizontal in the field.

It is geologically accepted that deeper structures are usually reflected in shallower depths. The residual gravity map of the Aqra plain (Fig. 6) shows prominent low gravity values which dominate the western part of the area (near Malabarwan village). Two conspicuous gravity anomalies as well as the inferred faults are superimposed on the net flow map of groundwater in the Aqra plain prepared by Aqrawi (1989) (Fig. 9). The flow net map is a reflection of the influence of relatively shallow geologic features (above the gravity datum level). An interesting correlation can be observed. The coincidence of the gravity low anomalies (Malabarwan anomaly in figure 8), with the main area of underground water accumulation, shows the usefulness of gravity maps in the quest of water aquifers. The artesian water wells in the Aqra plain are mainly located around the southern high residual gravity anomaly (Ruvia anomaly in figure 6). On the other hand, the locations of the faults coincide with the diversion from the usual system of groundwater flow with curvatures in the course of flow in the extreme southern part of the study area (Fig. 9).

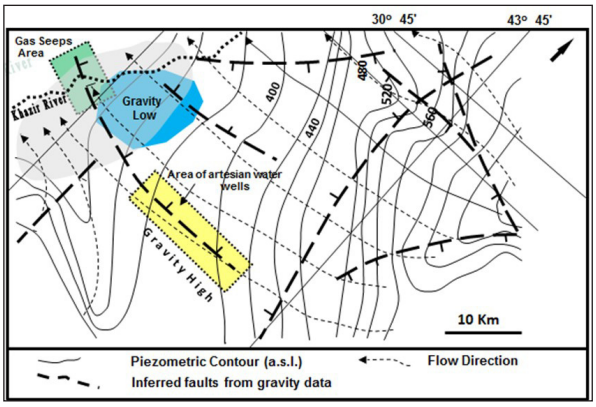

Figure 9. Net flow map of groundwater in the studied area. (modified after Aqrawi, 1989)

8. Conclusions

- The Bouguer anomaly map of the Aqra area shows a less obvious relation with the geological position of the area that is located between two widely-separated anticlines.
- The Bouguer gravity values generally decrease towards the north and northeast indicating that the basement-cover interface dips towards the north and northeast.
- A critical visual inspection of the Bouguer map reveals a gravity low zone in the central part of the Aqra area. This low gravity zone is better seen on the residual anomaly map, and extends in the E-W direction. A cutting positive anomaly is also identified. Three possibilities have been suggested for this pattern of linear positive Bouguer anomaly cross-cutting a zone of negative Bouguer anomaly.
- The thickness of the sedimentary cover overlying the basement complex ranges from 5.5 to 6.5 km. The inferred thickness of the sedimentary cover from this Bouguer gravity study coincides with the sedimentary cover thickness value for the Mosul Basement Block (which includes the present study area) obtained by Numan (1984) using isopach maps and lithostratigraphic data.
- There is a distinctive density contrast within the stratigraphic succession between the Upper Cretaceous formations (2.57gm/cm^3) and the Paleogene formations (2.28 gm/c^3).

Recommendations

Areas that are bounded by widely-separated anticlines like the Aqra area are sites of considerable thicknesses of Quaternary and recent deposits. This feature renders them as very good water aquifers, which may very well solve a lot of water shortages in the region. Further thorough geophysical investigations on the lines following this work need to be done in such areas (such as Harir and Shahrazour plains) in order to properly delineate the aquifers with their expected water yields and water quality. The possibility of stratigraphic traps is valid in such areas which have good subsurface potential for source, reservoir, and cap rocks which may well be helped by suitably situated subsurface faults. A few exploratory deep boreholes are needed in the region for this purpose.

Regional strips of gravity and magnetic studies running transverse to the trend of the Foreland Folds Belts and Thrust zone are needed in the Kurdistan region both for academic and applied purposes. A number of primary base stations need to be established in addition to the existing ones.

References

Al-Omari, F.S., and Sadek, A. (1973). Geologic studies on Gebel Maqlub area, N-Iraq. Iraqi J. Geol. Soc., VI: 66-82.

Aqrawi, Z.A. (1989). Hydrogeology of Aqra plain. Unpublished M.Sc. Thesis, Mosul University, Iraq, 155p.

Bellen, V.R.C., Dunington, H.V., Wetzel, R., Morton, D.M. (1959). Lexique stratigraphiue international. Fasc. 10a, Iraq, Paris, 333p

Bhimasankaram, V. L. S., and Gaur, V. K. (1977). Lectures on Exploration Geophysics for Geologists and Engineers. Association of Exploration Geophysicists, Geophysics, 449 pages.

Bolton, C.M. (1958). The geology of the Rania area. Site investigation co. rep., v ix (117) p. D.G. Geol. Surv. Min. Investigation. Lib., Report no. 271, Baghdad.

Bott, M.H.P., and Smith, R.A. (1958). The estimation of the limiting depth of gravitating bodies. Geoph. Pros., IV: 1-10.

Brown, G.F., and Coleman R.G. (1972). The tectonic framework of the Arabian Peninsula. Intern. Geol. Congr. XXIV Session Proc. Sect. 3, Montreal.

Buday, T. (1973). The regional geology of Iraq, part 2, structure. SOM Lib., Baghdad, Unpublished

Buday, T., and Jassim, S.Z. (1987). The regional geology of Iraq. Tectonism, Magmatism and Metamorphism. Vol.2 D.G. Of geologic survey an mineral investigation, Baghdad, Iraq. 352p.

Ditmar, V., Afanasiev, J., Briossove, B. and Shaban, S. (1971). Geological conditions and hydrocarbon prospects of the Republic of Iraq (Northern and Central parts). V. 1, Technoexpert report, INOC lib., Baghdad, Iraq.

Dunnington, H.V. (1958) Generation, Migration, Accumulation, and Dissipation of Oil in Northern Iraq. In: Weeks, L.G., Ed., Habitate of Oil, a Symposium, Association of Petroleum Geologists.

Ghaib, F.A. (2001). Geophysical survey of Aqra and Erbil plains and their geological implications, Ph.D.theis, Salahaddin University, Iraq (Unp.), 185p.

Grant, F.S., and West, G.F. (1965). Interpretation theory in applied geophysics. New York, McGraw Hill. 583p.

Litinsky, V.A. (1989). Concept of effective density: Key to gravity depth determinations for sedimentary basins. Geoph. 54(11): 1474-1482.

Mariita, N.O. (2007). The gravity method, Presented at Short Course II on Surface Exploration for Geothermal Resources, organized by UNU-GTP and KenGen, at Lake Naivasha, Kenya.

Mutib M., Al-majid M.H, Ghaib, F.A. (2019). Implementation of Gravity Investigations across Aqra Structures - Iraq. J Geol Geophys 7: 459

Numan, N.M.S. (1984). Basement controls of stratigraphic sequences and structural patterns in Iraq. Geol. Soc. Iraq J., 16: 8-28.

Numan, N.M.S. (1997). A plate tectonic scenario for the Phanerozoic succession in Iraq. Iraqi Geol. J., 30(2): 2-28.

Numan, N.M.S., and Bakos, G.Y, (1997). Lineaments: Questions on the veracity of their relationships in the western and southern deserts of Iraq. ITC Journal, 1997- 1, pp. 41-48.

Numan, N.M.S. (2001). Cretaceous and Tertiary Alpine subductional history in northern Iraq. Iraqi Jour. Earth Sci., 1 (2), pp. 59-74.

Parsons, R.M. (1955). Groundwater resources of Iraq. V.9 . Hydrologic aspects.

Reynolds, J.M. (1997). An Introduction to Applied and Environmental Geophysics.

Shackleton, R. M., (1986). Precambrian collision tectonics in African. In collision tectonics, Geol. Soc. Lond. M. P. Coward and A. C. of Ries (Editors), Pub. No. 19, pp. 329-349.

Skeels, D.C. (1963). An approximate solution of the problem of maximum depth in gravity interpretation. J. of Geoph., 2 8(5): 724-735.

Stocklin, J. (1968). Structural history and tectonics of Iran, A review. Bull. A. A. P. G., 52, 7, pp. 1229-1258.

Talwani, M., Worzel, J.L., Landisman, K. (1959). Rapid gravity computation for two-dimensional bodies with application to the Mendacino Submarine Fracture Zone. J. Geoph. Res., 64: 49-59.

JJEES

JJEES (2019) 10 (3): 152-160
ISSN 1995-6681

Jordan Journal of Earth and Environmental Sciences

Structural Evolution of Wadi Hudaydun in Wadi Shueib Area, NW Jordan

Saja Abutaha[1], Mohammad Atallah[2], Abdulkader Abed[1]

[1] The University of Jordan, Department of Geology, Jordan
[2] Yarmouk University, Department of Earth and Environmental Sciences, Jordan

Received 13 April, 2018; Accepted 14 May, 2019

Abstract

The study area of Wadi Hudaydun and its surroundings forms part of the 80 km long and NE trending Wadi Shueib Structure in northwestern Jordan. The area is predominated by the Late Cretaceous carbonates with minor bedded cherts and phosphorites of the Ajlun and Belqa Groups. A complex structural style is revealed during the measuring and mapping of the main structural elements. The major area's structures consist of two fold belts; Al Baqr - Hudaydun fold belt and Ath-Thughra fold belt intersected by a complex structural style of fault zones. These faulting systems are normal faults, striking WNW-ESE and N-E, while those trending NW-SE are of the thrusting type. Dextral and sinestral strike-slip faults are also recognized in the area. With the aid of fieldwork observations and the use of "Multiple Inverse Method Software Package", the main stress axes are obtained.

The results of the current study suppose that most of the geological structures in the investigated area follow two tectonic events. The major one is associated with the Late Cretaceous stress pattern, which is presumed to have occurred during the formation of the Shueib Structure, and produced the NNE-SSW folds of Al Baqr-Hudaydun belt. Its maximum and minimum compressive axes (σ1 and σ3) are trending towards the WNW-ESE and NNE-SSW, respectively. The minor tectonic phase can be either correlated to a local stress or may even be attached to the primary stresses of the Dead Sea Fault (DSS). Its trend, probably swinging towards the N-S direction, has produced Ath-thughra fold belt. Two distinctive compressional structures are observed in the studied area as well; they are the fault-propagation fold and the strike-slip fault.

Keywords: Fold belt, Structural analysis, Shueib Structure (SHS), fault-propagation fold, duplex structure, Syrian Arc Fold Belt (SAFB), Syrian Arc Stress Field (SAS), Dead Sea Transform Belt (DST), Dead Sea Stress Field (DSS).

1. Introduction

The investigated area, Wadi Hudaydun, which belongs to the SAFB, is located some 25 km from the northeastern tip of the Dead Sea, 20 km WNW of Amman city, within the central part of Wadi Shueib (Fig. 1). It is bounded by longitudes: 35° 42' 21.54'' and 35 44' 18.45'' E, and latitudes 31° 56' 53.62'' and 31 58' 0.18'' N. The area covers about 5 km^2. It is dissected by three main wadis, namely Wadi Hudaydun, Wadi Ath-Thughra, and Wadi Al Baqr, and is separated by three highlands; Hudaydun highland, AthThughra highland and Al-Baqr highland (Fig. 2).

The objective of this study is to investigate the structural deformations in details and deduce the stress regime affecting the area. It is different from previous studies, in that it shows new evidences of the Mastrichtian-Post Cretaceous (Oligocene-Miocene) activity, and proposed new structural relationships of the tectonic events and evolution of Wadi Shueib structure in the Wadi Hudaydun area, as a whole.

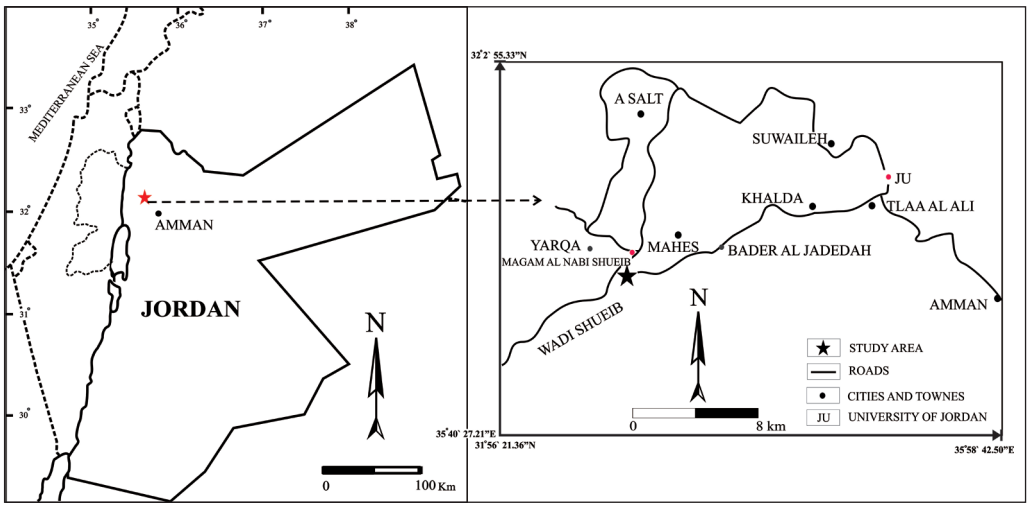

Figure 1. Location map of the study area and the roads leading to it.

* Corresponding author e-mail: sajaabutaha@yahoo.com

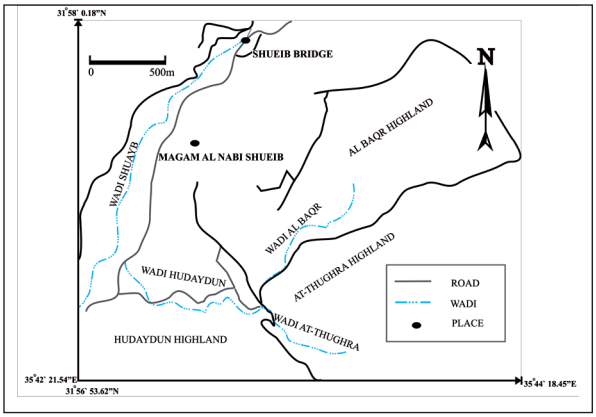

Figure 2. Detailed map of the study area showing the names of wadis and highlands used in the text.

2. Materials and Methods

Extensive field investigations, aerial photographs scales (1:10000 and 1:25000), Google topographical photos, and an accurate contoured topographic map in (1:25000) scale, are used to perform detailed structural map. The map shows the major structural elements investigated with simplified geological map (Fig.3). Multiple Inverse Method Software Package has been used to deduce the major trends of area's stresses.

2.1 Stress Analysis

To analyze the stress fields, this study uses Multiple Inverse Method Software Package which includes two major parts, namely the main and post processors. The main processor calculates stresses that are consistent with the data. The post processor, not only visualizes the stresses, but also provides various functions to analyze the data and stresses. Because the absolute values of the principal stresses are unachievable in most cases, a relative magnitude of these principal stresses can be estimated from fault population data. For this purpose, the program uses the stress ratio $\Phi = (\sigma2 - \sigma3)/(\sigma1 - \sigma3)$, where $\sigma1$, $\sigma2$ and $\sigma3$ are principal stresses and $\sigma3 \leq \sigma2 \leq \sigma1$. By definition, the value of Φ has the range [0, 1]. The two cases $\Phi = 0$ and 1 represent the stress states $\sigma1 > \sigma2 = \sigma3$ and $\sigma1 = \sigma2 > \sigma3$, respectively.

The parameters of a fault-slip datum consist of the orientation of the fault plane and the slip direction of the hanging-wall block. Since five out of ten major fault attitudes in the study area are measured with their slickenlines recorded accurately, they are used to analyze stresses field by this program. Table 1 shows the dip direction and the dip of the plane, faz and fpl, respectively. The slip direction is denoted by the orientation of slickenside striation and the sense of movement. The former is indicated by the azimuth of plunge of the striation, saz and spl. The letters in the last column represent the first letter of the "Normal," and "Dextral" fault-slip data. The angles are thought to be within the ranges of $0^\circ \leq$ faz, saz$<360^\circ$and $0^\circ \leq$ fpl, spl$<00^\circ$.

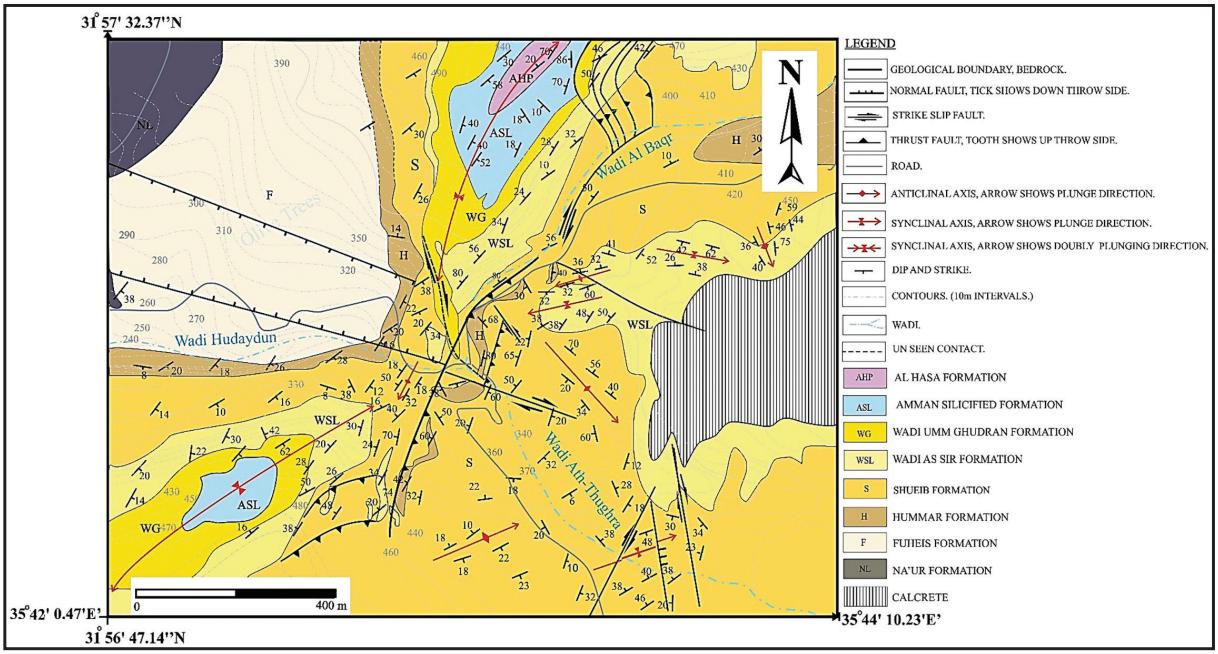

Figure 3. Geological map of study area.

Table 1. Slip data in Wadi Hudaydun area

Fault No.	Strike	Dip	Rake	Faz	Fpl	Saz	Spl	Sense
Fault1	110.0	60.0	-80.0	200.0	60.0	219.4	58.5	N
Fault2	260.0	40.0	-85.0	350.0	40.0	356.5	39.8	N
Fault10	330.0	40.0	-50.0	60.0	40.0	107.6	29.5	N
Fault3	150.0	80.0	150.0	240.0	80.0	326.0	21.6	D
Fault11	140.0	70.0	140.0	230.0	70.0	316.5	9.4	D

Two plotting methods are used in this software package including great-circles and poles or tangent lineation diagram. The first method exhibits the attitudes of faults by great-circles (Fig. 4), and the slip directions of the hanging wall blocks are indicated by arrows attached to the great-circles. In other words, the normal faults are denoted by arrows pointing away from the center of stereogram, and the strike-slip faults are exhibited by paired arrows attached to the great-circles.

The stereograms use a lower-hemisphere, equal-area projection. Each of the symbols that have heads and tails like tadpoles plotted on the stereograms represents a state of stress with the common principal orientations and the common values of stress ratio.

Optimal stress of the five faults, which are depicted by thick lines are shown in Fig. 4. The position of the head of a tadpole symbol on the stereogram indicates the σ1 and σ3 orientations (Fig.5 left and right stereogram); they are 324.5 ˚ trending and 58.5 ˚ plunge and around 130 ˚ trend and 31˚ plunge, respectively. On the whole, it can be concluded that the maximum stress direction trending is towards the N-S.

The correspondence between the length of the tail and plunge is shown by the ten gray tadpole symbols plotted between the stereograms; they indicate the plunges at 0˚, 10˚, 20˚, and 90˚. Φ values are digitized with the intervals of every 0.1 on the color bars just under the stereograms. Violet and red indicate Φ = 0 and 1, respectively. Therefore, the color of tadpoles (green to yellow) in Fig.5 is assigned to a moderate stress ratio, it is around 0.4.

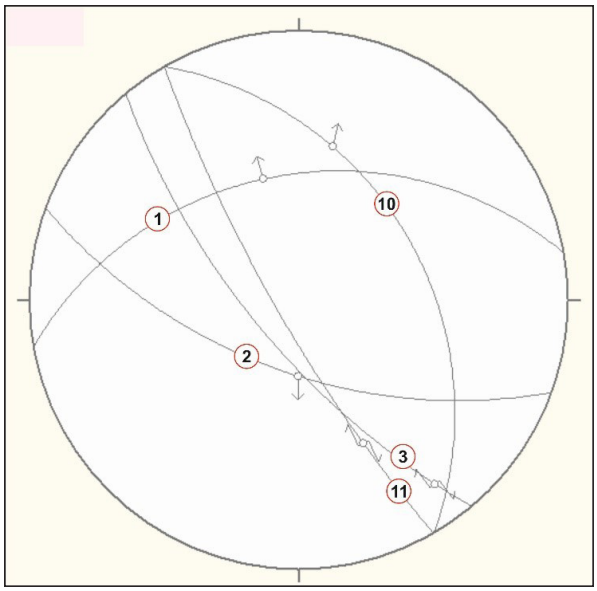

Figure 4. Lower-hemisphere, equal-angle projection. Numbers in open circles indicate the fault numbers in the map.

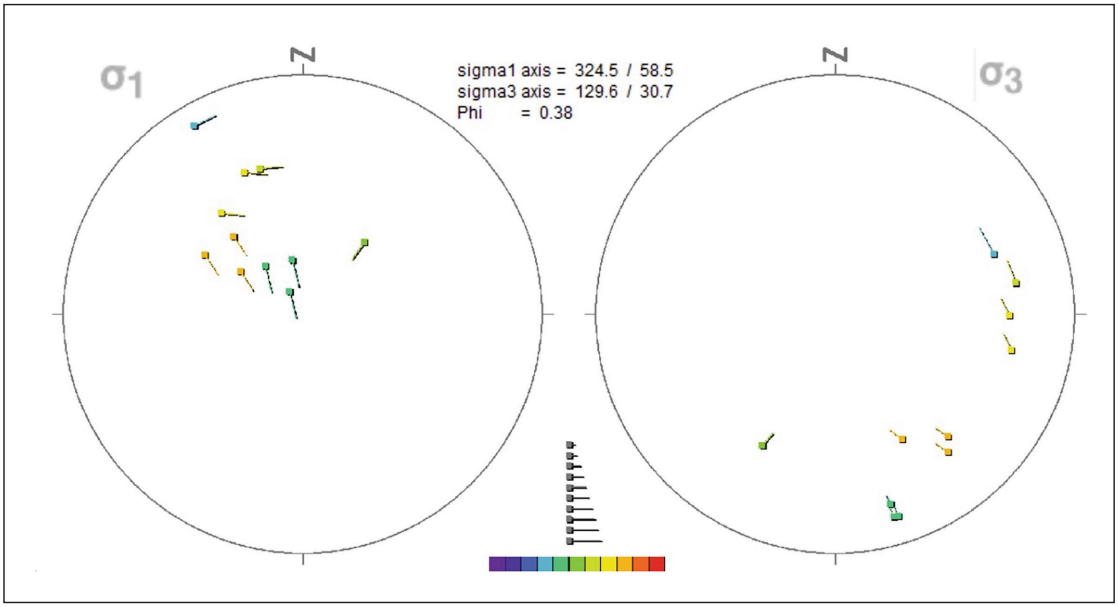

Figure 5. The position of the tadpole symbol on the stereogram indicates the major σ1 orientation and minor σ3. Phi~0.4.

3. Geological Setting

3.1 Stratigraphy

The present work deals with late Cretaceous carbonate facies. thick sequence of predominantly carbonate rocks of Cenomanian–Coniacian age, which represents the Ajlun and Belqa Groups, are exposed in the area of study. The formations that are measured and observed over there have been shaded in Table 2.

The Amman Silicified and Al-Hisa Formations are well-preserved in the cores of the major synclines at the northern and southern corners of the study area. However, the complete sequence of Ajlun Group (Na'ur, Fuheis, Hummar, Shueib and Wadi As Sir formations) is exposed at the eastern, central, and western borders of the study area. The most complicated and deformed part of the study area is its central part near the three wadis' intersection.

Table 2. Nomenclature of the Ajlun – Belqa Groups in the study area, Jordan.

Age		Group	Formation	Member
Tertiary	Eocene		Shallala	
			Umm Rijam Chert Limestone	
	Paleocene		Muwaqqar Chalk Marl (MCM)	
	Paleocene-Mastrichtian	Balqa	Al-Hisa Phosphorite (AHP)	Qatrana Phosphorite
				Bahiyya Coquina
Late Cretaceous				Sultani Phosphorite
	Campanian-Santonian		Amman Silicified Limestone	
	Coniacian		Wadi Umm Ghadran	Dhiban Chalk
				Tafila
				Mujib Chalk
	Turonian	Ajlun	Wadi As Sir Limestone	
			Shueib	
	Cenomanian		Hummar	
			Fuheis	
			Na'ur	
Early Cretaceous	Aptian-Albian		Kurnub (Hathira)Sandstone Group	

3.2 Tectonic setting

Coinciding with the contractional tectonic style, the closure of the Neo-Tethys, and the convergence of the African-Arabian Plate with the Eurasian Plate, a new NW-oriented horizontal compressive stress was generated (e.g. Ricou, 1995; Abd El Motaal and Kusky, 2003; Bumby and Giraud, 2005). This stress regime caused the flexturing of the preexisting strata forming a number of folds frequently associated with reverse and thrust faults, known as the Syrian Arc Fold Belt (SAFB) (Krenkel, 1924; Reches et al., 1981; Burek; 1981; Chaimov and Barazangi, 1990; Chaimov et al., 1992; Shahar, 1994; Reilinger and Mc Clusky, 2011). The largest structures in NW Jordan are the Amman-Hallabat Structure (AHS) and Shueib Structure (SHS); interpreted as part of the SAFB (e.g. Abed, 1989). The SAS is perhaps still active up to the present time (Awabdeh et al., 2015). The SHS was first coined by Mikbel and Zakher (1981) who gave a general description to the deformations along its length; a description which remained with little or no additions since then.

4. Results

4.1 Description of the Structures

The folds are divided into two belts; Al Baqr -Hudaydun highlands fold belt and Ath-Thughra highlands fold belt. The first fold belt includes three folds, namely Al Baqr doubly plunging syncline, Hudaydun anticline, and the doubly plunging Hudaydun syncline, which are present along Wadi Al Baqr and Wadi Hudaydun, respectively. The axis of Al Baqr syncline plunges 2˚ to N24˚E and 5˚ to the S24˚W (Fig.6a), whereas the axis of the Hudaydun syncline plunges 10˚ to the N42˚E and 20˚ to the S30˚W (Fig.6b). The Hudaydun anticline, which separates the two abovementioned doubly-plunging synclines, strikes towards S12˚W (Fig.6c).

The second belt, Ath-Thughra fold belt, extends along the eastern side of the study area between Wadi Al Baqr and Wadi Ath-Thughra. It includes seven folds, mostly asymmetrical; their plunging varies from 5˚ to 29˚ in different directions (Fig. 7). The folding is affecting the Mastrichtian phosphorite limestones (Al Hisa Formation) in Al-Baqr syncline and Hudaydun folds, while Ath-Thughra fold belt has affected the older carbonates of the Hummar and Shueib Formations.

Different types of faults are recognized in the study area (Fig. 8). Two major trends of a normal fault are measured, WNW-ESE, and NNW-SSE (e.g. fault10/Fig. 9b). The first two strikes, which are almost parallel but with an opposite downthrow, form a small graben (e.g. faults 1 and 2 /Fig. 9). Thrust faults are mainly striking towards the NNW-SSE (fault 4 and 6 in Fig. 9). Two types of strike-slip faults are also recognized in the area: dextral faults which are the dominant faults (e.g. faults 8 and 3 in Fig. 9/Fig. 9a, /Fig.9c, and fault 9), and the less abundant sinistral faults (e.g. Fig.9/d). The highly deformed fold limbs have resulted from faults passing through folded rocks that left some relicts on fault planes.

4.2 Distinctive Structural Features

Two distinctive structures are documented in the area, namely the fault-propagation fold and the strike-slip fault. These structures are used by some authors (e.g Al-Hseinat, et al., 2015) as a convenient evidence of the horsetail model theory that considered Wadi Shueib Structure a subsidiary feature splaying from the DST.

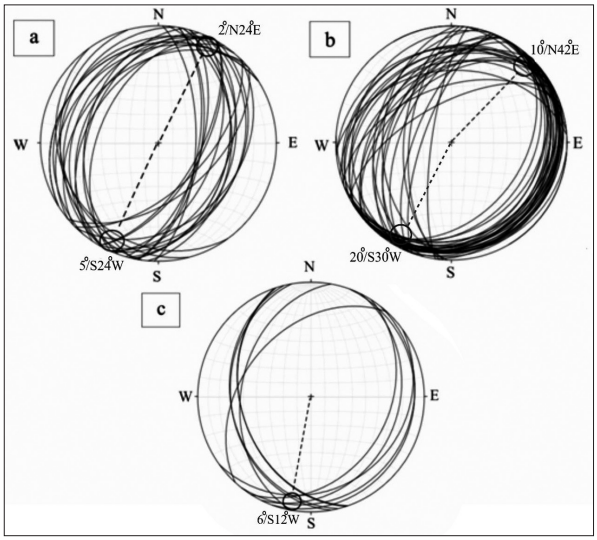

Figure 6. Stereographic projection of Al Baqr and Hudaydun fold belts.

4.2.1 Fault-propagation Fold

This type of fold is formed in association with thrust faults; as the fault tip propagates, the overlying beds are folded. By continuing propagation, the forelimb and the backlimb of the fold lengthen and form an asymmetric anticline. In the study area, this fold is located within the lower side of the eastern limb of Al-Baqr syncline (Fig. 10). The flat segment of the fault follows the soft marl beds of the Shueib Formation, while the ramp segment transects the hard limestone beds of the Wadi As Sir Formation. The fault and the overlying fold are verging to the southwest direction.

4.2.2 Strike-Slip Duplex

This structure is formed due to the bending of strike-slip faults. Depending on the type of bending (right or left) and the fault type (sinistral or dextral), either transpressive or transtensile duplexes are formed. Towards the uppermost part of the eastern limb of Al Baqr syncline, a duplex structure is formed. It consists of an array of several thrust faults that parallel a bend in a strike-slip fault (Fig.11a) passing through Wadi As Sir, Ghudran and Amman Silicified Formations (Fig.11b). Contractional thrust faults bounded by the two dextral strike-slip segments (fault5) generate a “contractional strike-slip duplex”. It is recognized as a positive relief comprised of a series of juxtaposed areas, resulting in stacked S shape fault blocks.

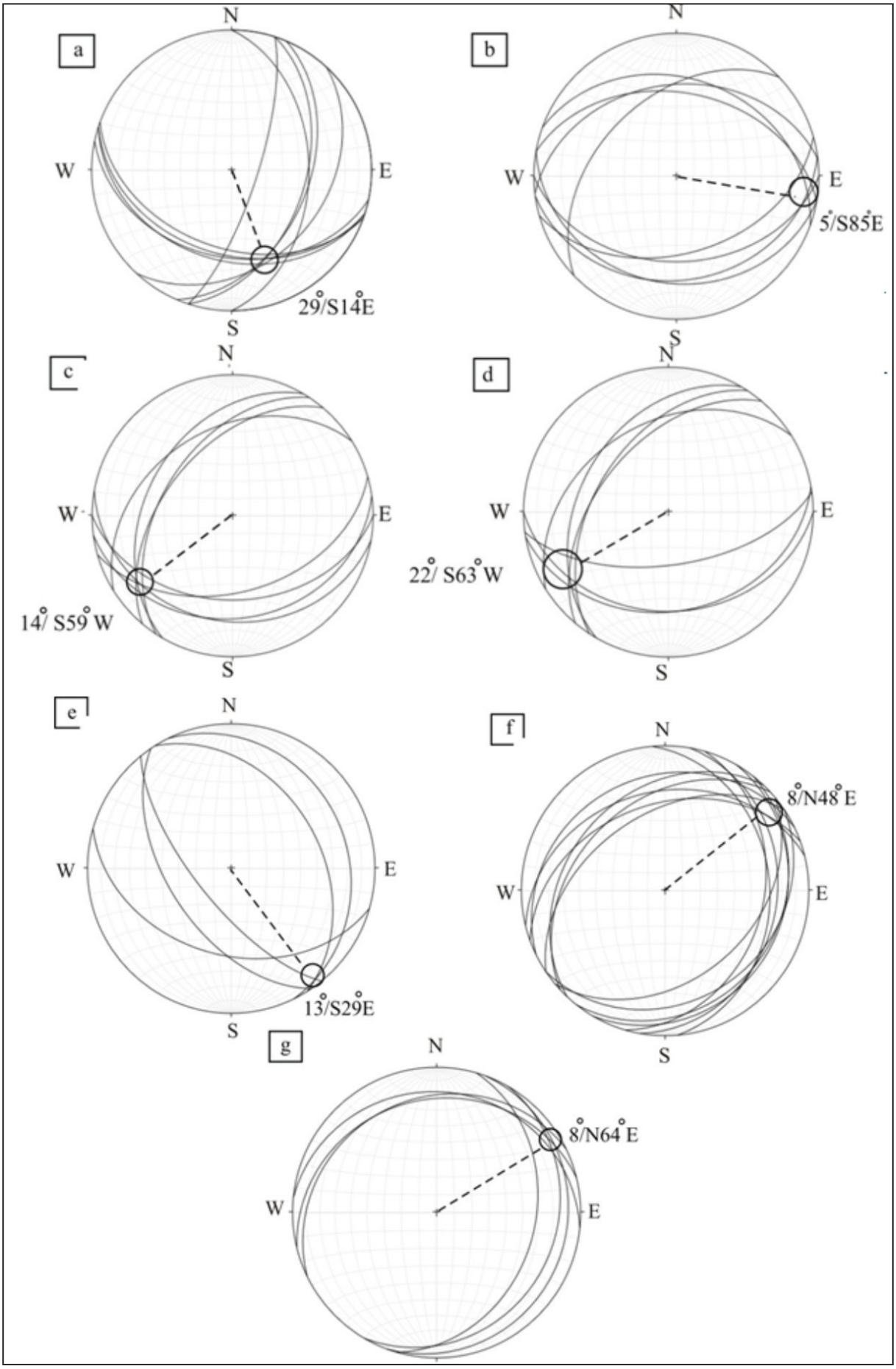

Figure 7. Stereographic projection of Ath-Thughra folds.

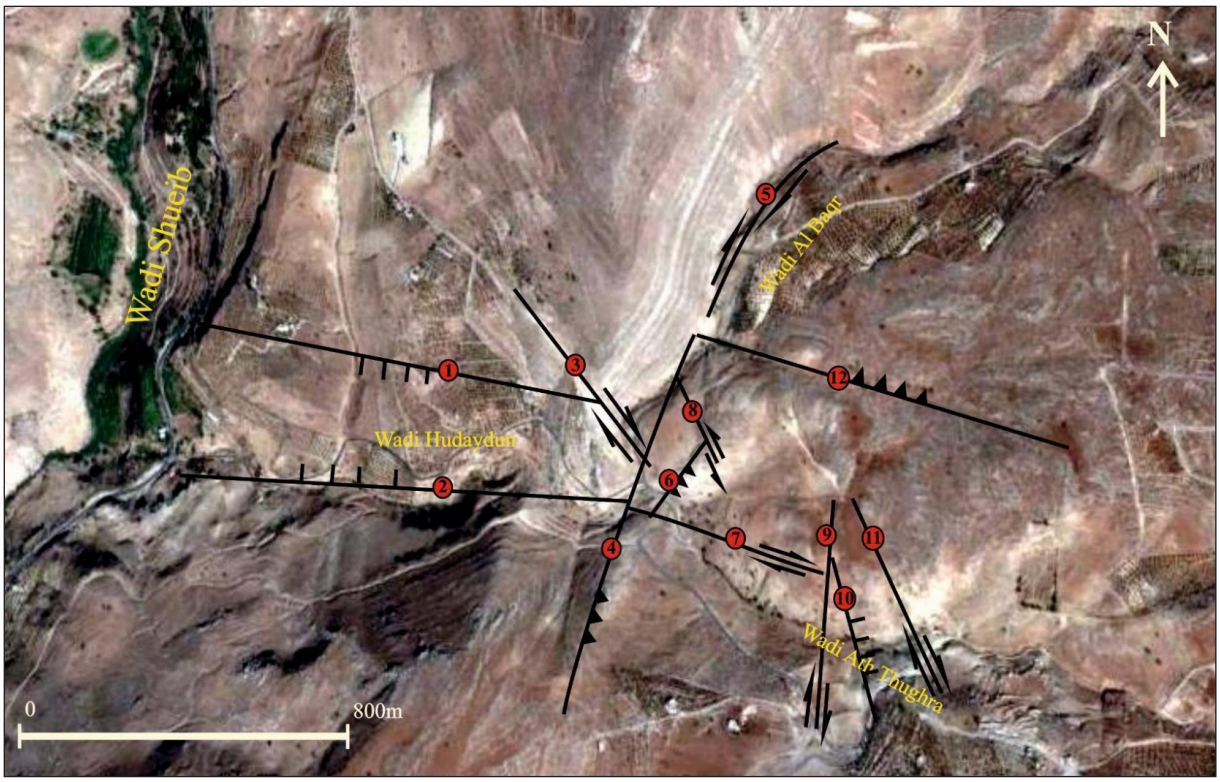

Figure 8. Google map of the major faults in the study area.

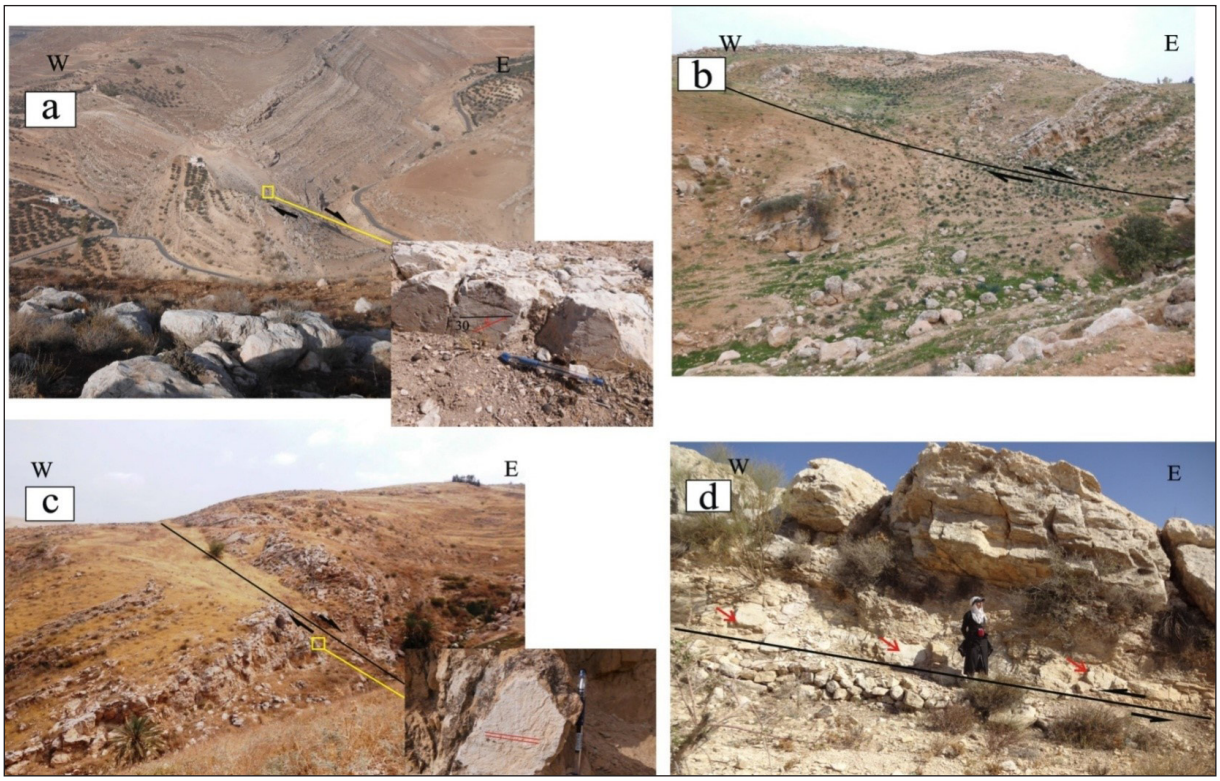

Figure 9. a) Fault 3; rake 30W, oblique dextral type; **b)** Fault 10; vertical section of normal fault / Ath-Thughra fold belt; **c)** Fault 11; dextral slip fault with horizontal slickenlines; **d)** A left lateral minor fault crossing the Al Baqr syncline, it is recognized by tracing slickenside "red arrows" in the Shueib layers.

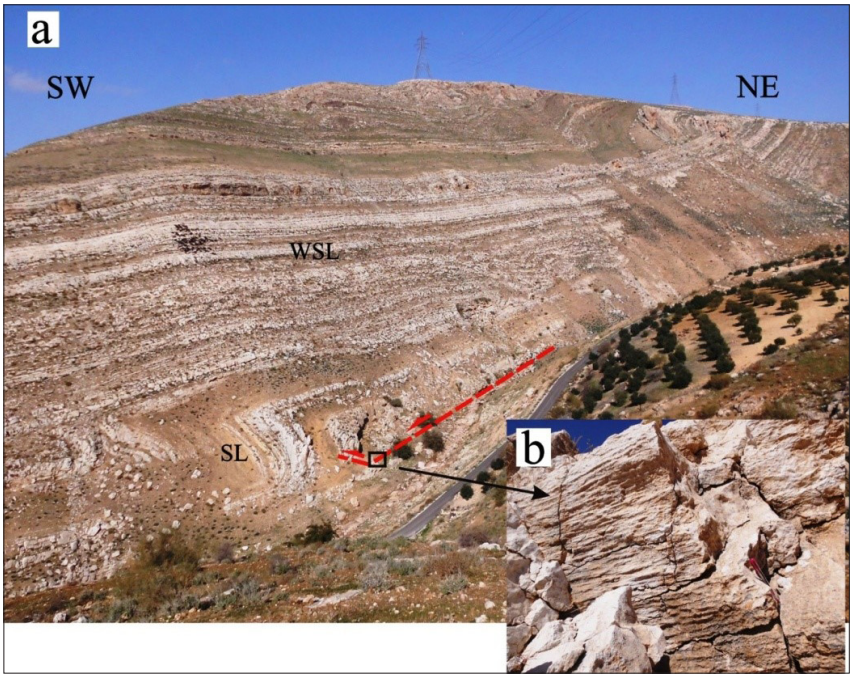

Figure 10. shows **a)** Fault-propagation fold feature in the western limb of Al Baqr syncline **b)** Horizontal slickenlines assigning sinistral strike-slip fault. (WSL=Wadi As Sir Limestone formation, SL= Shueib Limestone formation).

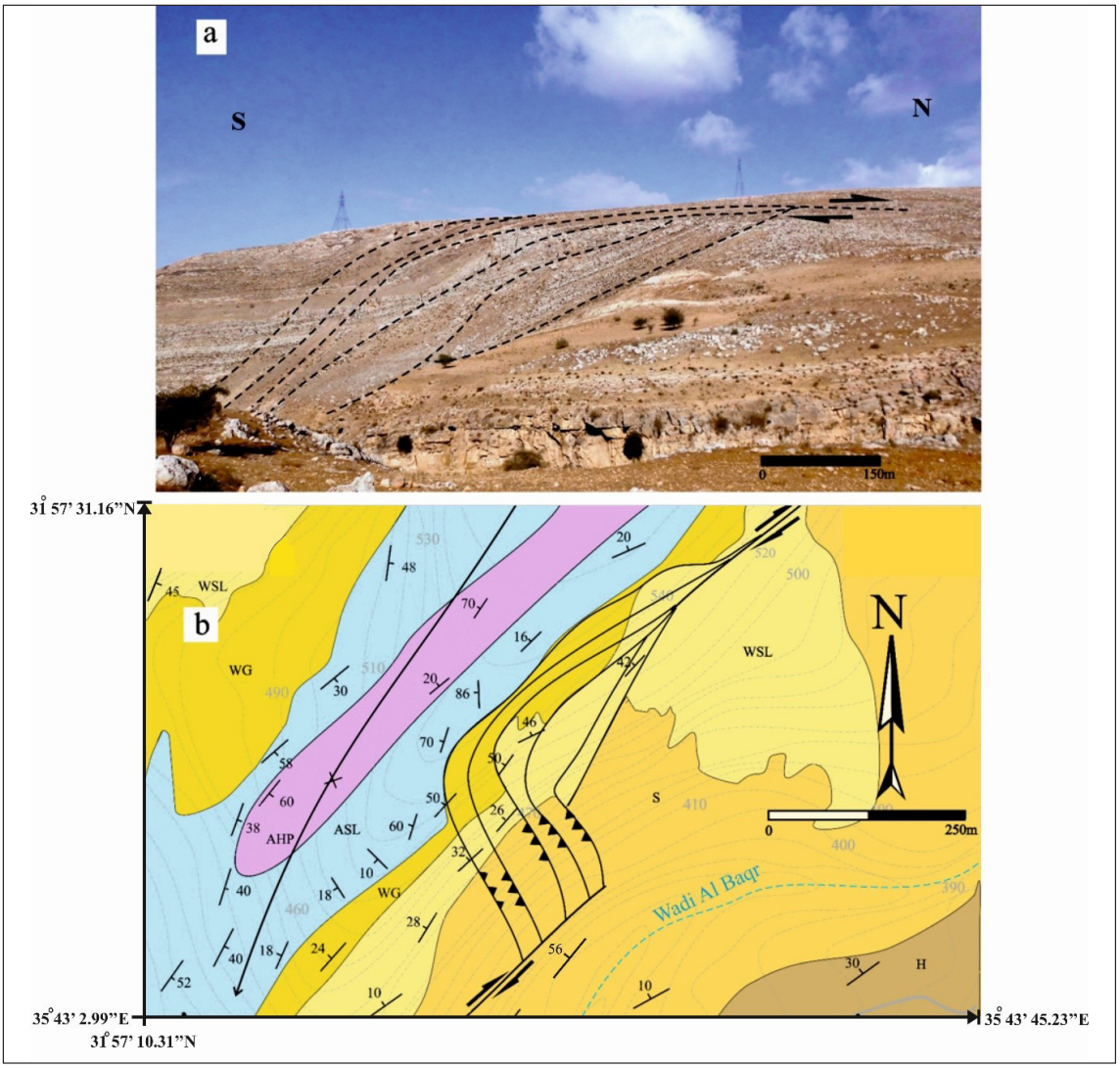

Figure 11. Strike-slip duplex a) Thrust fault system along juxtaposed horse of the strike-slip duplexes structure in the study area. The dashed line illustrates the contractional thrust fault at Wadi Al Baqr, b) the geological map shows the strike-slip duplex structure in the study area. For legend, see Fig. 3.

5. Discussion

Several authors indicated that two main stress fields have been affecting central and northern Jordan. The first field is characterized by ESE-WNW compression and NNE–SSW extension (Burden, 1959; Diabat et al., 2004; Diabat, 2009) These are: The Wadi Shueib and Amman Hallabat structures trending towards the NNE-SSW and NE-SW, respectively (Mikbel and Zacher, 1981, 1986). The latter structures are associated with the (SAS) (e.g. Abed; 1989). The second paleostress regime, which is a NNW–SSE compression and ESE–WNW extension is related to the (DSS) (Qassem, 1997; Zain Eldeen et. al., 2002; Sahawneh and Atallah, 2002; Al khatib et al., 2010, Al Tarawneh; 2011). Amman Hallabat Structure and Shueib Structure are redefined as active structures since the Neogene (Diabat, 2009; Al Awabdeh et al., 2015, and 2016), and are receiving a direct transference of tectonic stress through the Wadi Araba Fault (Awabdeh et al., 2015).

The main trends of the fold axes in the study area, based on measuring 10 axes of the folds, are: NNE-SSW and ENE-WNW of Al Baqr-Hudaydun fold belt and Ath-Thughra fold belt, respectively. The first fold belt trend N30°E of Al Baqr-Hudaydun structure is supposed to be the result of the ESE-WNW stress (Fig.12a). The youngest sediments of Al Baqr-Hudaydun structure that have been affected by a folding process are related to the Mastrichtian Period, which means that the folded deformations' stress is much younger than the folded sediments itself. In other words, the compressional folding force could have occurred beyond the Mastrichtian period (post Cretaceous). Many authors proved that the activity of the SAS has started in Turonian (Davies, 1984; Chaimov et al., 1992; De Ruiter et al., 1994; Guiraud and Bosworth, 1999; Diabat et al., 2004; Diabat, 2007, Giana et al., 2013) and it still active till now (Al Awabdeh et al., 2016). Hence, the area of study is considered as part of the Wadi Shueib structure, and the Wadi Shueib structure is considered part of the SATB (Zacher and Mikbel, 1981). Accordingly, it could be mentioned assertively that the investigated area must have been deformed by the SAS as well.

The short longitudinal extension of the Ath-Thughra folds (meso scale folds) and the major trend of its axes N70°E (Fig.12b), presuppose more than one scenario to interpret Ath-thughra structure. Firstly, the NNW-SSE maximum compressional stress is introduced as a local confined stress force that has affected the Cenomanian-Turonian sediments (Hummar and Shueib Formations), or based on the kinamatic analysis of the area's faults, it could have been affected by the DSS.

To sum up the whole former discussion, it can be said that the paleostress analysis of the study area's faults indicates one paleostress regime belonging to one major phase; the major tensor of the maximum compressive stress axis trends toward the NNW-SSE direction, and since Al Baqr-Hudaydun and Ath-Thughra folds' limbs are cut by these faults, they must have been younger than the youngest folding phase of the Al Baqr-Hudaydun belt. They were developed in the post-Cretaceous period, perhaps during the Early Paleocene-Miocene, or they could be related to the Dead Sea Stress Field and the opening of the Red Sea (Freuend et al., 1970; Diabat, 2007). Ath-Thughra belt folding seems to be corresponded with the faulting activities because of the consistency of the maximum compressional force of the Ath-Thughra folds and the maximum compressive stress axis of the area's faults that had, approximately, the same attitudes ~N30°W (Fig.12b). The only evidence for relating Ath-Thughra and fault events to the Dead Sea stress is the absence of the Quaternary deposits in the study area; under other circumstances this theory remains in doubt.

The strike-slip duplex structure occurred in competent beds (Wadi As Sir Limestone and Amman Silicified Limestone formations) that are separated by thin incompetent layers of Ghudran chalk Formation. Meanwhile, the flat segment of the fault-propagation fold structure took place in a weaker incompetent soft marl beds of the Shueib Formation, and its ramp segment transects the hard limestone beds of the Wadi As Sir Limestone formation (competent). Moreover, because they cut the eastern limb of Al-Baqr syncline, they must be younger than Al-Baqr folding phase. Therefore, the strike-slip duplex and fault-propagation folds are generated by northern trends of dextral and sinistral strike-slip faults; respectively, assigning a north trend of the maximum compressive stress that could be also associated with the formation of Ath-Thughra fold belt structure. Moreover, the strike-slip duplex compressional structure is one of the clues to explain and detect the relationship between Wadi Araba fault terminus, which represents the eastern border of the Dead Sea shore, and Shueib-Hallabat structures. They are considered as a subsidiary features splaying from the Dead Sea Transform fault (Al- Hseinat et al., 2015; Al Awabdeh et al., 2015). Accordingly these distinctive structural features could be regarded as extra proof to consider the DSS as a major stress field for the Wadi Hudaydun deformations.

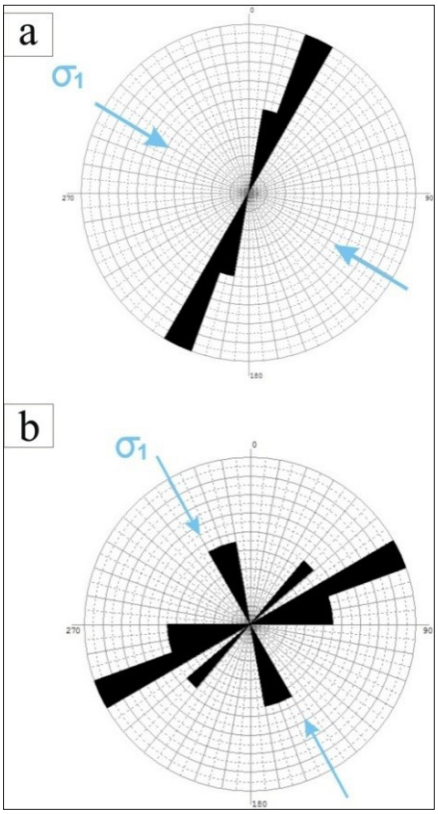

Figure 12. Rose diagrams show a) The major trends of fold axes in Al Baqr-Hudaydun fold belt. Blue arrows indicate the maximum horizontal compression axis. b) The major trends of fold axes in Ath-Thughra fold belt. Blue arrows indicate the Maximum horizontal compression axis.

6. Conclusions

The Wadi Hudaydun area is subjected to two phases of folding that are different in type, trending, and scale. The first phase of Al Baqr-Hudaydun fold belt produced asymmetrical large longitudinal extension folds (exceeds 1 Km), striking NNE-SSW, and is supposed to be the result of ESE-WNW compressional forces. It occurred through the accumulation of the horizontal stresses in the Arabian plate as a consequence of the northward movement and the rotation of the Arabian plate in the Late Cretaceous period. This stress pattern is similar to the one associated with the Shueib Structure which is a branch of the Syrian Arc Fold Belt. The second phase of the Ath-Thughra belt, trending to the ENE-WSW direction, is assumed to have occurred as a result of NNW-SSE maximum compressional stress. The maximum compressive stress of the fault slip data, striking to the NNW-SSE, and the compressional structure features (the duplex structure and the fault propagation fold) could have been produced either by local stress or by the Dead Sea transform fault stress.

Inaccuracy in detecting the reason behind Ath-Thughra's folding and the faulting time is due to the absence of the Quaternary deposits in Wadi Hudaydun area. However, because the faults are cutting through Al Baqr-Hudaydun and Ath-Thughra fold limbs, they must have been younger than the youngest folding phase of the Al Baqr-Hudaydun belt, and thus the age of the area's deformation could be between the Maastrichtian and post- Cretaceous period; perhaps during the Early Paleocene-Oligo-Miocene).

References

Abd El Motaal, E., and Kusky, T. (2003). Tectonic evolution of the intraplate S-shaped Syrian Arc Fold-Thrust belt of the Middle East region in the context of plate tectonics, The Third international conference on the geology pf Africa, 2: 139-157.

Abed, A.M. (1989). On the genesis of the phosphorite – chert association of the Amman formation in the Tel Es-Sur area, Ruseifa, Jordan, Sci. Geol., 423: 141-153.

Al-Hseinat, M., Atallah, M., Diabat, A. (2015). Structural Analysis of the Wadi Shueib Fold Belt, Jorda. M.Sc. Thesis, University of Al Yarmouk. Irbid, Jordan.

Al Awabdeh, M., Peña, J., Azañón, J., Booth-Rea, G., Abed, A., Atallah, M. (2015). Quaternary tectonic activity in NW Jordan: Insights for a new model of transpression-transtension in the southern Dead Sea Transform Fault. Phd thesis, University of Granada.

Al awabdeh, M., Peña, J., Azañón, J., Booth-Rea, G., Abed, A., Atallah, M. (2016). Stress analysis of NW Jordan: New episode of tectonicrejuvenation related to the Dead Sea transform fault. Phd thesis, University of Granada.

Al-Khatib, N., Atallah, M., Diabat, A. (2010). Paleostress analysis of the Cretaceous rocks in Northern Jordan, JJES, 3: 25-36.

Al-Tarawneh, M. (2011). Structural setting of the Jordan northern Highlands, phd thesis university of cape town, republished of south Africa, 253.

Bumby, A.J., and Giraud, R. (2005). The geodynamic setting of the Phanerozoic basins of Africa. Journal of African Earth Sciences, Elsevier Science,43: 1-12.

Burden, D.J. (1959). Hand book of the geology of Jordan: to a company and explain the three sheet of 1: 250,000 geological map east of the rift.

Burek, B.J. (1981). Tectonic effects of Sea floor spreading on the Arabian sheild. Aufsatze, Dallas, 59:382-389.

Chaimov, T., and Barazangi, M. (1990). Crustal shortening in the Palmyrids fold belt, Syria, and implications for movement along the Dead Sea fault system. Tectonics, 9: 13699-1386.

Chaimov, T. A., Barazangi, M., Al-Saad, D., Sawaf, T., Gebran, A. (1992). Mesozoic and Cenozoic deformation inferred from seismic stratigraphy in the Southwestern intracontinental Palmyride fold –thrust belt, Syria. Geological Society of America, Bulletin, 104: 704-715.

Davies, B.F. (1984). Strain analysis of wrench faults and collision tectonics of the Arabian Nubian Shield, Journal of Geology, 92: 37-54.

De Ruiter, R.S.C.; Lovelock, P.E.R. Nabulsi, N. (1994). The Euphrates graben, Eastern Syria: a new petroleum province in the Northern Middle East. In: M. Al-Husseini(ed.), Geo 94, Middle East Petroleum Geosciences. Gulf Petrolink, 1: p. 357-368.

Diabat, A., Atallah, M., Salih, M. (2004). Paleostress analysis of the Cretaceous rocks in the eastern margin of the Dead Sea transform. Journal of African Earth Sciences, 38: 449-460.

Diabat A. (2007). Paleostress Analysis of the Cretaceous-Tertiary Rocks in Central Jordan, Dirasat, Pure Sciences, 34: 2.

Diabat, A. (2009). Structural and stress analysis based on fault-slip data in the Amman area, Jordan, Journal of African Earth Sciences, 54:155-162.

Eyal, Y. (1996). Stress field fluctuations along the Dead Sea rift since the Middle Miocene. Tectonics, 15: 157-170.

Freund, R., Garfunkel, Z., Zak, I., Goldberg, M., Weissbrod, T., Derin, B. (1970). The shear along the Dead Sea Rift. Philos. Trans. R. Soc. Lond. Ser. A: Math. Phys. Sci. 267(1181), 107-130.

Gaina, G., Trond, H., Torsvik, T., van Hinsbergen, D., Sergei Medvedev, S., Cinthia Labails., (2013). The African Plate: A history of oceanic crust accretion and subduction since the Jurassic, Tectonophysics, 22.

Guiraud, R.and Bosworth, W. (1999). Phanerozoic geodynamic evolution of northeastern Africaand the north weastern Arabia plate. Tectonophysics, Elsiever science, 315: 73-108.

Krenkel, E. (1924). Der Syriasche Bogen, Zentral bulletin fur Mineralogle Geologie und Palaontology 9, p. 274-281, 10, 301-313.

Mikbel, S.and Zacher, W. (1986). Fold structure in Northern Jordan, N.Jb, Geol.Palaont, Mh., Stuttgart, 4: 248-256.

Mikbel, Sh., and Zacher, W. (1981). The Wadi Shueib Structure in Jordan. N. Jb. Geol. Palaont. Mh. H., 9: 571-576.

Qassem, J. (1997). Tectonic along Wadi Shueib Structure. M.Sc. Thesis, University of Jordan. Amman, Jordan.

Reches, Z., Hoexter, D., Hirsch, F. (1981). The Structure of a monocline in the Syrian Arc System. Middle East-surface and subsurface analysis, Journal of Petrolium Geology, 3, 4:413-425.

Reilinger, R., and Mc Clusky, S. (2011). Nubia-Arabia-Eurasia plate motions and the dynamics of Mediterranean and Middle East tectonics. Geophys. J. Int., 186: 971-979.

Ricou, L.E. (1995). The plate tectonic history of the past Teyhys Ocean. In: A.E.M. Nairn; L.E.Ricou, B. Vrielyncк and J. Dercourt (eds), The ocean basins and margins, 8: TheTethys Ocean. Plenum Press, New York, London, p. 3-70.

Sahawneh, J., and Atallah, M. (2002). Tectonic evolution of the north- eastern corner of the Dead Sea, Jordan, Abhath Al – Yarmouk, 11: 581-598.

Shahar, J. (1994). The Syrian Arc System: an overview. PALAEO, Elsiever Science, 112: 125-142.

Zain Eldeen, U., Delvaux, D., Jacobs, P. (2002). Tectonic evolution in the Wadi Araba Segment of the Dead Sea Rift, South-West Jordan. European Geosciences Union, 2: 1–19.

JJEES

JJEES (2019) 10 (3): 161-166
ISSN 1995-6681

Jordan Journal of Earth and Environmental Sciences

Green Synthesis of α-Fe_2O_3 Nanoparticles Using Pistachio Leaf Extract Influenced Seed Germination and Seedling Growth of Tomatos

Majd Abusalem[1], Akl Awwad[2], Jamal Ayad[1*], Azmi Abu Rayyan[1]

[1] University of Jordan, Department of Horticulture and Crop Science, Faculty of Agriculture, Jordan
[2] Royal Scientific Society, Department of Nanomaterials, Jordan

Received 7 April 2019; Accepted 19 May 2019

Abstract

The objective of this study is to assess the effects of the green synthesis of Hematite (α-Fe_2O_3) nanoparticles derived from pistachio (*Pistacia vera* L) leaves on seed germination and seedling growth of tomato (*Lycopersicon esculentum* L.). Hematite (α-Fe_2O_3) nanoparticles were synthesized using the pistachio leaves aqueous extract at ambient temperature. X-ray diffraction characterized the final product as crystalline α-Fe_2O_3 with the size of 40 nm. The seeds were then treated with different concentrations of α-Fe_2O_3 (10, 40, 80, 100 and 200 ppm). The transmission electron microscopy results reveal the presence of a network of randomly-oriented α-Fe_2O_3 spherical nanoparticles with an average size of 40 nm. The green synthesized α-Fe_2O_3 nanoparticles significantly improved seed vigor index, shoot length, fresh and dry weight of the tomato seedlings. Interestingly, lower concentration (10 ppm) of α-Fe_2O_3 nanoparticles improved the vigor index by 24 %, shoot length by 48.6 %, seedling fresh weight by 41 %, and seedling dry weight by 135 % compared to control ($p < 0.025$, $p < 0.001$, $p < 0.005$ and $p < 0.01$; respectively). Overall, the results of the current study show that the green synthesis of the nanoparticles from the pistachio leaves' extract holds promise in that the synthesized nanoparticles can enhance seed germination and seedling vigor of tomatos.

Keywords: Hematite nanoparticles, Pistachio vera, green synthesis, *Lycopersicon esculentum*.

1. Introduction

Iron-oxide nanoparticles have drawn the attention recently because they can improve the ability of plants to absorb iron oxides. Those nanoparticles (1–100 nm size) have distinctive physio-chemical characteristics that deliver iron oxides to plants efficiently (Ramimoghadam et al., 2014). Hematite (α-Fe_2O_3), the firmly-stable form of iron-oxide nanoparticles normally exists in rhombohedral crystal units and has an important role in research and technology (Kolen'ko et al., 2014). For example, it can be utilized as a startup for the synthesis of magnetite and maghemite. Moreover, the α-Fe_2O_3 nanoparticles have been widely utilized in soil decontamination, water quality, engineering (Dong et al., 2016), and agriculture (Asoufi et al., 2018).

Iron-oxide nanoparticles can be synthesized using several chemical and physical procedures. However, those procedures require costly and highly complicated equipments, tremendous pressure and temperature, additional purification procedures that could produce harmful derivatives and byproducts. Conversely, green synthesis has been suggested as an alternative because the manufacturing of metal-oxide nanoparticles using this approach is environmentally friendly and safe (Ahmmad et al., 2013).

Most of nanotechnology researches are concerned with adopting green synthesis to cope with the limitations of other common methods (Seabra et al., 2013). In general, plant tissue (Shameli et al., 2012), plant extracts (Parsons et al., 2007) and other parts of living plants (Jain et al., 2005) are used to synthesize nano-sized materials. This approach is environmentally safe, free from chemical contamination, less expensive, nontoxic, and can be utilized in biological applications (Groiss et al., 2017) in comparison to the commonplace chemical method where many noxious and permanent chemical substances are applied (Nadagouda et al., 2009). From the environment awareness point of view, green approaches are regarded as successful methods for producing metal nanoparticles. Also, when using the green method for Hematite production, it is not essential for the chemical to be stabilized and reduced, in addition to the fact that its manufacturing can be done under normal circumstances including temperature and pressure (Ren et al., 2017).

Using plant extracts in hematite production is simple, and is of a low cost. Moreover it entails utilizing bio-products which renders it acceptable as an eco-friendly method. Hematite nanoparticles have been synthesized using various plant species (Jagathesan and Rajiv, 2018), such as, *Camellia sinensis* (Hoag et al., 2009; Ahmmad et al., 2013), *Citrus reticulum* peels (Ali et al., 2017), *Cyprus rotundus* L. (Basavegowda et al., 2017), Roman nettle (Badni et al., 2016), and *Eucalyptus globules* (Madhavi et al., 2013). Limited research studies have documented the effects of iron-oxide nanoparticle on plants during germination (Pariona et al., 2017). Iron-oxide nanoparticles were found to increase germination in Chinese mung beans (Ren et al.,

* Corresponding author e-mail: ayadj@ju.edu.jo

2011), corn (Li et al., 2016) and oaks (Pariona et al., 2017). However, to the researchers' knowledge, no study has yet assessed the effects of the green-synthesis of hematite (α-Fe_2O_3) nanoparticles on seed germination and seedling growth of tomato plants. The present study was designed to synthesize hematite (α-Fe_2O_3) nanoparticles with a novel, rapid, clean, non-toxic, and environmentally acceptable green route. The approach of this study uses the iron salt precursor in the presence of pistachio leaves' aqueous extract via a single step reaction. This environmentally-friendly product (α-Fe_2O_3) was then used to investigate this research's objectives which hypothesized that the synthesized hematite (α-Fe_2O_3) nanoparticles can improve germination and growth parameters of tomato seeds.

2. Materials and Methods

2.1 Preparation of Pistachio Aqueous Extract

Mature Pistachio Leaves were collected from the local garden of the Royal Scientific Society, Jordan. The fresh green leaves were washed, cleaned and air-dried for seven days at room temperature (28 °C/ 15 °C, 41% relative humidity). Twenty grams of leaves were placed into 500 ml of deionized water and heated at 90°C for twenty minutes. The aqueous extract was cooled down and filtered through Whatman filter paper (porosity 25 µm) to remove the solid particles. Afterwards, the extract was stored in a glass bottle with a tight cover at room temperature to be used later for the synthesis of iron-oxides nanoparticles.

2.2 Preparation of Hematite (α-Fe_2O_3) Nanoparticles

The preparation of the α-Fe_2O_3 nanoparticles was conducted in the Royal Scientific Society Labs, Amman, Jordan. Four grams of iron nitrate nonahydrate ($Fe(NO_3)_3.9H_2O$; Sigma-Aldrich), used as a precursor for the Fe^{2+} ions, were dissolved in 400ml of de-ionized water under magnetic stirring at room temperature (27°C). Next, the prepared aqueous solution of the pistachio leaf extract (~ 100 ml) was progressively added to the iron-nitrate solution. The yellow color of the iron nitrate nonahydrate was changed to dark-red-brown indicating the formation of iron hydroxide. Then, a 5 % NaOH solution (99.5 %, BBC chemicals for lab) was added progressively in anticipation for the pH to reach the alkaline status (pH~10–12) and to act as a precipitation agent. The suspended red-brown particle solution was left under magnetic stirring for two hours. The suspension was purified with sterile de-ionized water three times. To get pure α-Fe_2O_3 nanoparticles, the precipitate was dried under vacuum, and was heated up to 550°C for two hours. The steps are demonstrated in equations 1-3 and in Figure 1. The prepared samples of the iron oxides were used for further characterization and for the nanoparticle synthesis.

$Fe(NO_3)_3.9H_2O + NaOH \rightarrow Fe(OH)_3 + 3NaNO_3 + 6H_2O$ . . Eq. 1

$Fe(OH)_3 \rightarrow FeOOH + H_2O$ . . . . . Eq. 2

$2FeOOH$ (Heated at 550°C/2h) $\rightarrow \alpha$-$Fe_2O_3 + H_2O$ . . . . . Eq. 3

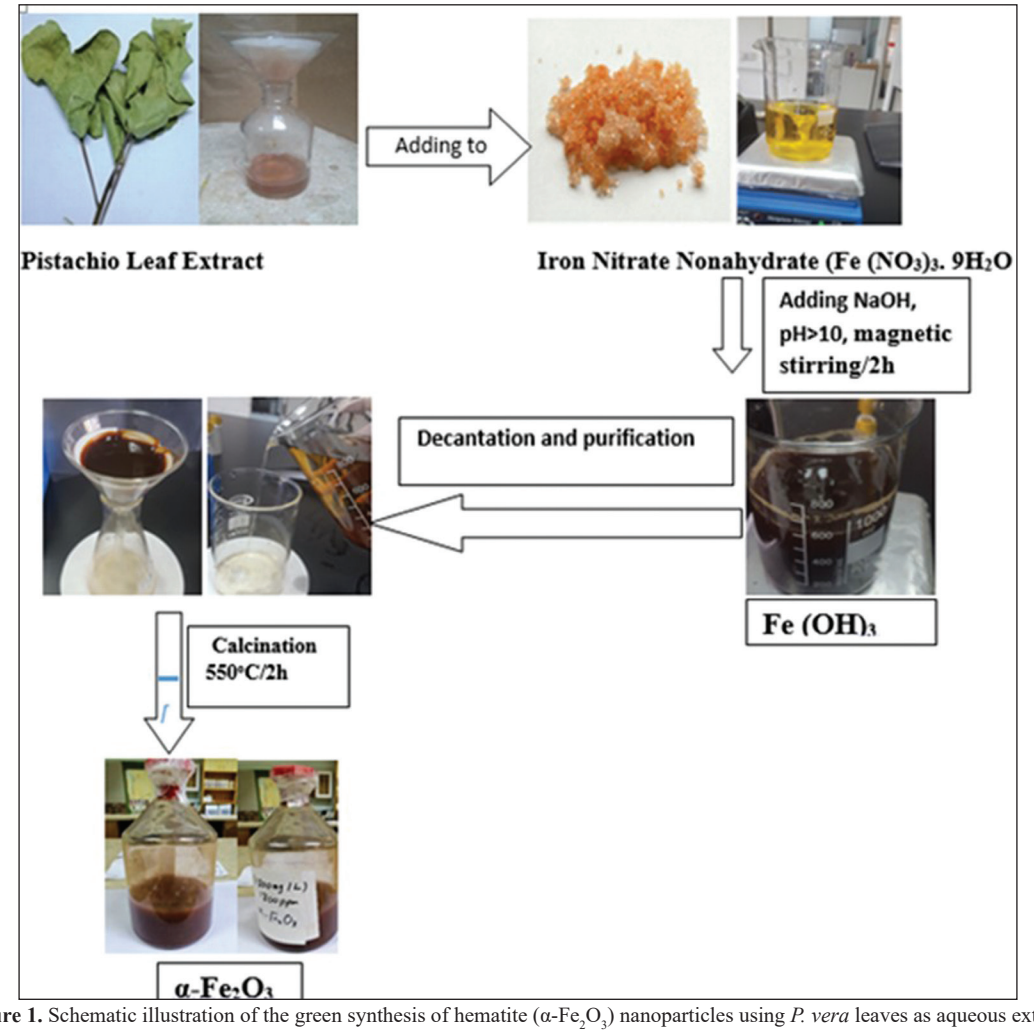

Figure 1. Schematic illustration of the green synthesis of hematite (α-Fe_2O_3) nanoparticles using *P. vera* leaves as aqueous extract.

2.3 Characterization of Hematite (α-Fe_2O_3) Nanoparticles

The Fourier transform infrared spectrophotometer (FT-IR, Shimadzu, IR-Prestige-21) was used to identify possible functional groups such as (NH, C=O carboxylic acid, C-N, OH phenols, OH alcohol, OH water) in the plant extract and in the synthesized hematite (α-Fe_2O_3) nanoparticles. The sample was scanned by X-ray diffraction (XRD-6000, Shimaduz) (λ=1.5405nm) within the 2θ range of (3^o -80^o) by applying the Debye–Scherer's equation (Awwad and Salem, 2012):

$$D = 0.9\lambda/\beta\cos\theta \quad \text{Equation 4}$$

where D is the crystallite size, λ is the X-ray wavelength, β is the full width at half maximum of the diffraction peak, and θ is the diffraction (Bragg) angle of the XRD spectra. The ultraviolet visible spectroscopy (SPUV-26, Sco-tech) was used to prove the forming and exact structure of the hematite (α-Fe_2O_3) nanoparticles in colloidal media. The transmission electron microscopy spectroscopy (TEM) (JEM-2100, JEOL Co.) was conducted to figure out the morphology, size, and distribution of the synthesized hematite (α-Fe_2O_3) nanoparticles.

2.4 Effect of Hematite (α-Fe_2O_3) Nanoparticles on Seed Germination of Tomatos

This experiment was carried out over the period from October 16-28, 2018 under laboratory conditions at the University of Jordan, Amman, Jordan. The impact of various concentrations of hematite nanoparticles on the germination of tomato seeds (*Lycopersicon esculentum* L. var Newton). The seeds were surface-sterilized with 50 % ethanol for one minute, and were rinsed once for one minute by 10 % commercial bleach (Sodium hypochlorite). Finally, they were washed extensively with sterilized water. One-hundred and eighty tomato seeds were grown in plastic trays (30cm x 10 cm). Thirty seeds per tray (three replicates and ten seeds per replicate) were used. Each tray was considered as an experimental unit. The seeds were wetted with 5 ml of six levels of hematite nanoparticles as follows: 0 (control), 10, 40, 80, 100, and 200 ppm. The trays were then covered tightly with transparent lids. The germination tests were performed according to the rules issued by the International Seed Testing Association (ISTA, 2009). The germination counts and seedling evaluations were performed daily for ten days. Seeds were considered germinated when the radical was emerged to a length of 2 mm. At the end of the experiment, the root and shoot fresh weights were measured using a four-digit balance. Germination indices such as germination percentage (G %), germination rate (GR) and Vigor index (VI) were calculated using the following equations:

$$\text{Germination percent (G \%)} = (Gf/N) \times 100 \quad \text{Equation 5}$$

Where Gf is the total number of germinated seeds at the end of experiment, and N is the total number of seeds used in the test.

$$\text{Germination rate (GR)} = (a/1) + (b-a/2) + (c-b/3) + \ldots + (nn-1/N) \quad \text{Equation 6}$$

Where a, b, c, and n are the numbers of the germinated seeds after 1, 2, 3, and N days from the start of imbibition.

$$\text{Vigor index (VI)} = SL \times G\ \% \quad \text{Equation 7}$$

Where SL is the seedling length (root length + shoot length), and G % is the germination percentage.

Root samples taken from the germinated seeds were scanned using a root scanner (Regent STD 1600+, Regent Instruments, QC, Canada). Root length and diameter and shoot length were measured using image analysis software, WinRhizo Pro (Regent Instruments). The root samples were then dried at 70°C for dry weight determination (Ayad, et al., 2010).

2.5 Statistical Analysis

Statistical analyses were conducted using SAS (version 9.4, SAS institute, Cary, NC). Significance was defined at $\alpha = 0.05$. The experiment was allocated using a complete randomized design (CRD) with three replications (ten subsamples) and six FeNPs concentrations. Data for each experimental unit were averaged and statistically analyzed. One-way ANOVA using General Linear Model (proc GLM) with the Fisher's LSD mean separation test were used to analyze the shoot length, root length, fresh weight, dry weight, germination percentage (G%), germination rate (GR), and vigor index (VI).

3. Results and Discussion

3.1 FT-IR Analysis

The FT-IR spectra of the *P. vera* aqueous leaf extract showed a distinctive broad and a peak (3433-3352 $cm^{-1)}$. This was attributed to the N-H stretching and bending vibration of amine group NH_2 and hydroxyl O-H (Figure 2). The overlapping of the stretching vibration is attributed to the water and the *P. vera* aqueous leaf extract molecules. The peaks at 2924 cm^{-1} and 2850 cm^{-1} are attributed to the stretching vibrations of -CH_2 and -CH_3 functional groups. The sharp band at 1724 cm^{-1} was a result of the amid carbonyl group as amide I and amide II, which appeared because of C=O and NH stretching vibrations in the amide linkage of the protein. The peaks at 1604, 1531, 1450, 1334, and 1207cm^{-1} can be attributed to the C-O group of polyols. The peaks around 1099 cm^{-1} might be ascribed to the C-N stretching vibrations of the aliphatic amines. These results agreed with the findings reported by Salem et al. (2013) upon the investigation of the P. vera aqueous leaves' extract FT-IR

The synthesized hematite (α-Fe_2O_3) nanoparticles are characterized by FT-IR spectra. This is normally to determine the probable biological molecules behind the oxidation of Fe^{3+}, capping, and the stabilization of nanoparticles. Figure 3 shows that the peaks at 3691 cm^{-1} and 3401 cm^{-1} are attributed to the O-H stretching -NH stretching and the bending vibration of amine NH_2 group in the P. vera leaf extract, and the overlap of the stretching vibration of O-H. The peak at 1358 cm^{-1} could be attributed to the asymmetric and symmetric stretching vibration of COO-. The presence of hematite (α-Fe_2O_3) nanoparticles was identified by the presence of two absorption bands approximately at 536 cm^{-1} and 455 cm^{-1}, which correspond to the Fe-O stretching bands of the bulk hematite (Fe_2O_3). These results indicate that the COO- groups were attached to the hematite particle surface. Generally, the observation indorses the existence of protein in the P. vera aqueous leaf extract, which acts as as an oxidizing and capping agent and as a stabilizer for the hematite nanoparticles.

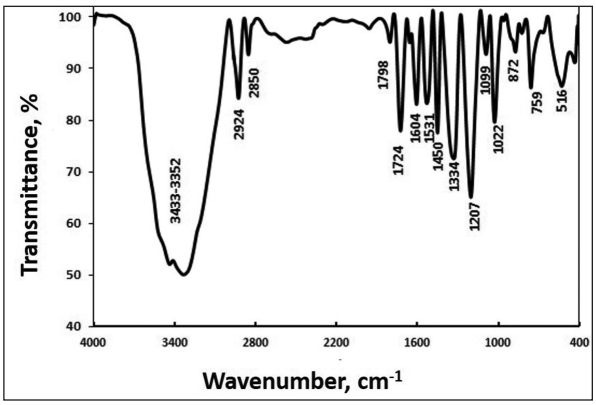

Figure 2. FTIR spectrum of P. vera aqueous leaves extract.

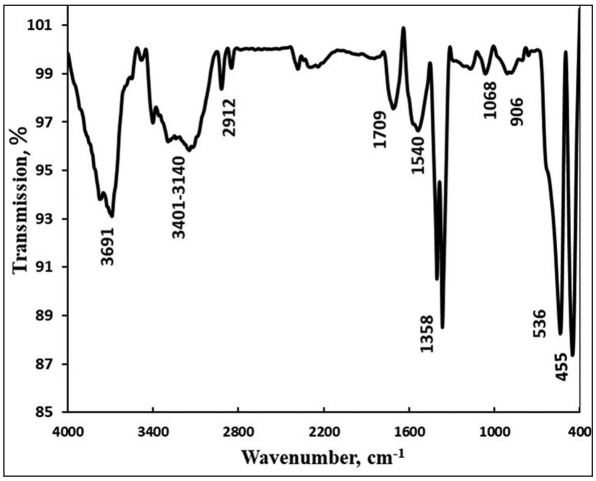

Figure 3. FT-IR spectrum of the synthesized hematite (α-Fe_2O_3) nanoparticles, heated at 550°C for 2h.

3.2 X- ray Diffraction (XRD) Analysis

The X-ray diffraction (XRD) verifies the crystalline configuration of synthesized α-Fe_2O_3 nanoparticles. The diffractogram in Figure 4 demonstrates the sharp peaks at twenty degree values 23.92°, 32.96°, 35.48°, 40.54°, 49.31°, 53.91°, 62.12°, and 63.76°. The exhibited peaks corresponded to 012, 104, 110, 113, 024, 116, 214, and 300 plans, respectively. The diffraction peaks are well-matched with Joint Committee on Powder Diffraction Standards (JCPDS) card no. 33-0664, endorsing that the α-Fe_2O_3 nanoparticles have a hexagonal crystalline configuration. Moreover, no further difraction peaks of other stages are detected, which signifies the high purity level of the α-Fe_2O_3 nanoparticles. The average crystallite size of the synthesized nanoparticles is 40 nm.

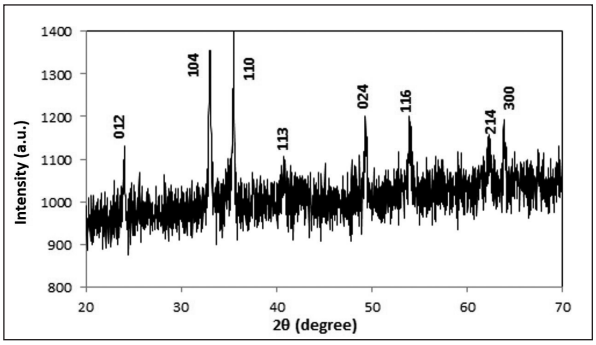

Figure 4. XRD pattern of the synthesized hematite (α-Fe_2O_3) nanoparticles.

3.3 UV-vis Spectroscopy Analysis

UV–visible spectroscopy is a spectral technique used to certify the formation and constancy of metal nanoparticles in aqueous solutions. Figure 5 shows that the UV–visible absorption of the α-Fe_2O_3 nanoparticles was the maximum in the wavelength range of 460-480 nm. The SPR bands of the colloidal iron nanoparticles were centered at around 480 nm for the α-Fe_2O_3 nanoparticles prepared by the green method (Figure 5). The reaction mixtures showed a single surface plasmon resonance (SPR) band; this demonstrates the spherical shape of the hematite nanoparticles, which was further confirmed by TEM images.

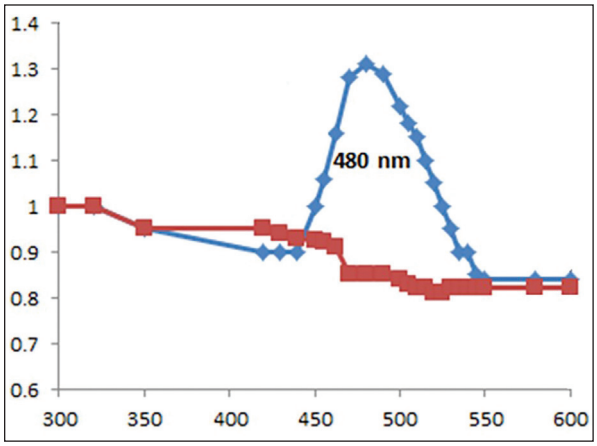

Figure 5. UV- vis absorption spectra of α-Fe_2O_3 (blue line) and *P. vera* leaves extract (red line).

3.4 TEM Analysis

The hematite (α-Fe_2O_3) nanoparticles are composed of invariable nanoparticles of a nearly spherical morphology with a narrow-size distribution (Figure 6). The nanoparticles size was in the range of 40 nm. It was very dependent on the type and concentration of the utilized base in the preparation process of hematite. However, a direct correlation governs the relationship between the base concentration and the resulted nanoparticle. This correlation was noticed by Lassoud et al. (2017).

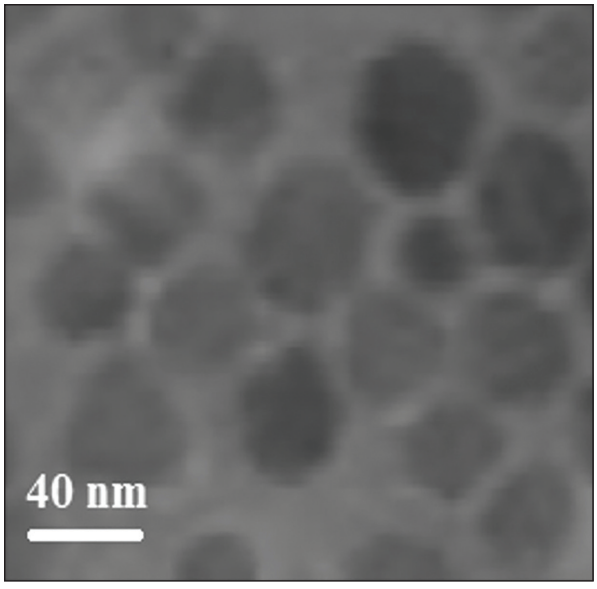

Figure 6. TEM micrograph of synthesized hematite α-Fe_2O_3 nanoparticles.

3.5 Seed Germination

The effect of the hematite nanoparticle concentrations on the germination percentage (G %), germination rate (GR), and vigor index (VI) of tomato seeds is shown in table 1. In the current study, priming tomato seeds before germination with hematite nanoparticles exhibited a higher vigor index across all treatments (10 to 200 ppm). At the 10 ppm treatment, the germination vigor index has improved by 24 % compared to the control. Seed vigor index is a key indicator of rapid germination and seedling establishment (Barpete et al., 2015). The uppermost vigor index level is linked with the superiority of the tomato plant (Var. newton) to perform more applicably at different concentrations of the α-Fe_2O_3 nanoparticles (10, 40 and 80 ppm). On the other hand, at higher concentrations (100 and 200 ppm), the seed vigor index had a negative impact on seed vigor compared to a lower concentration of the α-Fe_2O_3 nanoparticles (10 ppm). This may be attributed to the toxicity degree caused by higher concentrations as reported by Shankramma et al., (2016). Another explanation could be the status of the massing and clustering of nanoparticles in high concentrations which leads to block the nanoholes and reduce element uptake (Ren et al., 2011).

The application of α-Fe_2O_3 nanoparticles significantly increased seedling growth parameters (shoot length, seedling fresh and dry weights) compared to the control ($p < 0.001$, $p < 0.005$ and $p < 0.01$; respectively) (Table 2). Interestingly, the response of tomato seeds to a lower concentration (10 ppm) recorded better or similar results compared to high concentrations. At 10 ppm, the shoot length increased by 48.6 %, the seedling fresh weight by 41 %, and the dry weight by 135 % compared to the control. Overall, it is believed in this study that a low concentration (10 ppm) of α-Fe_2O_3 is adequate to induce vigor index and growth parameters in 'Newton' tomatoes.

Table 2. Effect of seed treatment with various hematite (FeNPs) concentrations on tomato seedling growth parameters. Different letters indicate statistically-significant differences among treatments ($P < 0.05$). NS not significant.

FeNPs (ppm)	Shoot length (cm)	Root length (cm)	Seedling fresh weight (g)	Seedling dry weight (g)
Control	3.62 d	7.47	0.17 c	0.017 b
10	5.38 a	7.11	0.24 ab	0.040 a
40	4.70 c	7.60	0.20 bc	0.037 a
80	4.74 bc	6.83	0.23 ab	0.040 a
100	4.93 bc	5.98	0.26 a	0.037 a
200	5.00 b	6.53	0.22 b	0.040 a
P value	*<.001*	*NS*	0.005	*0.01*

Although the biological indicators of phytotoxicity were not investigated in this study, the negative responses of seed germination, root and shoot length parameters to high α-Fe_2O_3 levels (e.g. 100 and 200 ppm) support the hypothesis that a high concentration of α-Fe_2O_3 can lead to phyto-toxicity (Kumar et al., 2015). In fact, Phyto-toxicity can lead to the reduction of germination and negative modifications of plant growth and oxidative-stress resistance (Chen et al., 2010; Rajeshwari et al., 2015). In this study, no negative impacts were detected on germination indices, and shoot and root length, which indicates that hematite (α-Fe_2O_3) nanoparticles (10 ppm, 40 ppm, 80 ppm, 100 ppm and 200 ppm) are not phytotoxic to the 'Newton' tomato seeds.

4. Conclusions

In this work, hematite (α-Fe_2O_3) nanoparticles were efficaciously prepared from P. vera leaves by an innovative green technique. Iron nitrate nonahydrate ions were utilized as a precursor and of the P. vera leaf aqueous extract as a stabilizing and capping agent. FTIR confirms the presence of Fe-O stretching vibration. The obtained results indicate that the synthesized hematite nanoparticles are spherically-shaped and are 40 nm in size. A low concentration of hematite (α-Fe_2O_3) nanoparticles (10 ppm) was adequate to promote seed vigor index and growth parameters compared to other higher concentrations. The current results confirm the promising potential of hematite (α-Fe_2O_3) nanoparticles to be utilized in seed priming and agricultural production.

Acknowledgments

The authors are thankful to the Deanship of Scientific Research, at the University of Jordan, in Amman, Jordan and to the Royal Scientific Society for providing all the facilities and support to carry out this research.

References

Ahmmad, B., Leonard, K., Islam M.S., Kurawaki, J.; Muruganandham, M., Ohkubo, T., Kuroda, Y. (2013). Green synthesis of mesoporous hematite (α-Fe_2O_3) nanoparticles and their photocatalytic activity. Advanced Powder Technology, 24(1): 160-167.

Ali, H.R., Nassar, H.N., El-Gendy, N.S. (2017). Green synthesis of α-Fe2O3 using Citrus reticulum peels extract and water decontamination from different organic pollutants J. Energy Sour., Part A: Recovery, Util. Environ. Effects, 39: 1425–1434.

Asoufi, H.M., Al-Antary, T.M., Awwad, A.M. (2018). Green route for synthesis hematite (α-Fe_2O_3) nanoparticles: Toxicity effect on the green peach aphid, Myzus persicae (Sulzer). Environmental Nanotechnology, Monitoring & Management, 9: 107-111.

Awwad, A.M., and Salem, N.M. (2012). Green synthesis of silver nanoparticles by mulberry leaves extract. Nanoscience and Nanotechnology, 2(4): 125-128.

Ayad, J.Y., Al-Abdallat, A.M., Saoub, H.M. (2010). Growth and yield of spring wheat and barley genotypes. International Journal of Botany, 6(4): 404-413.

Badni, N., Benheraoua, F.Z., Tadjer, B., Boudjemmaa, A., El Hameur, H., Bachari, K. (2016). Green synthesis of α-Fe_2O_3 nanoparticles using Roman nettle. Third International Conference on Energy, Materials, Applied Energetics and Pollution ICEMAEP2016, October 30-31, 2016 (Constantine, Algeria).

Barpete, S., Oğuz, M.C., Özcan, S.F., Anayol, E., Ahmed, H.A., Khawar, K.M., Özcan, S. (2015). Effect of temperature on germination, seed vigor index and seedling growth of five Turkish cotton (*Gossypium hirsutum* L.) cultivars. Fresenius Environ Bull, 24: 1-7.

Basavegowda, N., Mishra, K., Lee, Y.R. (2017). Synthesis, characterization, and catalytic applications of hematite (α-Fe_2O_3) nanoparticles as reusable nanocatalyst. Advances in Natural Sciences, Nanoscience and Nanotechnology, 8(2): 025017.

Chen, R., Ratnikov, T.A., Stone, M.B., Lin, S., Lard, M., Huang, G., Hudson, J.S., Ke, P.C. (2010). Differential Uptake of Carbon Nanoparticles by Plant and Mammalian Cells. Small 6: 612–617. http,//dx.doi.org/10.1002/smll.200901911

Dong, C.D., Chen, C.W., Hung, C.M. (2016). Magnetic nanoparticles and their heterogeneous persulfate oxidation organic compound applications. In Advanced Materials (pp. 23-35). Springer, Cham

Groiss, S., Selvaraj, R., Varadavenkatesan, T., Vinayagam, R. (2017). Structural characterization, antibacterial and catalytic effect of iron-oxide nanoparticles synthesised using the leaf extract of *Cynometra ramiflora*. Journal of Molecular Structure, 1128: 572-578.

Hoag, G.E., Collins, J.B., Holcomb, J.L., Hoag, J.R., Nadagouda, M.N., Varma, R.S. (2009). Degradation of bromothymol blue by 'greener' nano-scale zero-valent iron synthesized using tea polyphenols. Journal of Materials Chemistry, 19(45): 8671-8677.

International Seed Testing Association (ISTA). International Rules for Seed Testing. (2008). Bassersdrof, CH. Switzerland.

Jagathesan, G., and Rajiv, P. (2018). Biosynthesis and characterization of iron-oxide nanoparticles using Eichhornia crassipes leaf extract and assessing their antibacterial activity. Biocatalysis and agricultural biotechnology, 13: 90-94.

Jain, T.K., Morales, M.A., Sahoo, S.K., Leslie-Pelecky, D.L., Labhasetwar, V. (2005). Iron oxide nanoparticles for sustained delivery of anticancer agents. Molecular pharmaceutics, 2(3): 194-205.

Kolen'ko, Y.V., Bañobre-López, M., Rodríguez-Abreu, C., Carbó-Argibay, E., Sailsman, A., Piñeiro-Redondo, Y., Rivas, J. (2014). Large-scale synthesis of colloidal Fe_3O_4 nanoparticles exhibiting high heating efficiency in magnetic hyperthermia. The Journal of Physical Chemistry C, 118(16): 8691-8701.

Kumar, S., Patra, A.K., Datta, S.C., Rosin, K.G., Purakayastha, T.J. (2015). Phytotoxicity of nanoparticles to seed germination of plants. International Journal of Advanced Research, 3(3): 854-865.

Lassoued, A., Lassoued, M.S., Dkhil, B., Gadri, A., Ammar, S. (2017). Synthesis, structural, optical and morphological characterization of hematite through the precipitation method, Effect of varying the nature of the base. Journal of Molecular Structure 1141: 99-106.

Li, J., Hu, J., Ma, C., Wang, Y., Wu, C., Huang, J., Xing, B. (2016). Uptake, translocation and physiological effects of magnetic iron oxide (γ-Fe_2O_3) nanoparticles in corn (*Zea mays* L.). Chemosphere, 159: 326-334.

Madhavi, V., Prasad, T.N.V.K.V., Reddy, A.V.B., Reddy, B.R., Madhavi, G. (2013). Application of phytogenic zerovalent iron nanoparticles in the adsorption of hexavalent chromium. Spectrochimica Acta Part A, Molecular and Biomolecular Spectroscopy, 116: 17-25.

Nadagouda, M.N., Hoag, G., Collins, J., Varma, R.S. (2009). Green synthesis of Au nanostructures at room temperature using biodegradable plant surfactants. Crystal Growth & Design, 9(11): 4979-4983

Pariona, N., Martinez, A.I., Hdz-García, H.M., Cruz, L.A., Hernandez-Valdes, A. (2017). Effects of hematite and ferrihydrite nanoparticles on germination and growth of maize seedlings. Saudi journal of biological sciences, 24(7): 1547-1554

Parsons, J.G., Peralta-Videa, J.R., Gardea-Torresdey, J.L. (2007). Use of plants in biotechnology, synthesis of metal nanoparticles by inactivated plant tissues, plant extracts, and living plants. Developments in environmental science, 5: 463-485.

Rajeshwari, A., Kavitha, S., Alex, S.A., Kumar, D., Mukherjee, A., Chandrasekaran, N., Mukherjee, A. (2015). Cytotoxicity of aluminum oxide nanoparticles on *Allium cepa* root tip—effects of oxidative stress generation and biouptake. Environ. Sci. Pollut. Res., 22: 11057–11066. http,//dx.doi.org/10.1007/s11356-015-4355-4.

Ramimoghadam, D., Bagheri, S., Hamid, S.B.A. (2014). Progress in electrochemical synthesis of magnetic iron oxide nanoparticles. J. Magn. Magn. Mater, 368: 207–229.

Ren, G., Yang, L., Zhang, Z., Zhong, B., Yang, X., Wang, X. (2017). A new green synthesis of porous magnetite nanoparticles from waste ferrous sulfate by solid-phase reduction reaction. Journal of Alloys and Compounds, 710: 875-879

Ren, H. X., Liu, L., Liu, C., He, S.Y., Huang, J., Li, J.L., Gu, N. (2011). Physiological investigation of magnetic iron oxide nanoparticles towards chinese mung bean. Journal of biomedical nanotechnology, 7(5): 677-684.

Seabra, A.B., Haddad, P., Duran, N. (2013). Biogenic synthesis of nanostructured iron compounds, applications and perspectives. IET nanobiotechnology, 7(3): 90-99.

Salem, N.M., Ahmad, A.L., Awwad, A.M. (2013). New route for synthesis magnetite nanoparticles from ferrous ions and pistachio leaf extract. Nanoscience and Nanotechnology, 3(3): 48-51.

Shameli, K., Bin Ahmad, M., Jazayeri, S.D., Sedaghat, S., Shabanzadeh, P., Jahangirian, H., Abdollahi, Y. (2012). Synthesis and characterization of polyethylene glycol mediated silver nanoparticles by the green method. International journal of molecular sciences, 13(6): 6639-6650.

Shankramma, K., Yallappa, S., Shivanna, M.B., Manjanna, J. (2016). Fe2O3 magnetic nanoparticles to enhance *S. lycopersicum* (tomato) plant growth and their biomineralization. Applied Nanoscience, 6(7): 983-990.

JJEES

JJEES (2019) 10 (3): 167-172
ISSN 1995-6681

Jordan Journal of Earth and Environmental Sciences

Polycyclic Aromatic Hydrocarbon, Physio-Chemical Properties, and Culturable Microbial Flora of Human Urine-Impacted Topsoils at Commercial Tricycle Parks Along Benin-Sapele Expressway, Benin City, Nigeria.

Esosa Imarhiagbe* and Nosa Obayagbona

University of Benin, Department of Environmental Management and Toxicology, Nigeria

Received 12 February 2019; Accepted 26 May, 2019

Abstract

This study presents an evaluation of the microbiological, physiochemical, and poly aromatic hydrocarbon (PAH) properties of human urine-impacted topsoils from a commercial tricycle park located along Benin-Sapele expressway in Benin City. Several analytical procedures (pour plate method, spectrophotometry, atomic absorbance spectrophotometry, and gas chromatography) were utilized in the determination of the heterotrophic microbial flora, physiochemistry, heavy metal and PAH profiles of the topsoils. The heterotrophic bacterial and fungal counts for the urine-contaminated soils ranged from 8.1×10^4cfu/g to 18.9×10^4cfu/g and 4.4×10^4cfu/g to 8.0×10^4cfu/g, respectively. The heterotrophic bacterial and fungal counts for the control soils were 5.0×10^4cfu/g and 3.1×10^4cfu/g, respectively. The predominant bacterial and fungal genera were Bacillus sp., Klebsiella sp., Alcaligenes sp., Acinetobacter sp, Enterobacter sp., Micrococcus sp., Staphylococcus sp., Aspergillus sp., Penicillium sp., Trichoderma sp., and Candida sp. All the soils were acidic and sandy. The conductivity and organic carbon values for the urine-contaminated soils ranged from 960 µs/cm to 3240 µs/cm and from 3.58 % to 5.39 %. The potassium values for the contaminated soils ranged from 0.05 meq/100g to 0.12 meq/100g. Iron had the highest heavy metal concentration (788.0 mg/kg). The highest concentration of total hydrocarbon content was 43.6 mg/kg. The PAH values of the contaminated soils ranged from 1.47 mg/kg to 2.12 mg/kg. Considering the bio-magnification potentials of these chemical constituents within the ecological food webs and the disgusting stench and unhygienic nature of the urine-impacted environment, there is a need for increasing public awareness to discourage this low-esteemed human behaviour.

Keywords: Microbiological, physiochemical, poly aromatic hydrocarbon, human-urine, topsoils

1. Introduction

A soil environment refers to the weathered geological materials and biological residues that come into contact with the earth's atmosphere (Wilson and Artiola, 2004). The soil environment includes viable plants (roots), animals, and microorganisms that reside in the pore spaces, and are attached to the geological materials. According to Dada and Aruwa (2014), soil organic and inorganic matters are determinants of soil fertility, and they also aid the proliferation of various soil micro flora which in-turn play vital roles in the maintenance of the nutritional balance and geochemical cycles of the soil. The topsoil has the highest concentration of organic matter and microorganisms; it is where most of the Earth's biological soil activity occurs. The majority of microbial population is found in the topsoil and the number decreases as depth increases (Bridge and Spooner, 2001). The microbial population and types of biota found in soils depends on the Physiochemical quality of the soil. Different bacterial and fungal species thrive on various food sources and in different microenvironments in the soil (Dada and Aruwa, 2014).

Heavy metals have a great ecological significance due to their toxicity and accumulative behavior. Polycyclic Aromatic Hydrocarbons (PAHs) result from pyrolytic processes and originate mainly from anthropogenic processes, particularly from any incomplete combustion of organic fuels (matter) at high temperatures (Suchanová et al., 2008). Considering their carcinogenic and mutagenic properties, sixteen PAHs have been classified as priority pollutants by both the U.S. Environmental Protection Agency and the European Environment Agency, in addition to the fact that their health effects have been widely studied (Safo-Adu1 et al., 2014). Although air and drinking water may be responsible for some human exposure, the highest PAH intake is typically associated with their occurrence in diet (food) (Suchanová et al., 2008).

The basic urine constituents are urea, uric acid, minerals, chloride, nitrogen, sulphur, ammonia, copper, iron, phosphate, sodium, potassium, manganese, carbolic acid, calcium, salts, vitamins A, B, C, and E, enzymes, hippuric acid, creatinine, as well as lactose (Dada and Aruwa, 2014). Some possible effects of indiscriminate urination include disgust, damages to property value, impacting the quality of life for the people who have to live with the stench, and spreading diseases (Hoglund et al., 2002). Dada and Aruwa (2014) maintained that the proper disposal of human waste is important to avoid pollution and minimize the possibility of spreading diseases.

* Corresponding author e-mail: esosa.imarhiagbe@uniben.edu

The aim of this study is to evaluate the culturable microbial flora as well as the polycyclic aromatic hydrocarbon levels of human urine-impacted topsoils.

2. Materials And Methods

2.1 Collection of Soil Samples

Samples of topsoils contaminated with human urine were collected from different commercial tricycle parks sited along the Benin-Sapele-Warri expressway, Benin City, Edo State. The topsoil samples were collected with the aid of a standard soil auger at the depths of 0-20 cm; and were dispensed into a labelled sterile polythene bags. Also, a soil sample free of human urine contamination was collected from a sampling point 100 m away from contaminated vicinity along the Benin-Sapele-Warri expressway. The soil samples were immediately transported to the laboratory for analysis. Geographical Position System (GPS) coordinates of the sampling locations were N:06.29174, E005:63277^{o}; N:06.28186, E005:63396^{o}; N: 06.27500, E005:63277^{o}; N: 06.24243, E005:63761^{o}; N: 06.25882, E005:63667^{o} (control).

2.2 Enumeration and Isolation of Heterotrophic Bacteria and Fungi Using General Purpose Media

Ten grams of the respective soil samples were suspended in ninety millilitres (90 ml) of a sterilized nutrient broth in a conical flask. The soil suspension was thoroughly mixed and serially diluted using tenfold dilution. Appropriate dilutions were plated in duplicates on a sterile nutrient agar and potato dextrose agar for total heterotrophic bacterial counts and total heterotrophic fungal counts, respectively. The plates for the total heterotrophic bacterial counts were incubated aerobically at 35 ^{o}C for eighty-four hours; while one millilitre of antibiotic solution (chloramphenicol) was added to the potato dextrose agar plates to inhibit any possible growth of bacterial isolates on the fungal incubated plates at room temperature (28^{o}C ± 5^{o}C) for five days. After incubation, the counts obtained from the culture plates were recorded and expressed as the colony-forming unit per gram (cfu/g) of the original sample. The various isolates were further identified and characterized (Barnett and Hunter, 1975; Cullimore, 2000; Collins et al., 2004; Cheesbrough, 2006).

2.3 Determination of Polycyclic Aromatic Hydrocarbons (PAHs)

Ten grams of the soil samples were weighed into a solvent-rinsed beaker and 50 ml of 50:50 mixtures of acetone and dichloromethane (DCM) was added. The samples were spiked with 1ml of a surrogate mixture (orthoterphenyl-OTP) and placed in a sonicator for fifteen minutes at 20 ^{0}C. Ten grams of anhydrous sodium sulphate was then added to the sample and allowed to stand until a clear extract developed and was decanted. One milliliter (1ml) of the extracted samples was dissolved in n-hexane (HPLC grade) in order to elute the aliphatic hydrocarbons. The eluted samples were concentrated using a rotatory evaporator to about 3 ml, and was transferred into a teflone lined screwed vial and labeled for gas chromatography (GC) for the PAH analysis using Gas Chromatography (Agilent, Hewlett Packard 6890 series).

2.4 pH and Electrical Conductivity

Twenty grams of the air-dried soil samples was dispensed into a sterile beaker. Twenty millilitres (20 ml) of distilled water was added, and the mixture was stirred vigorously. The mixture was, then, allowed to stand for ten minutes before the pH was read using a calibrated pH meter. Also, a digital conductivity meter was used in determining the soil conductivity by dipping the sensitive rod into the mixture and a steady reading was taken.

2.5 Total Organic Carbon

Prior to analysis, 50 g of the soil was air-dried and sieved using a 2 mm metallic sieve. The soil was then ground to a fine consistency and re-sieved using a 0.5 mm metallic sieve. Approximately 0.5 g of the sieved soil was dispensed into a clean 250 ml conical flask and 10 ml of N $K_2Cr_2O_7$ and 10 ml of Conc. H_2SO_4 were, respectively, added to the flask. The mixture was shaken for one minute and allowed to cool. 60 ml of distilled water was added to the cooled solution to make the volume up to 150 ml, and the mixture was shaken and allowed to settle. Five millilitres (5 ml) of phosphoric acid and 8-10 drops of 1% diphenylamine solution were added, making the solution assume a dark violet color. This solution was titrated against 0.4 N ferron ammonium sulphur solution until a color change from violet to green was observed (Onyeonwu, 2000).

Calculation

%C = Titre × 0.24
%C = Bk – Titre × 0.24
Total Organic Carbon = (Bk – Titre) × 1.72.

2.6 Particle-Size Distribution

Fifty grams of the fine textured air-dried soil samples was transferred into a one-litre dispersion cup. One-hundred millilitres of freshly 0.1M sodium hydroxide solution was added to the dispersion cup. After thorough mixing, the mixture was placed on a mechanical shaker for four hours. The mixture was thereafter transferred to a (1 L) measuring cylinder, and the volume was made up to one litre with distilled water. The mixed solution inside the cylinder was shaken by inversion, and the time was noted. After forty seconds, a hydrometer was inserted into the cylinder, and at five minutes, the hydrometer scale was read and the temperature of the mixture was also noted. The hydrometer was withdrawn and the process was repeated three hours later (Onyeonwu, 2000).

Calculation

$$\text{(a) Silt + Clay\%} = \frac{\text{corrected hydrometer reading at 40 seconds}}{\text{Sample weight (g)}} \times 100\%$$

$$\text{(b) Clay\%} = \frac{\text{corrected hydrometer reading at 5 hours}}{\text{Sample weight (g)}} \times 100\%$$

(c) Sand (%) = 100 – (a) - (b).

2.7 Exchangeable Acidity

Five grams of air-dried soil was weighed and dispensed into a 150 ml plastic bottle. Fifty millilitres (50 ml) of potassium chloride was added and shaken mechanically for one hour. The mixture was filtered with the aid of Whatman filter paper No.1 into 250 ml conical flask. Thereafter, three to five drops of phenolphthalein indicator were added and titrated against the 0.05M NaOH until the colourless solution turned to pink (Onyeonwu, 2000).

Calculation

Exchangeble Acidity = 0.05M ×Titre × 20 meq/100g soil

2.8 Ammonium-Nitrogen

Prior to the estimation of the NH_4-N value of the soil samples, a filtered extract of the soil was prepared by weighing 10 g of the soil into 150 ml conical flask. Forty

(40 ml) millilitres of the extracting solution was added and shaken for thirty minutes. The solution was then filtered using a Whatman filter paper No 1. Five millilitres (5 ml) of the extract was pipetted into a clean beaker after which 2.5 ml of alkaline phenol, 1 ml of sodium potassium tartrate and 2.5 ml of sodium hypochlorite were added, respectively. The solution was shaken vigorously in between each addition, and the resultant solution was read at 636 nm (Onyeonwu, 2000).

Calculation

$$NH_4N \text{ (ppm as } \alpha/g \text{ for soil)} = \frac{IR \times SR \times Vol.}{Wt. \text{ of sample} \times Aliquot \text{ taken}}$$

IR: instrumental reading
SR: slope reciprocal
Vol: volume
Wt. of sample: weight of sample

2.9 Nitrate

Ten millilitres (10 ml) of the sodium acetate soil extract filtrate was pipetted into a 50 ml flask. Two millilitres (2 ml) of brucine and 10 ml of conc. H_2SO_4 were added sequentially. The resultant solution was mixed and allowed to stand for ten minutes. The solution was read spectrophotometerically at 470 nm (Onyeonwu, 2000).

Calculation

$$NO_3 \text{ (ppm as } \alpha/g \text{ for soil)} = \frac{IR \times SR \times Vol}{Wt. \text{ of sample} \times Aliquot \text{ taken}}$$

IR: instrumental reading
SR: slope reciprocal
Vol: volume
Wt. of sample: weight of sample

2.10 Sulphate

Ten millilitres (10 ml) of the sodium acetate soil extract filtrate was transferred into 50 ml conical flask. The volume of the filtrate was made up to 20 ml by the addition of 10 ml of distilled water. One millilitre (1 ml) of gelatine – $BaCl_2$ reagent was added, and the mixture was shaken and allowed to stand for thirty minutes. The solution was read at 420 nm (Onyeonwu, 2000).

Calculation

$$SO_2 \text{ (ppm as } \alpha/g \text{ for soil)} = \frac{IR \times SR \times Colour\ Vol. \times Extra.\ Vol.}{Wt. \text{ of sample} \times Aliquot \text{ taken}}$$

IR: instrumental reading
SR: slope reciprocal
Vol: volume
Wt. of sample: weight of sample

2.11 Chloride

Ten millilitres (10 ml) of the sodium acetate soil extract filtrate was transferred into a 250 ml conical flask. Three drops of K_2CrO_4 were added, and the solution was titrated against 0.05 M silver nitrate until the formation of slight red precipitate (Onyeonwu, 2000).

Calculation

$$Cl^- \text{ (}\alpha/g \text{ for soil)} = \frac{Molarity \times Titre \times Vol. \times 1000}{Wt \text{ of sample} \times Aliquot \text{ taken}}$$

Vol: volume
Wt. of sample: weight of sample

2.12 Cation Exchangeable Bases (Na, K, Ca, Mg)

Five grams of the air-dried soil was weighed into a conical flask. One-hundred milliliters (100 ml) of neutral 1 M ammonium acetate was then added to the soil, and the mixture was shaken with the aid of a mechanical shaker for thirty minutes. The mixture was filtered using a Whatman filter paper No 42 into a 100 ml volumetric flask. The filtrate was made up to mark with acetate. Stock working standards 0, 2, 4, 6, 8, and 10 ppm were prepared for sodium, potassium, calcium, and magnesium, and the concentration of the exchangeable cations (Na, Ca, K and Mg) in the filtrate was determined using a flame photometer. The utilized blank was ammonium acetate (Onyeonwu 2000).

Calculation

$$Ca \text{ (Meq/100g)} = \frac{Instrument\ reading}{Weight \text{ of sample} \times Eq.\ wt.} \times 100\%$$

$$K \text{ (Meq/ 100g)} = \frac{Instrument\ reading}{Weight \text{ of sample} \times Eq.\ wt.} \times 100\%$$

$$Mg \text{ (Meq/ 100 g)} = \frac{Instrument\ reading}{Weight \text{ of sample} \times Eq.\ wt.} \times 100\%$$

$$Na \text{ (Meq/ 100 g)} = \frac{Instrument\ reading}{Weight \text{ of sample} \times Eq.\ wt.} \times 100\%$$

2.13 Determination of Heavy Metals:

The soil was sieved, and 5 g of the soil samples was taken from the sieved soil and dispensed into a beaker. Ten milliliters (10 ml) of nitric acid was added to the sample. The sample was digested at 105°C for forty-five minutes after which it was allowed to cool to room temperature. The cooled digest was washed into a standard volumetric flask, and was made up to the mark with distilled water (Onyeonwu, 2000). The heavy metals (Pb, Cd, Mn Fe, Cu, Cr, Ni, V, and Zn) levels were analyzed using an Atomic Absorbance Spectrophotometer (AAS) (MODEL-SOLAAR 969 UNICAM SERIES).

2.14 Determination of Total Hydrocarbon Content

One gram of the air-dried soil samples was dissolved in 10 ml of hexane and shaken for ten minutes using a mechanical shaker. The solution was filtered using a Whatman filter paper No. 42, and absorbance was read at 460 nm (Akpoveta et al., 2011).

$$THC \text{ (mg/Kg)} = \frac{OD\ reading \times Volume\ of\ Solvent\ Used}{Weight\ of\ soil\ sample\ (Kg)}$$

3. Results

The results of heterotrophic bacterial and fungal counts were in the order of 10^4 cfu/g for both (table 1 A). The heterotrophic bacterial and fungal counts for the control were 5.0×10^4cfu/g and 3.1×10^4cfu/g, respectively (Table 1). The heterotrophic bacterial counts and heterotrophic fungal counts for the urine-contaminated soils ranged from 8.1×10^4cfu/g for sample 4 to 18.9×10^4cfu/g for sample 2, and from 4.4×10^4cfu/g for sample 4 to 8.0×10^4cfu/g for sample 3, respectively. The culturable microbial isolates were: Bacillus sp., Klebsiella sp., Alcaligenes sp., Acinetobacter sp., Enterobacter sp., Micrococcus sp., Staphylococcus sp., Aspergillus sp., Penicillium sp., Trichoderma sp., and Candida sp. The most dominant bacterial isolates were Bacillus sp., Enterobacter sp.. Micrococcus sp. was isolated from all the soils, whilst Aspergillus sp. and Penicillium sp. were the dominant fungal isolates (table 1B).

The results of the physiochemical analysis are shown in table 2. All the soils were acidic (pH ranging from 4.28 to 5.82) and sandy (ranging from 91.1 % to 92.4 %). The conductivity and organic carbon values for the urine-contaminated soils ranged from 960 µs/cm for sample 3 to 3240 µs/cm for sample 1, and from 3.58 % for sample 3 to 5.39 % for sample 1. The sodium and potassium values for the contaminated soils ranged from 1.09 meq/100g for sample 3 to 1.84 meq/100g for sample 1, and from 0.05 meq/100g for sample 2 to 0.12 meq/100g for sample 3. The

calcium, magnesiumm and chloride values for the urine-contaminated soils ranged from 2.85 meq/100g for sample 3 to 3.95 meq/100g for sample 1, 0.74 meq/100g for sample 1 to 1.20 meq/100g, and from 89.4 mg/kg for sample 3 to 177.7 mg/kg for sample 1. The ammonia-nitrogen and nitrate content of the urine-contaminated soils ranged from 8.48 mg/kg for sample 3 to 15.6 mg/kg for sample 1, and from 10.4 mg/kg for sample 3 to 15.2 mg/kg for sample 1. The sulphate and exchangeable acidity values for the contaminated soils ranged from 7.4 mg/kg for sample 3 to 17.0 mg/kg for sample 1, and from 0.6 meq/100g for sample 4 to 1.3 meq/100g for sample 2.

The results of the heavy-metal analysis of the soils are presented in table 3. Iron had the highest concentration, which ranged from 162.2 mg/kg (control) to 788.0 mg/kg (sample 1). This was followed by manganese with a range of 12.4 mg/kg (control) to 67.7 mg/kg (sample 1). The PAHs values for the soils are shown in table 4. The total concentration of PAHs ranged from 0.10 mg/kg (control) to 2.05 mg/kg (sample 2).

Table 1A. The heterotrophic microbial counts of the urine-contaminated and control soils

Soil samples	Total Heterotrophic Bacterial count ($\times 10^4$cfu/g)	Total heterotrophic fungal count ($\times 10^4$cfu/g)
Control	5.0	3.1
Location 1	16.8	7.5
Location 2	18.9	7.1
Location 3	17.2	8.0
Location 4	8.1	4.4

Table 1B. Occurrence of the microbial isolates in the soils

Sample Code	Bacterial isolates present	Fungal isolates present
Control	Bacillus sp., Enterobacter sp., Micrococcus sp., Alcaligenes sp.	Aspergillus sp., Penicillium sp.
Location 1	Bacillus sp., Staphylococcus sp., Enterobacter sp., Micrococcus sp.	Aspergillus sp., Penicillium sp., Candida sp.
Location 2	Bacillus sp., Acinetobacter sp., Micrococcus sp.	Aspergillus sp., Penicillium sp.
Location 3	Bacillus sp., Klebsiella sp., Enterobacter sp., Micrococcus sp.	Aspergillus sp., Trichoderma sp., Penicillium sp., Candida sp.
Location 4	Bacillus sp., Enterobacter sp., Micrococcus sp., Staphylococcus sp.	Aspergillus sp., Penicillium sp., Candida sp.

Table 2. Physiochemical values of the urine-contaminated and control soils

Soils	pH	EC	Org.C	EA	Na	K	Ca	Mg	Cl	THC	NH_4N	NO_3	SO_4	Clay	Silt	Sand
		(µS/cm)	(%)	(meq/100g)						(mg/kg)					(%)	
Control	5.82	270	1.51	0.4	0.63	0.12	0.96	0.50	37.5	2.17	2.28	3.36	1.62	5.9	2.5	91.6
Location 1	4.28	3240	5.39	1.1	1.84	0.09	3.95	0.74	177.7	43.6	15.6	15.2	17.0	6.9	1.8	91.3
Location 2	4.36	2950	4.22	1.3	1.29	0.05	3.11	0.88	143.6	35.2	11.9	13.5	14.8	5.4	2.2	92.4
Location 3	4.93	960	3.58	0.9	1.09	0.12	2.85	0.91	89.4	25.3	8.48	10.4	7.4	6.1	2.5	91.4
Location 4	5.20	1210	4.18	0.6	1.36	0.10	3.07	1.20	125.2	17.0	9.47	12.3	9.1	5.8	3.1	91.1

KEY: EC; Electrical conductivity, T. N; Total nitrogen, Org. C; Organic Carbon, EA; Exchangeable acidity, THC: Total Hydrocarbon content

Table 3. Heavy-metal values of the urine-contaminated and control soils

Code	Fe (mg/kg)	Mn (mg/kg)	Zn (mg/kg)	Cu (mg/kg)	Cr (mg/kg)	Cd (mg/kg)	Pb (mg/kg)	Ni (mg/kg)	V (mg/kg)
Control	162.2	12.4	1.0	0.0	0.0	0.0	0.03	0.03	0.0
Location 1	788.0	67.7	5.1	0.0	0.0	0.0	3.0	1.0	0.0
Location 2	729.1	54.2	2.0	0.0	0.0	0.0	2.5	1.0	0.0
Location 3	531.3	28.4	5.9	0.0	0.0	0.0	2.0	0.1	0.0
Location 4	685.1	32.6	4.2	0.0	0.0	0.0	1.1	0.7	0.0

Table 4. Poly aromatic hydrocarbon values of the urine-contaminated and control soils

Sample Code	Control	Location 1	Location 2	Location 3	Location 4
COMPONENT					
Naphthalene	0	0	0	0.07	0
Acenaphthylene	0	0	0	0.30	0
Acenaphthene	0	0	0	0	0
Fluorene	0	0	0.27	0.17	0
Phenanthrene	0	0	0.19	0.08	0.32
Anthracene	0	0	0	0	0
Fluoranthene	0	0.18	0.40	0	0
Pyrene	0	0.15	0	0	0.35
1,2-Benzothracene	0	0	0.30	0.11	0
Chysene	0	0	0	0	0
Benzo(b)fluoranthene	0	0.45	0	0	0
Benzo(k)fluoranthene	0	0	0	0	0.36
Benzo(a)pyrene	0	0.08	0.23	0.18	0.35
Dibenzo(a,h)anthracene	0	0.53	0.22	0.41	0.04
Benzo(g,h.i) perylene	0.04	0.10	0.21	0.08	0.06
Indeno(1,2,3-cd)pyrene	0.06	0.04	0.30	0.07	0.06
Total mg/kg	**0.10**	**1.53**	**2.12**	**1.21**	**1.54**

4. Discussion

Expectedly, the culturable microbial flora of the human-urine-impacted soil samples was comparatively higher than the counts recorded for the control soil (table 1). This trend was collaborated by the higher conductivity, total hydrocarbons, and macro nutritional values of the contaminated soils in comparison with the control soil (table 2). These trends suggest possible characteristic changes on the microbial diversity and physiochemical status of the exposed soil as a result of continuous urine contamination. The microbial isolates identified from the examined soils were similar to the isolates reported by Dada and Aruwa (2014) who investigated the culturable microbial flora of human urine-impacted soils collected from around lecture theatres within the Federal University of Technology, Akure. The isolation of gram-positive bacterial cultures such as Bacillus sp. and Micrococcus sp. (table 1B) was not surprising, given the fact that these organisms are normally present in tropical soils and are also known to withstand adverse environmental conditions. Dada and Aruwa (2014) reported that the micrococci are known to grow well in environments with little water or high salt concentrations. They also described the Bacillus species as versatile chemo-heterotrophs capable of respiration using a variety of simple organic compounds (sugars, amino acids, organic acids). Also, expectedly, Aspergillus sp. and Penicillium sp. were isolated from all the studied soils (table 1B). These filamentous micro fungi are known to be ubiquitously distributed in the environment especially in the soil and air niches. The pH values of the urine-polluted soils were comparatively lower than the values indicated by the control soil (table 2). This phenomenon might be ascribed directly to the effect of the urine on the topsoil. Dada and Aruwa (2014) reported the same trend and stated that fungal growth favours low pH more than a bacterial growth in the urine-contaminated soils.

The presence of heavy metals and poly cyclic aromatic hydrocarbon in the studied soil samples (tables 3 and 4) may be attributed to the impact of anthropogenic activities or practices in the area. Examples of some of these practices include: vehicular emissions and indiscriminate disposal of refined petroleum products and used batteries. The heavy-metal concentrations in the control soil were comparatively lower than levels recorded in the urine-contaminated soils (table 3). This trend might also be attributed to natural factors such as the elemental composition of the underlying parent rock material from which the soil was formed. The possible source of the PAHs in the soils can be attributed to the deposition of refined petroleum products on the soils over time. The detection of PAHs in both the control and the urine-impacted soils could be a reflection of the ubiquitous distribution of these compounds in the soils. However, this trend is relevant to public health because these compounds

are known to have a lipophilic nature, and because heavy metals and PAHs have a high potential for biomagnification through trophic transfers (Clements et al., 1994). From the results of this study, dibenzo (a, h) anthracene, benzo (b) fluoranthene, benzo (k) fluoranthene, benzo (a) pyrene, pyrene and phenanthrene were generally observed to be high among the PAH tractions.

5. Conclusions

Considering the bio-magnification potentials of these chemical constituents within the ecological food webs, the chemical contents of primary producers, such as plants growing around urine- impacted soils, should be investigated. The disgusting-stench and unhygienic nature of the urine impacted environments also call for the need to increase public awareness for the sake of discouraging this low-esteemed human behaviour.

References

Akpoveta, O.V., Egharevba, F., Medjor, O.W., Osaro, K.I., Enyemike, E.D. (2011). Microbial degradation and its kinetics on crude oil polluted soils. Research Journal of Chemical Sciences 1(6): 8-14.

Barnett, H.L., and Hunter, B.B. (1975). Illustrated Genera of Imperfect Fungi.3rdEd. Burgess, New York, 225 pp.

Bridge, P., and Spooner, B. (2001). Soil fungi: Diversity and detection. Plant and Soil 232 (12):147-154.

Cheesbrough, M. (2006). District Laboratory Practice in Tropical Countries.Cambridge University press, Cambridge, 434 pp.

Clements, W., Oris, J., Wissing, T. (1994). The effects of chemical structure and exposure on the microbial degradation of polycyclic aromatic hydrocarbons in fresh water and estuarine ecosystems. Environ Toxicol Chem., 6:535-546.

Collins, C.H., Lyne, P.M., Grange, J.M., Falkinham, J.O. (2004). Collins and Lyne's Microbiological Methods, 8th Ed. Arnold Pub., London, 465 pp.

Cullimore, D.R (2000). Practical Atlas for Bacterial Identification.CRC Press, 209 pp.

Dada, E.O., and Aruwa, C.E. (2014). Microorganisms associated with urine contaminated soils around lecture theatres in Federal University of Technology, Akure, Nigeria. International Journal of Applied Microbiology and Biotechnology Research 2: 79-85.

Hoglund, C., Ashbolt, N., Strenstrom, T.A. (2002). Microbial risk assessment of source-separated urine used in agriculture. Waste Management Research 20:162-171.

Onyeonwu, R.O. (2000). Manual for Waste/Wastewater, Soil/ Sediment, Plant and Fish analysis. MacGill Environmental Research Laboratory Manual. Benin City, 81 pp.

Safo-Adu1, G., Ofosu, F.G., Carboo, D., Serfor – Armah, Y. (2014). Health risk assessment of exposure to particulate polycyclic aromatic hydrocarbons at a tollbooth on a major highway. American Journal of Science and Industrial Research 5(4): 110-119.

Suchanová, M., Hajšlová, J., Tomaniová, M., Kocourek, V., Babička L. (2008). Polycyclic aromatic hydrocarbons in cheese. Journal of Science Food Agriculture 88(8):1307-1317.

Wilson, L.G., and Artiola, J.F. (2004). Soil and vadose zone sampling. Pp 101-119, In: Artiola JF, Pepper IL and Brusseau ML (Eds.), Environmental Monitoring and Characterization. Elsevier Science and Technology Books, New York.

JJEES

JJEES (2019) 10 (3): 173-177
ISSN 1995-6681

Jordan Journal of Earth and Environmental Sciences

Risk Evaluation of Heavy Metals in Soils Irrigated with Afra Thermal Water Springs, Jordan

Amjed Shatnawi[1*], Anwar Jiries[2], Mohammad Emereen[2]

[1] Al al-Bayt University, Institute of Earth and Environmental Sciences, Jordan
[2] Mutah University, Faculty of Science, Jordan

Received 20 December, 2018; Accepted 31 May, 2019

Abstract

The present study investigates the concentrations of six heavy metals (Cu, Ni, Co, Zn and Cr) in Afra thermal springs in Tafila, southern Jordan and their accumulations in soils irrigated by this hot spring water. Thermal water samples were collected during two seasons that is at the end of summer and at the end of the winter season, 2012-2013.

The results show that the concentrations of heavy metals in the soil were relatively low. This was attributed to their low concentrations in the control samples as well as in the thermal water.

The current study investigates water quality in Afra thermal springs in Jordan in terms of heavy metal concentrations. It shows relatively low concentrations and a great variation with seasons. Heavy metal concentrations at the end of winter (in ascending order) were $C_{Cu} > C_{Ni} > C_{Co} > C_{Zn} > C_{Cd}$, whereas at the end of the summer season, they were: $C_{Co} > C_{Ni} > C_{Cu}$. All analyzed metals in the thermal spring water were below the WHO guidelines for drinking water except Ni which showed higher concentrations than those set by the WHO guidelines.

As for soil analysis, the results showed that most of the detected heavy metals were related to pedogenesis rather than to the accumulation from irrigation with thermal water. However, there is an increase in all metals in soils irrigated with thermal springs compared to the control sample, which indicates that there is an accumulation of heavy metals coming from the thermal springs through successive irrigation.

Keywords: Afra Thermal springs, Heavy metal, soil, Jordan.

1. Introduction

Heavy metals are natural constitutes of natural water and their concentrations in the environment depend on the lithology of the aquifer as well as the physiochemical characteristics of the water. The damage resulting from heavy metal accumulation in the soil is difficult to cure as metals cannot be chemically degraded (Salt et al., 1995)

Thermal springs are natural geological phenomena found in all five continents. Geothermal springs are known to be rich in heavy metals which may be attrbiuted to the water rock interaction in the deep aquifers because the chemical composition of the thermal waters reflects the geological formations of the aquifer at depth (Oliver et al., 2008), and the minerals are released through water rock interaction in the deep aquifers.

The chemistry of spring waters reflects the interaction of groundwater with the aquifer host rock as well as any chemical constituents that may be introduced from surface sources. Spring water chemistry is not intrinsically different from groundwater chemistry. The temperature of the hot springs depends on the temperature of the aquifer as well as the speed of water coming to the surface; at a less chance it has to cool down, thus it would be hotter (Durowoju et al., 2016). The solubility of many minerals increases with increasing the temperatures which makes thermal water capable of dissolving minerals over time enriching thermal springs with trace elements (Stauffer et al., 1980). As the hot springs discharge its water at the earth surface, the high concentration of metals will be deposited near the earth surface accumulating in the soil as a result of the changing physiochemical conditions of the water.

Thermal springs have been intensively investigated in the Mediterranean region. In Tunis, an investigation of the deep and shallow geothermal systems in southwestern Tunisia showed that the thermal upward movement of the thermal water from the deep aquifers to the shallow ones is probably due to the abundant fractures in the research area (Ben Brahim, 2013). Also, an isotopic investigation was done by Katsanou et al. 2012 at the Hamamayagi thermal spring in Turkey and showed that the d18O–d2H isotope ratios clearly indicate a meteoric origin for the waters. Another investigation was done by Pasvanoglu et al. (2012) who demonstrated that the thermal-water springs of Banaz area in Tukey have a meteoric origin as the rainwater which percolates downwards along fractures and faults, is heated at depth, and then rises to the surface along fractures and faults which resemble and act as a hydrothermal conduit.

More than ten thermal springs can be found In Jordan, mainly along the eastern flank of the Jordan valley extending from the Yarmouk River in the north to Tafileh province in the south with temperatures ranging from 30°C to 63°C. The main sources of heat for these springs are mainly the hot igneous rocks beneath these springs.

* Corresponding author e-mail: amjedshatnawi@yahoo.com

However, Sawarieh (2008) reported that the source of heat for the thermal water in the lower aquifer is a result of the deep circulation of water within the Paleozoic sandstones receiving heat from normal to slightly elevated geothermal gradient.

The water of some thermal springs to the east of the Dead sea (Main hot spring) originate from three end members mixed with an old groundwater (many thousands of years) at the Dead Sea water under a normal geothermal gradient (Salameh and Rimawi, 1984). A recent investigation of heavy metal concentrations at Main hot springs was found to be higher than the permissible limits set by international organizations (Shakhatreh et al., 2017).

Water quality of cold springs at NW of Afra thermal springs was investigated by Tarawneh et al. (2000). They found that the pollution of the investigated springs comes from surface sources rather than form within the groundwater.

In north Jordan, within Yarmouk basin, Batayneh (2010) found that heavy metal levels in some springs exceeded the Jordanian permissible limits. Schaeffer and Sass, (2014) reported that the shallow aquifer system in Jordan are overexploited in a way that the thermal water system will be affected in quality and quantity increasingly.

Irrigation with thermal water can contaminate the soil with heavy metals. For example, agriculture rice soils irrigated with thermal water during drought seasons in the Gunda plain, northern Taiwan, were reported to be contaminated with Fe, Cu, Mn, Cr, Ni, Zn especially in the deep layers (60-80 cm).

Among the well-known thermal springs in south Jordan is Afra thermal springs which is located at around 30 Km north of Tafila city at altitudes ranging from 304 to 326 m above sea level. The aim of this study is to investigate heavy metal concentrations in Afra thermal water as well as their accumulation in the soils irrigated from a stream fed by the effluent water produced from Afra thermal springs.

2. Study area

Tafila province is characterized by the presence of more than 360 springs of different temperatures. Afra geothermal springs consists of fifteen springs located about 30 km north of Tafila city, on the western limb of Sharah Mountain extending between longitudes (35° 34′) , and (35° 38′) and latitudes (30° 52′) and (31° 00′) (Figure 1).

The geothermal system consists of springs with an overall discharging rate of around 500l/sec ranging at a rate of 3.5-80 l/s for each different spring. The temperatures of the springs ranging between 44.5 and 46.3 °C originate from a different aquifer. The thermal water presently flows through open channels to pools, used for swimming and treatment of skin diseases. After being used, the water is discharged to nearby fields where it is used for irrigation purposes. The investigated spring (Afra) originates from the lower cretaceous sandstone underlying gravel beds (Harahsheh, 2002).

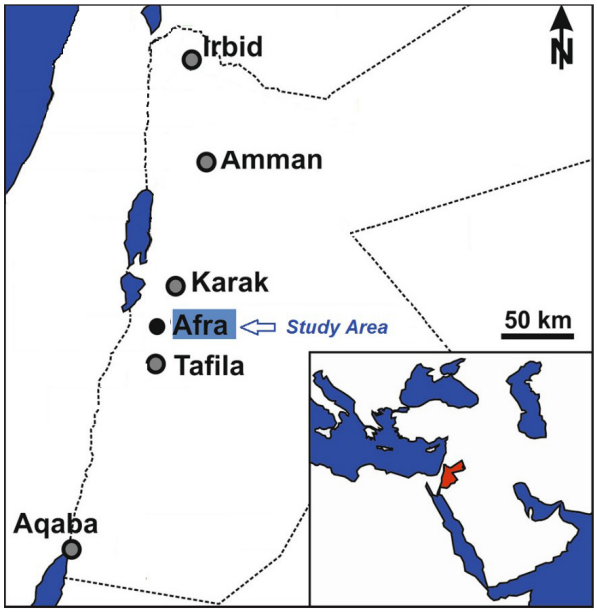

Figure 1. Location map

3. Materials and Methods

The Afra thermal spring water and soils irrigated with streams produced from the thermal springs were investigated in terms of six heavy metals (Zn, Cu, Co, Cr and Ni) for both the soil and water samples.

The water samples were collected at two periods: during March representing the end of the winter season and at the end of summer to show the distribution and potential risks of heavy metals with time.

A 250 ml PVC bottles were used after being washed with 10 % nitric acid. Also the bottles were washed several times with sample water before sampling. Few drops of concentrated nitric acid were added to each bottle to eliminate the precipitation of heavy metals during transportation.

The collected water samples were transferred to the laboratories of "Jordan Abyad Fertilizers and chemicals company and were analyzed within few days after sampling to eliminate any change in their composition.

Soil sampling was carried out only at the end of the winter season from a site located downstream from the Afra thermal water where the source of irrigation water is the effluent water discharge from Afra thermal springs. An additional site was selected where no irrigation is practiced and is considered as a blank sample.

Soil samples from each location were collected from two depths (0-10, and 10-20 cm). All of the samples were in triplicates to ensure reliability of the results. The samples were then transferred to the laboratory at Mutah University for digestion and analysis.

Each sample was oven-dried at 105°C until constant weight was achieved indicating the removal of soil moisture. After drying, each sample was sieved through a 2mm plastic mesh to remove large particles and plant remains from the soil.

For each Soil samples, 1 to 2 grams of the soil was accurately weighed and placed in the test tube, and 10 mL of concentrated nitric acid was added and sonicated for one hour at 90°C (Hewitt et al., 1990). The samples were left to

cool, and the contents were filtered through Whatman filter paper No.42. Solutions were made up to a final volume of 25 ml using 1 % nitric acid in polyethylene volumetric flasks.

The digested soil samples were transferred to the laboratories of "Jordan Abyad Fertilizer and Chemical company and were stored at 5°C until used for the heavy metal analysis which was done also within few days after sampling.

The analysis of Zinc (Zn), Nickel (Ni), Copper (Cu), Chromium (Cr), and cobalt (Co) was determined using Varian atomic absorption spectrophotometer supplied (FAA240). Standard solutions for (Zn, Ni, Cu, Fe, Cr, Co) were prepared by dilution of the stock solution, and calibration curves for all metals were made using their standard solution. Accuracy of the analysis was checked by a periodic analysis of the standard solutions which showed good agreement within less than ±10 %.

4. Results and Discussion

4.1 Thermal Water

Generally, the concentrations of all analyzed metals were found to be low due to neutral pH of the water (pH 6.85-7.14). The dissolution and mobility of metals in natural water are greatly influenced by the (pH) (Hans-EikeGäble, 1997). The slightly alkaline thermal water enhances the precipitation of metals from the aqueous to the solid phase (Jiries et al., 2003)

A statistical summary of the concentrations of six heavy metals (Co, Zn, Cr, Cu, Ni) from the Afra thermal spring waters at the end of summer and winter seasons is presented in Table 1.

The average concentrations of heavy metals for Afra thermal springs at the end of the summer season were as follows: 99, 55, 41 ppb for Co, Ni and Cu, whereas Zn and Cr were below their detection limit. The average concentrations at the end of the winter season were 32, 25, 49, 50, 12, and 543 ppb for Co, Zn, Ni and Cu, respectively. The heavy metals' concentrations in Afra thermal water in ascending order varied with seasons. At the end of winter, the concentrations were Cu > Ni > Co > Zn >Cd, whereas at the end of summer, they were Co > Ni > Cu. The elements Cu and Zn are less reactive in water, but due to the thermal properties of the spring water with temperatures ranging from 36 to 46 °C, there is more reaction resulting in higher concentrations in winter compared to the summer season (Durowoju et al., 2016). As shown in Table 1, all of the analyzed heavy metals in Afra geothermal spring water fall within the WHO permissible level guidelines for drinking water except for Ni values, which are high in both of the winter and summer seasons.

Table 1. Statistical summary of heavy metals concentrations in ppb for Afra thermal spring during summer and winter season.

	Summer					Winter				
	Co	Zn	Ni	Cu	Cr	Co	Zn	Ni	Cu	Cr
Min	53	ND	40	28	ND	20	18	25	38	11
Max	148	ND	69	54	ND	46	33	70	62	13
Mean	99	ND	55	41	ND	32	25	49	50	12
STD	64	ND	16	15	ND	24	19	20	11	1
WHO Guidelines*	NA	3000	20	2000	50	NA	3000	20	2000	50

*ND: Not Detected, NA: Not available, * after UNEP GEMS (2006)*

Comparing the current results with those from other thermal springs worldwide (Table 2), it was found that the concentration of some heavy metals, such as Co, was much higher than those of other sites such as Limpopo-south Africa. As for Zn and Cr, the results showed higher concentrations than the thermal springs of Tulaz-Turkey and Limpopo-south Africa. The variation can be attributed to the different lithology and different temperatures which make the dissolution of heavy metals vary from one site to another.

Table 2. Heavy metal concentration in ppb of the investigated area compared with other thermal springs worldwide.

	Co	Zn	Ni	Cu	Cr	Reference
Limpopo-South Africa	1.13-3.5	8.65-37.54	4.43-17.33	1.14-6.07	2.85-5.25	Oliver et al. 2008
Main-Jordan	NA	95	58	70	571	Shakhatreh et al 2017
Tulza-Turkey	NA	8-292	NA	1-16	5-329	Baba et al. 2005
This work	32-99	ND-25	49-55	41-50	ND-12	

4.2 Soil

As far as soil is concerned, a statistical summary of heavy metal concentrations at two depths (0-10 cm and 10-20 cm) for soils irrigated with the Afra thermal water is given in Table 3. The average concentrations of the analyzed heavy metals in descending order were Cr > Zn > Co > Ni > Cu. The trend of the increased heavy metal concentrations in the soil was opposite to the trend of heavy metal concentrations of thermal springs at the end of the winter season. Some heavy metals which were found at high concentrations in the soil, such as Zn, were not detectable in the thermal water at the end of summer season; they were found at low concentrations at the end of winter season. This indicates the existence of other additional sources of heavy metals in the soil of the investigated site such as the mineralogical composition of the soil itself as indicated by the high Zn concentration in the control soil as shown in Table 3, whereas there is no remarkable anthropogenic activity in the area.

Table 3. Heavy metal concentration in ppb for soil irrigated by Afra thermal spring water.

		Heavy metal				
Depth		Ni	Cu	Zn	Cr	Co
0-10 cm	Min	160	146	198	200	181
	Max	211	246	450	777	254
	Mean	187	188	327	537	209
	STD	21	42	111	212	27
10-20 cm	Min	135	147	137	168	186
	Max	223	182	385	652	263
	Mean	190	163	257	523	215
	STD	36	17	94	209	31
Control Samples	Min	76	107	108	81	136
	Max	93	131	140	149	173
	Mean	81	117	129	131	143
	STD	9	12	16	35	20

Heavy metals concentrations found in the soil irrigated with Afra geothermal spring were the result of the accumulation from metals in the geothermal spring water and the soil pedogenesis. By comparing the amount of metals found in the soil with that from the control samples (Table 3 and Figure 2), it is noted that there is an increase in all metals in the soils irrigated with thermal springs compared to the control sample. This can be attributed to the accumulation of heavy metals from the waters of the thermal springs through successive irrigation. The trend of the increasing heavy metal concentrations in the soil is not similar to the trend of the thermal water concentrations indicating that pedogenesis is still the main factor controlling heavy metals in the soil as the accumulation of heavy metals through irrigation was not predominant.

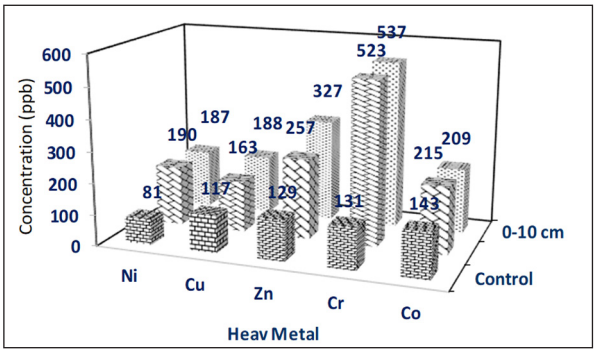

Figure 2. Heavy metal concentration in ppb for soil irrigated with Afra thermal water at two depths (0-10 cm, 10-20 cm and control sample)

The results of the present study show that the concentrations of heavy metals in the soil were relatively low which can be attributed to their low concentrations in the control samples as well as the thermal water.

5. Conclusions

The mean concentrations (C) of the studied metals in Afra thermal springs were in the following order: $C_{Cu} > C_{Ni} > C_{Co} > C_{Zn} > C_{Cd}$,. The mean values of metal concentrations were found to be lower at the control site compared with other sites

The data obtained in this study show that the increase in the heavy metal concentrations in soils irrigated by water from the Afra thermal springs was not significant. The concentrations of heavy metals result mostly from pedogenesis rather than from the accumulation through irrigation water.

The mean values of metal concentrations in the soil were found to be lower at the control site compared with the other sites. The results indicate that there was a substantial aerial deposition of the metals on the leaves, which was removed by the washing procedure. The presented results show that irrigation with Afra thermal water does not have any significant impact on heavy metal pollution in the soil.

References

Batayneh, A.T. (2010). Heavy metal in water springs of the Yarmouk Basin, North Jordan and their potentiality in health risk assessment, 5(7): 997-1003.

Ben Brahim, F., Makni, J., Bouri, S. (2013). Properties of geothermal resources in Kebilli region, Southwestern Tunisia. Environ Earth Sci., 69(3):885–897

Chiang, K., Chuan, K., Sheng, L. Lin, C., Chang, T., Wang M. (2010). Arsenic and lead (beudantite) contamination of agricultural rice soils in the Guandu Plain of northern Taiwan Journal of Hazardous Materials, 181(1–3): 1066–1071.

Durowoju, S., John, O., Georeges-Ivo, E. (2016). Variations of Heavy Metals from Geothermal Spring to Surrounding Soil and Mangifera Indica–Siloam Village, Limpopo Province Journal of Sustainability Volume 8, Issue 1.

Hans-EikeGäble, H. (1997). Mobility of heavy metals as a function of pH of samples from an overbank sediment profile contaminated by mining activities. J. of Geochem Expl., 58(2–3): 185-194.

Harahsheh, S.S. (2002). Curative tourism in Jordan and its potential development. MA Thesis, Bournemouth University.

Jiries, A., Hussein, H., Lintelmann, J. (2003). Polycyclic Aromatic Hydrocarbon in rain and street runoff in Amman, Jordan. J. of Environ Sci., 15(6): 848.

Katsanou, K., Siavalas, G., Lambrakis, N. (2012). The thermal and mineral springs of Aitoloakarnania Prefecture: function mechanism and origin of groundwater. Environ. Earth Sci., 65(8): 2351–2364.

Olivier, J., Niekerk, HJ., and Walt, I. (2008). Physical and chemical characteristics of thermal springs in the Waterberg area in Limpopo Province, South Africa. Water South Africa 34(2): 163-174.

Pasvanoglu, S., and Gultekin, F. (2012). Hydrogeochemical study of the Terme and Karakurt thermal and mineralized waters from Kirsehir Area, central Turkey. Environ. Earth Sci., 66(1): 169–182.

Salameh, E. and Rimawi, O. (1984). Isotopic analyses and hydrochemistry of the thermal springs along the eastern side of the Jordan Dead sea-Wadi Arab rift valley . J. Hydrol., 73: 129-145.

Salt, D.E., Blaylock, M., Kumar, N.P.B.A., Dushenkov, V., Ensley, B.D., Chet, I., Raskin, I. (1995). Phytoremediation: a novel strategy for the removal of toxic metals from the environment using plants. Biotechnology, 13: 468 –474.

Sawarieh, A. (2008). Thermal water resources in Jordan Geological Mapping Division - Geology Directorate Natural Resources Authority, Amman, Jordan.

Schaeffer, R., and Sass. (2014). The thermal springs of Jordan, Environ. Earth Sci., 72: 171–187.

Shakhatreha, M., Ali, K., Jacob, H., Emad, I., Hussein, Majed, M., Masadehd, Safwan, M., Obeidat, Abdul-salam, F., Juhmani, Mutaz, A., Abd Al-Razaq. (2017). Microbiological analysis, antimicrobial activity, and heavy-metals content of Jordanian Ma'in hot-springs water, Journal of Infection and Public Health.

Stauffer, R.E., Jenne, E.A., Ball, J.W. (1980). Chemical studies of selected trace element in hot spring drainages of Yellowstone national park, Geological Survey professional paper 1044-F. Washington, United State Government.

Tarawneh, K., Qtaitat, M.A., Mraiat, G., Jiries, A. (2000). Hydrochemical and bacteriological of the springs in Al-Tafileh region / south Jordan , Mu'tah lil-Buhuth wad-dirasat, 15: 25-46.

UNEP GEMS. (2006). Water quality for ecosystem and human health. Programme UNEP GEMS.

JJEES

JJEES (2019) 10 (3): 178-186
ISSN 1995-6681

Jordan Journal of Earth and Environmental Sciences

Estimating Lime Equivalence of Animal Manure Ashes and Soil Reaction Kinetics in Southwestern Nigerian Soils: An Incubation Study

Jamiu Azeez*, Olowoboko Blessing, Ajenifuja Debo, Oyegoke Olabisi

Federal University of Agriculture, Department of Soil Science and Land Management, Nigeria

Received 11 February 2019; Accepted 23 June, 2019

Abstract

In this study, the liming equivalence (LE) of manures and soil pH kinetics were computed in triplicates, for soil pH measurements after eight weeks of soil incubation using manure ashes and $CaCO_3$. The liming effects of $CaCO_3$ and manure ashes are related to their Ca content. The pH_{KCl} was more reliable for estimating the LE of the soil. The average LE was 0.73, 0.30, 0.26 for goat, cattle, and poultry ashes, respectively in pH_{KCl} and 0.22, -0.22 and 0.15 in pH_{water}. Generally, the estimated LE of the ashes was 0.58 in pH_{KCl} and 0.46 in pH_{water}. The goat manure ash had an LE value of 0.57, followed by the poultry manure ash value of (0.48); the least LE value (0.39) was found by the cattle manure ash. In alluvial soil, pH kinetics was best described by the power- function model (pH_{KCl}), while first-order and power-function models were most appropriate for soils amended with the poultry and cattle manure ash, respectively in pH_{water}. In a sedimentary soil, no single kinetics model could be used to describe the changes in soil pH. The liming equivalence of the ashes was (0.58) in pH_{KCl} and (0.46) in pH_{water}. Their liming equivalences relative to $CaCO_3$ were 57, 48 and 39 %, for goat, poultry and cattle manure ash, respectively. Conformity of the soils to the kinetics model is a function of the solution (electrolyte) used for the pH estimation.

Keywords: soil acidity, calcium carbonate, lime equivalence, manure ash.

1. Introduction

The agricultural productivity of acidic soils is usually characterized by a large number of limitations such as the adverse impacts on the proliferation of soil microbes, fixation of soil nutrients, and the growth retardation and death of plants. The effects of acid rain, aluminum hydrolysis, the application of acid-containing or acid-forming fertilizers to soil acidification are enormous (Fernandez-Calvino and Baath, 2010; Lege, 2012). The most limiting crop-growth factors in acidic soils are the Al and micronutrients' toxicity and the low Ca uptake by plants (Adams, 1984). Consequently, the usage of acidic soils in agriculture is only limited to the cultivation of crops adaptable to high soil Al and micronutrients (Whalen et al., 2002). The widely used options to tackle soil acidity include the application of lime to increase the low pH in the soil. Several minerals and at times synthetic soil-liming materials ($CaCO_3$, CaO, $Ca(OH)_2$, slag, etc.) have been recommended for usage in developed countries with a noticeable success in agricultural yield improvement of the crops. In fact, because of its strong liming potential, $CaCO_3$ has been recommended for use as a standard and reference liming material for evaluating other liming materials (Adams, 1984; Mokolobate and Haynes, 2002; Olowoboko et al., 2018).

The socioeconomic situations of farmers in sub Saharan Africa have forced them to rely solely on the use of ashes from the residue of their burnt bushes as lime. The population explosion in this part of the world has not only made the practice of shifting cultivation impossible, but has also made fallow periods very short, with the subsequent low bush biomass at the end of the short fallow periods. This will invariably produce a low biomass yield and ashes after burning. To a large extent, this has made the problem of soil acidity persistent because of the low ash input, being not enough to neutralize the soil acids.

The practice of organic agriculture and the huge amount of animal waste generated in sub Saharan Africa have made the use of animal manures a relatively cost-effective option in replenishing lost soil nutrients (Sajal and AbulKashem, 2014). Animal manures fertilize the soil and also reduce soil acidity (Mokolobate and Haynes, 2002). Theories have been postulated to explain the liming effects of manures, such as those confirmed by Azeez and Van Averbeke (2012). The effects included proton consumption by functional groups associated with the organic materials (Wong et al., 1998), proton consumption during decarboxylation of organic acid anions which occur during decomposition (Yan et al., 1996), specific adsorption of organic molecules by ligand exchange with the release of OH^- (Hue et al., 1986), and the release of OH ions during reduction reactions associated with localized anaerobic microsites. Moreover, Eghball (1999) and Whalen et al. (2000) maintained that the liming effects of animal manures are essentially attributed to their calcium carbonate and organic acid contents. These gains, however, are not fully enjoyed by farmers because their use of animal manures is restricted because of its low-nutrient concentration and its

* Corresponding author e-mail: azeezjo@funaab.edu.ng

high bulkiness, which at times become worrisome to farmers who lack resources and would rather prefer to cultivate their fields without any amendments.

A new option to the use of animal manures is to burn the manure at suboptimal temperatures to generate ashes (Komiyama, et al., 2013; Olowoboko et al., 2018). Manure ashes are concentrated plant nutrients with a high potential to lime acidic soils. Some studies (unpublished data) have evaluated the agronomic potentials of the use of animal manure ashes, but none has estimated the potential liming effects of these ashes and the changes in their liming value with time, in comparison with the standard reference $CaCO_3$. Hence, this study hypothesizes that based on their Ca content, manure ashes will have an equal liming potential and soil pH dynamics to that of the standard reference $CaCO_3$ lime. Accordingly, the objectives of this study are to compute the lime potential of three animal manure ashes, and evaluate the kinetics of the soil pH as a result of the addition of the manure ashes in an incubation study.

2. Materials and Methods

2.1 Soil and Manure Sample Collection and Preparation

Soil samples with acidic (low pH) reaction were collected at a depth of 0 – 15 cm from two different geologic backgrounds. The samples included: (a) an alluvial soil from Epe and (b) a sedimentary parent material soil from Ijale-papa. The two soil locations are both in the Ogun state, in southwest Nigeria. The collected soil samples were air-dried and screened with a 2 mm sieve.

Poultry, goat and cattle manures were collected from the animal farm of the Federal University of Agriculture Abeokuta, Nigeria. The manures were air-dried to a constant weight, then the dried samples were combusted to make manure ashes; the temperature of ashing was determined using an infrared thermometer. The conditions of ashing the manures were earlier reported by Olowoboko et al. (2018).

The poultry (birds) from which the litter without bedding materials was collected were raised in an intensive system of battery cages. They were layer birds provided with all the adequate nutritional and medical care needed. As for the ruminants, the goats and cattle were semi-intensively managed. The pure litters were collected from the animal pens. The animals scavenge for browse plants and grass outside their pens during the day, and stay in shed at nights in their different pens. The feces they produce overnight were then collected, processed, and used for the study as mentioned earlier. The animals consisted of a mixture of matured young males and females.

2.2 Soil and Manure Analyses

The collected soil samples were analyzed for the following properties: Soil pH was estimated in a 1:2 soil: water and KCl solution (for incubated soils) using a glass electrode pH meter (Orion Research Model 201), and the particle-size analysis was done using the hydrometer method (Bouyoucos, 1965). Exchangeable bases were extracted with 1 N ammonium-acetate solution in 1:10 soil: solution ratio. Potassium and sodium were analyzed with a flame photometer, while Ca and Mg were measured with atomic absorption spectrophotometry (Anderson and Ingram 1993). The available P and N were determined by the Bray 1 and micro-Kjeldhal methods respectively. The soil organic matter was determined using the chromic acid oxidation procedure of Walkley and Black (1934) method.

The manure ashes used were digested with nitric and perchloric acids at the ratio of 2:1 (Watanabe et al. 2013), and the digests were analyzed for exchangeable bases according to aforementioned methods. Distilled water was used for extraction to determine the pH of the manure ashes.

2.3 Experimental Design

The study was essentially an incubation experiment arranged in a completely randomized design.

The treatments were replicated thrice and included: control, cattle manure ash, goat manure ash, poultry manure ash, calcium carbonate (standard), all applied at 2.5, 5, 10, 15 and 20 t ha^{-1}.

2.4 Laboratory Incubation

Two-hundred grams of the air-dried soil samples sieved with a 2-mm mesh were dispensed into each incubation plastic container (300 cm^3 capacity) assuming that the mass of furrow slice soil is 2240 t ha^{-1}. Treatments were applied separately in each incubation plastic container and were mixed. The soils and treatment mixtures were watered at a field capacity to initiate microbial activity/mineralization, and were kept in a dark cupboard for eight weeks. The average temperature of the incubation cupboard was 26.5 °C. Soil samples were subsequently taken at 0, 2, 4, 6, and 8 weeks after the treatment incorporation and were analysed for pH in water and calcium chloride ($CaCl_2$).

2.5 Estimation of the Lime Potential of the Manure Ashes

This was estimated by plotting the graph of the values of the soil pH against the corresponding amounts of the amendments (manure ashes and $CaCO_3$). The slope of the equation generated from the linear graph was used as a measurement of the responsiveness of the soil pH values to the addition of ashes and $CaCO_3$ (Figures 1 and 2). Using calcium carbonate as a standard and as a reference-liming material, the slope of the lines generated for each of the amendments were then compared with those of the corresponding $CaCO_3$ treatments. This calculation was used to generate a parameter referred to as 'Lime equivalent' (LE). This parameter was obtained from soil pH data measured from pH in water and KCl. For example, two weeks after incorporating (2 WAI) the ash, the LE of the cattle manure ash, for soil pH measured in water was as follows:

$LE_{(water)(2WAI)}$ = slope of graph of cattle manure $ash_{(2WAI)}$ /slope of the graph of $CaCO_{3\,(2WAI)}$. . . . . .(Eq. 1).

The LE values were then computed for soil pH measured after 0, 2, 4, 6, and 8 weeks of the incorporation of the manure ashes to the two soils, for soil pH measurements in water and KCl.

2.6 Estimation of pH Kinetics Model

The pH kinetics was estimated with first-order, second-order, and power-function equations described by Dang et al. (1994) and reported by Azeez and Van Averbeke (2010).

First-order Equation:

$$ln\ Qt = ln\ Qe - k_1 t$$

k_1 is the first-order rate constant (pH^{-1}), Qt is the changes in pH after t days, Qe is the value of pH at equilibrium, and t is the time ($^{-1}$ day).

Second-order Equation:

$1/Qt = 1/Qe + k_2t$

k_2 is the second-order rate constant ($(pH^{-1})^{-1}$), Qt is the changes in pH after t days, Qe is the value of pH at equilibrium, and t is the time ($^{-1}$ day).

Power-function Equation:

$Qt = at^b$

A is the initial pH release rate constant (pH^{-1} day^{-1}), b is the release rate coefficient ($(pH^{-1})^{-1}$), and t is the time ($^{-1}$ day).

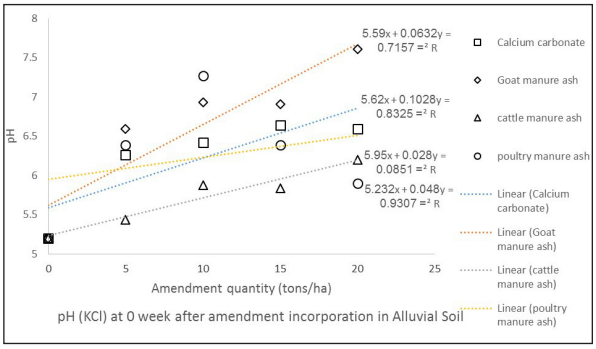

Figure 1. Typical soil pH changes in response to amendment application

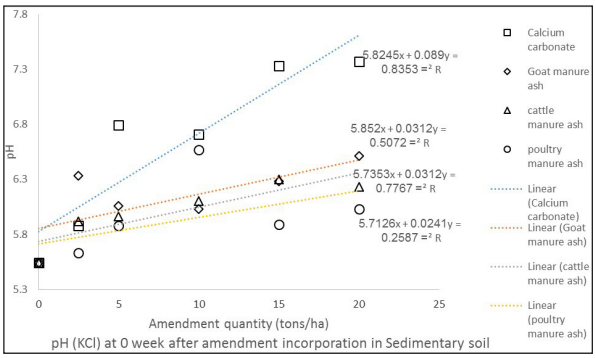

Figure 2. Typical soil pH changes in response to amendment application in sedimentary soil.

2.7 Statistical Analysis

The data collected were subjected to analysis of variance (ANOVA) using statistical analysis system (SAS, 1999). Significant treatment effects were separated using LSD at a 5 % level of probability.

3. Results and Discussion

3.1 Some Properties of the Soils and Manure Ashes Used for the Experiment

Some of the chemical analyses of soils and manure ashes used for the experiment are shown in Table 1. The textural class of both soils were sandy. It is observed that the two experimental soils were acidic in reaction, with very low exchangeable cations. With these pH values, there is the likelihood of micro-nutrient toxicity and low crop performance. Liming is probably the only option that could be used to ameliorate the problems. The soil nitrogen and organic carbon were also low. As expected, the manure ashes were high in pH and cations. Poultry manures had the highest Ca and Mg, followed by goat manure and the least Ca and Mg values were found in the cattle manure. The liming efficacy of these elements is expected to be high in the soils. Similar high amounts of the cations in manure ashes have been reported by Olowoboko et al. (2018). They also reported that the metallic contents of manure ashes are usually higher than the amounts in their respective unashed manure samples. The differences in nutrients in the manures could be attributed to the factors that had influenced the qualities of the manures; such factors include the differences in animal type, age, diet, and management system (Chadwick et al. 2000). The basic pH in the ashes is probably due to the concentration of the basic cations at ashing. The conversion of biomass to ash has been reported to increase cations and other nutrient elements by Lal and Ghuman (1989). Calcium and magnesium salts are added to the feed as additives for body osmotic balance, building of bones, and egg production in poultry (layers) production (Azeez and Van Averbeke, 2010a); this could be the rationale behind the high content of calcium and magnesium in poultry manure ash.

Table 1. Some chemical analyses of soils and manure ashes used for the experiment

	pH	Ca	Mg	Na	K	Al+H	Total N	Org. C
Soil		**Cmol(+) kg^{-1}**					**%**	
Epe	6.09	2.23	0.50	0.93	0.24	0.08	0.09	0.13
Ijale papa	5.66	2.52	0.82	0.83	0.29	0.07	0.11	1.25
Manure ash		**%**					**%**	
Poultry	10.14	13.43	4.60	1.16	3.32	-	2.58	4.67
Goat	10.48	5.08	3.19	1.39	3.02	-	3.11	5.61
Cattle	11.65	4.68	2.85	1.77	3.63	-	2.79	4.06

3.2 Effect of Manure Ashes and $CaCO_3$ on the Changes in Soil pH Values

Figures 3 and 4 show the changes in soil pH values measured in water and KCl, respectively, with the application of manure ashes and $CaCO_3$ to alluvial soil.

Generally, the addition of $CaCO_3$ to soil (Figure 3) increased the soil pH (water) significantly, except at the application rate of 5 tons/ha. On the other hand, the application of the manure ashes has an erratic pattern of response. For most of the incubation period, the ashes resulted in lower soil pH values compared with the control treatments. This might be due to the leaching of the ashes from the soil or temporary sage of the cations by soil microbes. Cattle manure ash application at 15 and 20 tons/ha and goat manure ash at 15 tons/ha were the only ash treatments that had liming effects on the soils. All the poultry manure ashes were observed to acidify the soil, compared with the control soil.

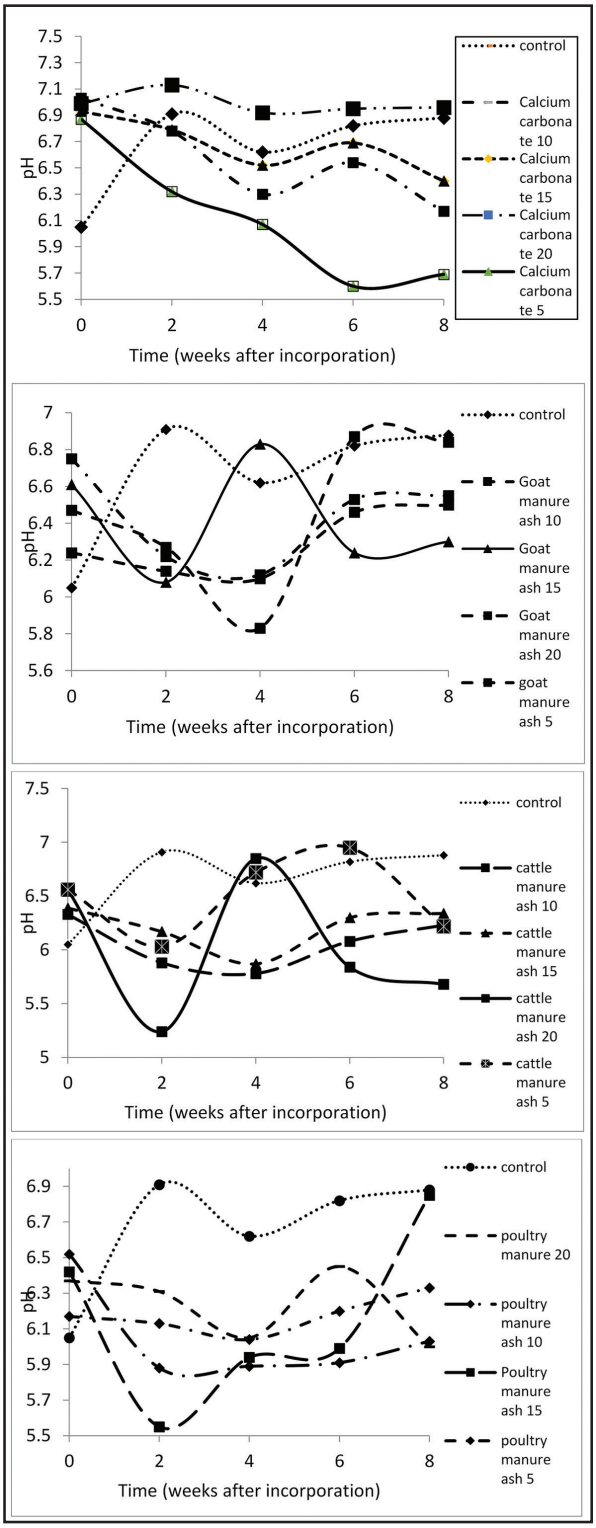

Figure 3. Changes in soil $pH_{(water)}$ with the application of manure ashes and lime in alluvial soil

As shown in the Figure 4, the pH measurement in KCl depicts that the effect of $CaCO_3$ in liming the soil was more pronounced for most of the period under investigation. The application of the lime at all rates resulted in higher soil pH values $_{(KCl)}$ than the control soil except at 2WAI. It was also observed that all the manure ashes limed the soil at inception and at later parts of the incubation period with the exception of soils amended with the poultry manure ash. It was also observed that the soil pH (KCl) was highest in all treatments weeks after the incorporation of all the amendments. Generally, the response pattern of soils treated with manure ash is similar to some minor outliers.

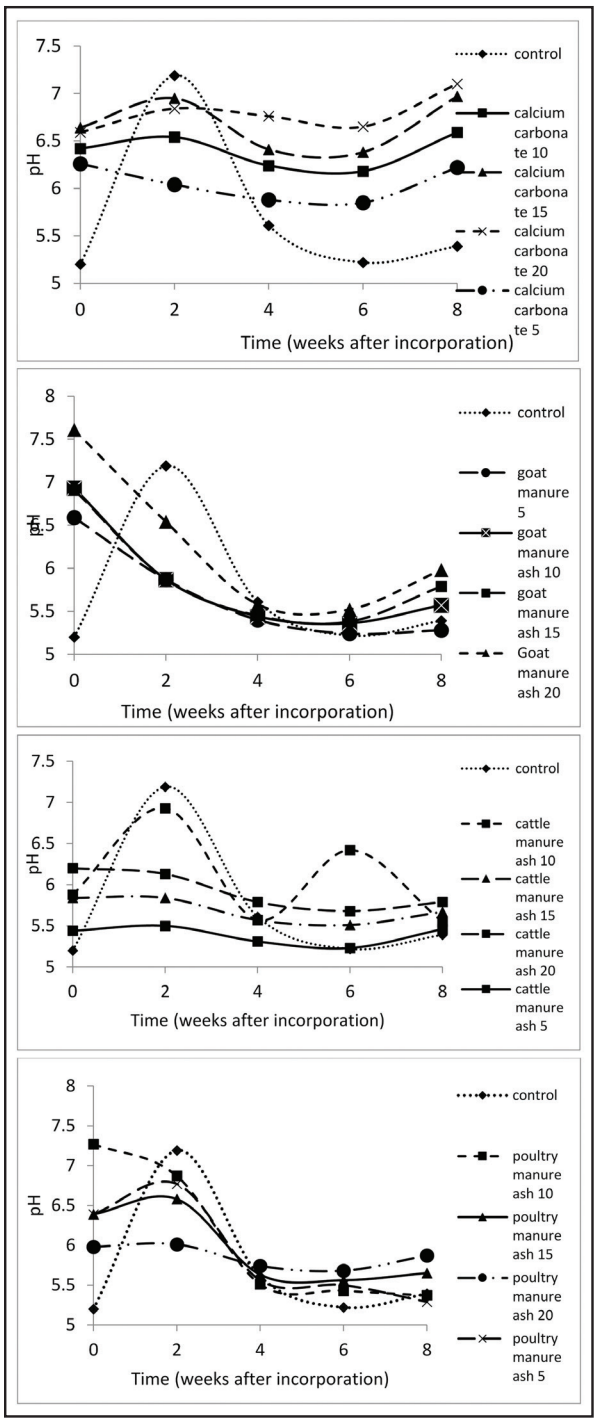

Figure 4. Changes in soil $pH_{(KCl)}$ with the application of manure ashes and lime in alluvial soil

Figures 5 and 6 show the changes in soil pH values measured in water and KCl, respectively, with the application of manure ashes and $CaCO_3$ to sedimentary soils. In Figure 5, it was observed that lime and the manure ashe application significantly increased the soil pH water. In all the ashes, and that application of 10 tons/ha and above had a significant increase in the soil pH. It was also observed that for most of the pH values, the initial soil pH peak was observed at 2 WAI. In soils treated with cattle and poultry manure ashes, the initial high pH at 2WAI was not sustained, and there

was a gradual reduction in soil pH with the increase of the incubation time, though, pH values remained higher than the control for most of the rates considered. In soils treated with goat manure ash, the pattern seems erratic, irrespective of the manure ash rates applied.

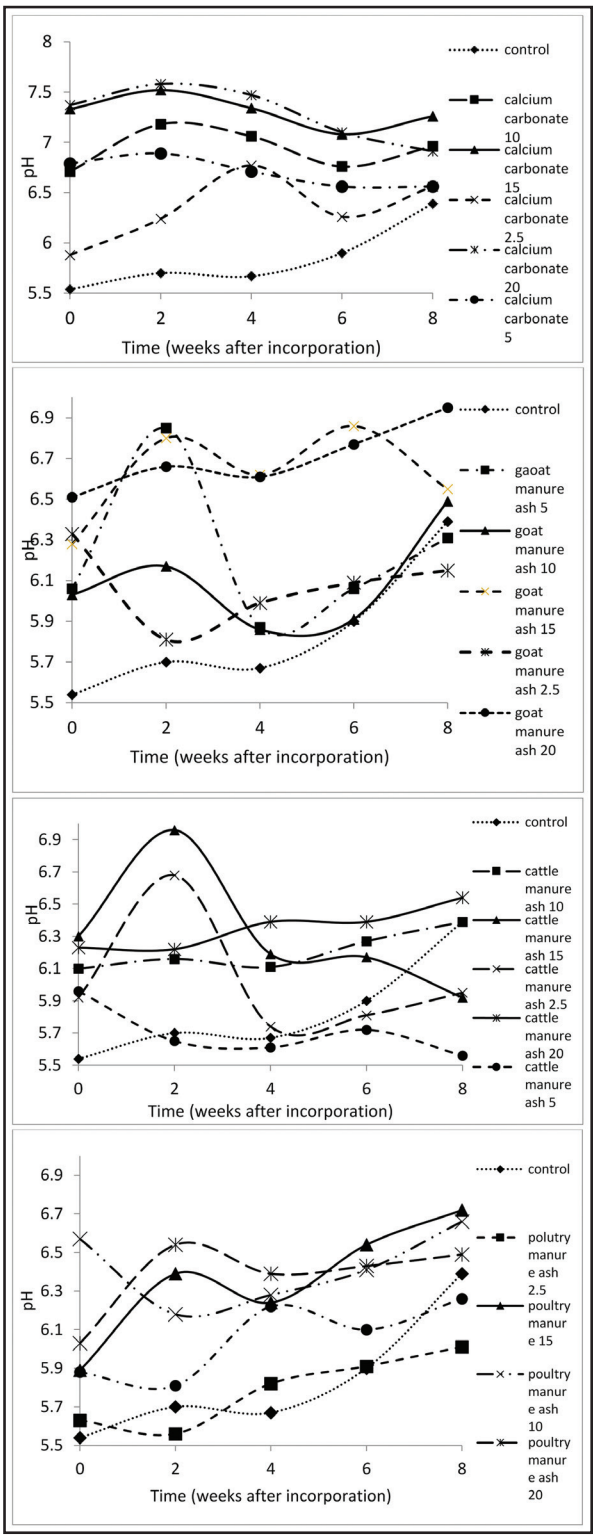

Figure 5. Changes in soil pH $_{(water)}$ with the application of manure ashes and lime in sedimentary soil

The pattern observed for soil pH $_{KCl}$ (Figure 6) was also inconsistent. The application of lime and the ashes increased the soil pH. However, there were two peaks in the graphs, at 2 and 6 WAI. Irrespective of the manure ash rates (except in 5 tons/ha cattle manure), their application significantly limed the soils. The differences observed between the soils might be a reflection of their parent materials and the initial soil pH values.

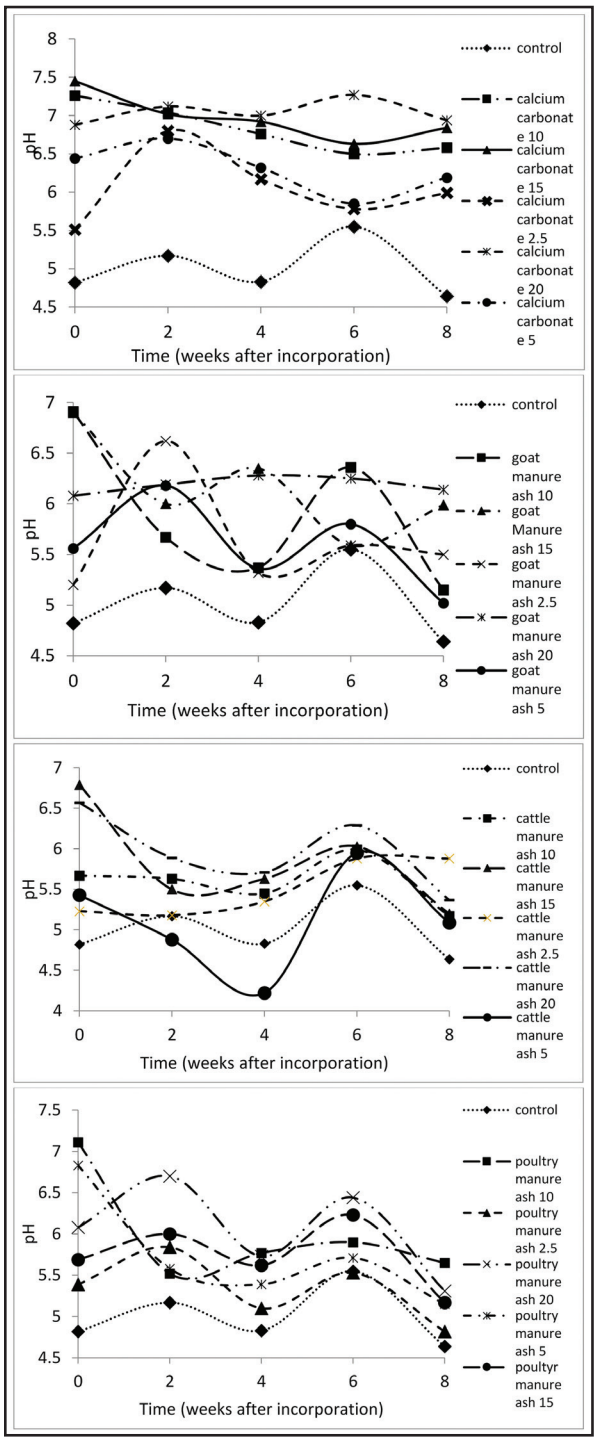

Figure 6. Changes in soil pH $_{(KCl)}$ with the application of manure ashes and lime in sedimentary soil

The $CaCO_3$ and the manure ashes applied limed the soil. This liming effect is closely related to the Ca contents of the amendments. The ashes have high amounts of Ca and Mg that are noted for soil liming. Their content, however, might not be a guarantee for liming, particularly if the cations are not bioavailable or soluble enough to neutralize and displace the Al and H content from the soil colloidal surfaces. The pH in KCl seems more reliable, since most of the H in the

exchange sites are displaced by the K in solution, which is the reason for the uniformity in pattern. However, this might not be possible in the pH measured in distilled water. Two weeks seem critical in the measurement of the liming effects of the amendments. Microbial-mediated reactions with the manure ashes most likely reach equilibrium stability at two weeks. This time duration seems critical for microbial-mediated processes in the soil. Azeez and van Averbeke (2010b) also reported that two weeks is critical for the release of nutrients from manure-amended soils in South Africa.

The pattern of liming differs among the different manures and their ashes. This could be a reflection of the feeding pattern of the animals and the management practices employed in the raising of the animals. The poultry manure used for the study is taken from layer birds raised intensively using a battery cage system. The cattle and goat manures were sourced from animals that scavenge (open grazing) during the day, but stay in shed at nights. The manures were collected from the open sheds. Additionally, the birds were fed with compound feeds in which the nutrient requirements of the birds are adequately met, while the ruminants scout for browse plants daily. These could have affected the manural quality of the animal wastes, and hence, their cation contents. This will invariably affect their liming effectiveness when used raw as manure or when applied as ashes.

3.3 Kinetics of Soil pH after Incorporation of Manure Ashes and $CaCO_3$

The parameters estimates of the equation employed in describing the soil pH kinetics in alluvial and sedimentary soils with and without amendments are shown in Tables 2 and 3 with the R^2 used as the criteria to determine the best equation for describing the changes in soil pH with time. Table 2 shows that for pH_{water} of the alluvial soil, the first-order equation was able to capture the changes in soils amended with poultry manure ash, while the power-function equation was preferred for soils amended with cattle manure ash. This implies that changes in pH with the increasing of time followed solely a linear pattern with the addition of poultry manure ash, while the addition of cattle manure ash allowed a nonlinear increase or decrease in pH as the weeks progressed. Soil amended with calcium carbonate (5t/ha, 10t/ha) and goat manure ash (15t/ha and 20 t/ha) had their pH following a curvilinear pattern with the increasing of weeks. This means that these pH changes were not consistent with time, and the fluctuations in pH were a result of soil and amendment characteristics. This is agreement with the findings of Abbasi et al., 2007 who observed inconsistency (increased or decrease with time) in the pattern of total mineral N of three organic manures in an incubation experiment. The type of the extracting solution affected the kinetics of pH, since they differ with varying extracting solutions. pH changes in almost all of the amended soils were inconsistent, and, hence, followed a nonlinear pattern. This is seen as they were best described by the power-function kinetics model, no plausible scientific reason is adduced for this. Soils amended with poultry manure ash at 15t/ha and 5t/ha and the cattle manure ash at 10t/ha had the second-order equation as the best model for expressing the pH kinetics. However, in the control soil, the first-order equation was preferred signifying linear changes in pH with time. The highest and lowest R^2 among others for pH_{water} were observed in power-function model as 0.943 (calcium carbonate 5t/ha) and in first-order equation as 0.009 (cattle manure ash 5t/ha) respectively. However, the power-function kinetics model showed the highest and lowest R^2 of 0.979 (goat manure ash 5t/ha) and 0.015 (calcium carbonate 10t/ha) in pH_{KCl}.

Table 2. pH mineralization kinetics of an alluvial soil applied with or without manure ashes and $CaCO_3$

	$pH_{(water)}$							$pH_{(KCl)}$						
	first order		Second order		Power function			first order		Second order		Power function		
Treatment (t/ha)	K_1	R^2	K_2	R^2	a	b	R^2	K_1	R^2	K_2	R^2	a	b	R^2
Control	0.012	0.487	0.003	0.49	6.181	0.053	0.698	0.012	0.084	0.003	0.076	5.776	-0.01	0.006
Calcium carbonate 10	-0.014	0.782	0.004	0.779	7.068	-0.05	0.807	0.000	0.000	0.00008	0.001	6.427	0.000	0.015
Calcium carbonate 15	-0.008	0.754	0.002	0.752	6.956	-0.03	0.746	0.000	0.001	0.000	0.001	6.676	0.000	0.000
Calcium carbonate 20	-0.001	0.213	0.000	0.214	7.036	0.000	0.13	0.006	0.431	0.000	0.428	6.595	0.02	0.385
Calcium carbonate 5	-0.024	0.899	0.007	0.901	6.918	0.000	0.943	-0.002	0.051	0.000	0.052	6.185	-0.01	0.209
Cattle manure ash 10	0.00008	0.00004	0.00005	0.000	6.161	-0.01	0.082	-0.009	0.099	0.003	0.103	6.199	-0.01	0.026
Cattle manure ash 15	0.000	0.000	0.00008	0.000	6.283	0.000	0.045	-0.005	0.482	0.001	0.476	5.865	-0.02	0.556
Cattle manure ash 20	0.009	0.067	0.002	0.056	6.325	-0.03	0.091	-0.01	0.751	0.003	0.747	6.245	-0.04	0.791
Cattle manure ash 5	0.001	0.009	0.000	0.008	6.435	0.005	0.008	-0.002	0.103	0.000	0.103	5.456	0.000	0.148
Goat manure ash 10	0.01	0.222	-0.002	0.203	6.259	0.021	0.073	-0.026	0.636	0.008	0.639	6.779	-0.11	0.97
Goat manure ash 15	-0.003	0.055	0.001	0.053	6.53	-0.01	0.067	-0.022	0.487	0.006	0.476	6.717	-0.1	0.88
Goat manure ash 20	0.000	0.002	0.000	0.0012	6.56	-0.01	0.104	-0.032	0.6	0.009	0.582	7.491	-0.13	0.813
Goat manure ash 5	0.006	0.519	-0.001	0.518	6.137	0.017	0.271	0.027	0.827	0.009	0.841	6.57	-0.11	0.97
Poultry manure 20	-0.004	0.231	0.001	0.23	6.382	-0.01	0.216	-0.004	0.357	0.001	0.353	6.7	-0.09	0.617
Poultry manure ash 10	-0.007	0.297	0.002	0.288	6.371	-0.03	0.593	-0.042	0.836	0.012	0.84	7.469	-0.15	0.862
Poultry manure ash 15	0.01	0.163	0.003	0.157	6.038	0.011	0.015	-0.02	0.672	0.006	0.676	6.57	-0.07	0.672
Poultry manure ash 5	0.003	0.333	0.000	0.327	6.115	0.006	0.12	-0.029	0.752	0.009	0.774	6.005	-0.01	0.425

In the sedimentary soil, (Table 3) the kinetics of pH in water and calcium chloride was not consistent among amendment rates since none of these kinetics models could solely describe the pH changes for any of the applied amendments. However, it was observed that the kinetics model was affected by the extracting solution used for the pH determination. This was noticed when the kinetics model that best captured the changes in pH_{water} was distorted when applied to the same amended soil in pH_{KCl}. The power-function model captured the changes only in soils amended with poultry manure at 20t/ha, 15t/ha and calcium carbonate at 2.5t/ha, 10t/ha, while a linear pattern described pH changes in soils amended with the cattle manure ash at all rates except 5t/ha for pH_{water}. pH kinetics in the control and in the soils amended with calcium carbonate were best described by the power-function model signifying a nonlinear response of soil pH as the weeks progressed whereas the first-order function was the best fit for cattle manure ash (2.5t/ha, 5t/ha and 10t/ha), goat manure ash (2.5t/ha) and poultry manure ash (10t/ha) in pH_{KCl}. Among all the kinetics' models, the highest and lowest R^2 were observed with first-order equation at 1.90 (cattle manure ash at 15t/ha) and with the power-function model at 0.08 (calcium carbonate at 10t/ha) respectively for pH_{water}. Conversely, in pH_{KCl}, the highest and lowest R^2 of 0.901 (cattle manure ash at 10t/ha) and of 0.008 (goat manure ash at 2.5t/ha) respectively were recorded. The rate constant of the second-order model (K_2) was positive for almost all of the amended soils while the rate constant of the first-order (K_1) and power-function (b) models had both positive and negative values. The wide variation in the rate constant of the manure ashes and calcium carbonate could be attributed to the differences in amendment characteristics.

Table 3. pH mineralization kinetics of a sedimentary soil applied with or without manure ashes and $CaCO_3$

	$pH_{(water)}$							$pH_{(KCl)}$						
	first order		Second order		Power function			first order		Second order		Power function		
Treatment (t/ha)	K_1	R^2	K_2	R^2	a	b	R^2	K_1	R^2	K_2	R^2	a	b	R^2
Control	0.016	0.823	0.005	0.835	5.444	0.05	0.615	0.000	0.000	0.000	0.001	4.921	0.01	0.016
Calcium carbonate 10	0.000	0.005	0.000	0.006	7.419	0.09	0.08	0.013	0.89	0.003	0.889	7.314	-0.05	0.901
Calcium carbonate 15	-0.004	0.333	0.001	0.33	7.419	-0.01	0.208	-0.011	0.703	0.003	0.701	7.42	-0.04	0.867
Calcium carbonate 2.5	0.011	0.426	0.003	0.441	5.934	0.0047	0.594	0.000	0.00008	0.000	0.01	5.85	0.022	0.058
Calcium carbonate 20	-0.009	0.651	0.002	0.651	7.547	-0.02	0.358	0.001	0.0075	0.000	0.076	6.93	0.011	0.195
Calcium carbonate 5	-0.005	0.751	0.000	0.754	6.87	-0.01	0.542	-0.01	0.458	0.003	0.462	6.595	-0.03	0.35
Cattle manure ash 10	0.005	0.787	0.001	0.787	6.06	0.017	0.574	-0.006	0.128	0.002	0.147	5.709	-0.01	0.077
Cattle manure ash 15	-0.0012	1.901	0.003	0.402	6.574	-0.03	0.204	-0.022	0.464	0.006	0.463	6.58	-0.09	0.602
Cattle manure ash 2.5	-0.006	0.113	0.001	0.112	6.13	-0.01	0.049	0.018	0.824	0.006	0.463	5.082	0.057	0.621
Cattle manure ash 20	0.006	0.885	0.001	0.885	6.179	0.02	0.713	-0.016	0.451	0.005	0.458	6.503	-0.06	0.502
Cattle manure ash 5	-0.006	0.543	0.002	0.544	5.91	-0.02	0.736	0.003	0.007	-0.001	0.005	5.155	-0.01	0.005
Goat manure ash 5	0.002	0.012	0.000	0.009	6.24	0.000	0.001	-0.013	0.29	0.004	0.306	5.822	-0.03	0.127
Goat manure ash 10	0.005	0.161	-0.001	0.151	5.989	0.012	0.064	-0.023	0.377	0.000	0.381	6.701	-0.09	0.493
Goat manure ash 15	0.004	0.177	0.001	0.183	6.392	0.025	0.398	-0.017	0.506	0.005	0.494	6.795	-0.07	0.648
Goat manure ash 2.5	0.000	0.002	0.000	0.001	6.17	-0.01	0.106	-0.002	0.008	0.000	0.004	5.554	0.009	0.007
Goat manure ash 20	0.007	0.867	0.002	0.869	6.47	0.024	0.727	0.01	0.124	0.000	0.126	6.112	0.008	0.347
Poultry manure ash 2.5	0.009	0.862	0.003	0.857	5.54	0.03	0.625	-0.013	0.353	0.005	0.367	5.603	-0.03	0.191
Poultry manure 15	0.014	0.816	0.004	0.809	5.903	0.053	0.85	-0.007	0.118	0.002	0.138	5.847	-0.01	0.052
Poultry manure ash 10	0.003	0.106	0	0.106	6.409	0.001	0	-0.019	0.376	0.005	0.359	6.767	-0.09	0.626
Poultry manure ash 20	0.006	0.407	0.001	0.412	6.119	0.029	0.64	-0.015	0.281	0.005	0.3	6.366	-0.03	0.137
Poultry manure ash 5	0.008	0.679	-0.002	0.678	5.81	0.029	0.507	0.027	0.629	0.008	0.641	6.649	-0.11	0.812

3.4 Changes in the Lime Equivalence of Manure Ashes with Time of Incorporation

The dynamics of the Lime equivalence (LE) values of the manure ashes are shown in Figures 7-10. The LE values of the ashes as measurements in soil pH (water) for the alluvial soil, shown in Figure 7, revealed that cattle manure ash (at 2, 6 and 8 WAI) and goat manure ash (at 6 and 8 WAI), actually acidify the soil compared with the effects of $CaCO_3$. However, for the soil pH in KCl (Figure 8), negative LE was only observed in soils amended with poultry manure ash at 2WAI. After the incorporation of the ashes, other week durations had positive effects on increasing LE, though this was not consistent with time. As shown in Figures 7 and 8, the average LE across weeks of investigation was highest with the goat manure ash (0.73), followed by the cattle manure (0.30). However, it was least with poultry manure (0.26) in pH_{KCl}. Their corresponding values are 0.22, -0.22 and 0.15, in pH_{water}.

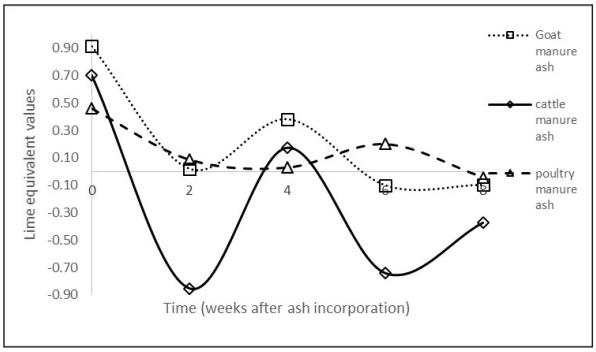

Figure 7. Changes in Lime Equivalent of manure ashes in alluvial soil, pH in water

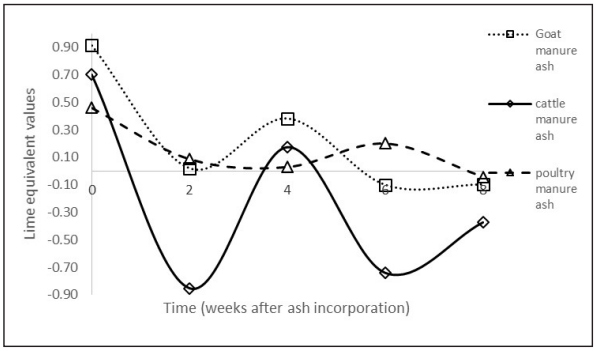

Figure 8. Changes in Lime Equivalent of manure ashes in alluvial soil, pH in KCl

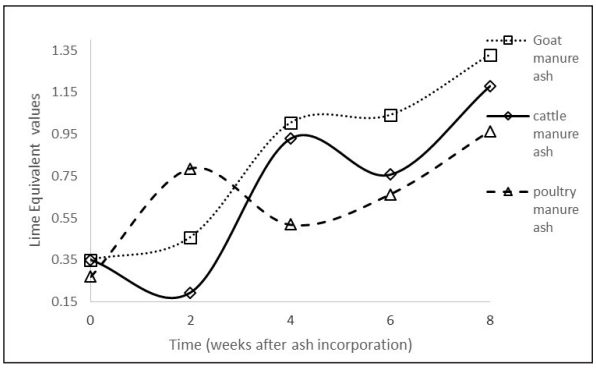

Figure 9. Changes in Lime Equivalent of manure ashes in sedimentary soil, pH in water

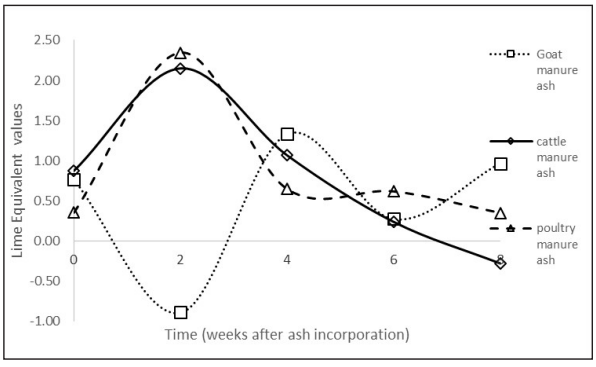

Figure 10. Changes in Lime Equivalent of manure ashes in sedimentary soil, pH in KCl

Lime equivalence for the ashes in the sedimentary soil estimated in pH_{water} is shown in Figure 9. It was observed that all the ashes had increased LE with the time of incorporation. The highest LE values were recorded at 8 WAI. The LE values are in the following order: goat manure ash (0.84) > cattle manure ash (0.68) > poultry manure ash (0.64). The pattern observed in Figure 10 shows that the LE of the ashes had its peaks at 2WAI for poultry and cattle manure ashes, while it was negative for the goat manure ash. The values increased for the goat manure ash, but they were reduced with time consistently concerning the other two ashes. The average LE values across the weeks of incorporation were 0.86, 0.81 and 0.49, for the poultry manure ash, cattle manure ash, and goat manure ash, respectively. The results recorded in the above figures signify that the manure ashes have the ability to lime the soil. However, the magnitude of their liming potential depends on the medium in which the soil pH is determined. It was generally observed that the LE of the ashes was higher with pH values recorded in pH_{KCl} (0.58) and lower in pH_{water} (0.46). Goat manure ash was also seen to have a consistently higher LE values irrespective of the media of pH measurement. Overall, goat manure ash has an LE value of 0.57. it was followed by poultry manure ash at (0.48) and the least LE value (0.39) was found for the cattle manure ash.

4. Conclusions

Manure ashes have a liming potential in comparison with conventional lime. Values of liming equivalence of the ashes were higher in pH values recorded in pH_{KCl} (0.58) and lower in pH_{water} (0.46). Their liming equivalence values are 57 %, 48 %, and 39 %, for the goat, poultry and cattle manure ash, respectively. In the alluvial soil, pH changes in almost all of the amended soils were best described by the power-function kinetics model in pH_{KCl}, while the first-order and power-function models were most appropriate for soils amended with poultry manure ash and cattle manure ash, respectively for $pH_{water.}$ However, in the sedimentary soil, pH kinetics was not consistent among amendment rates, as the kinetics models could not solely describe the pH changes for any of the applied amendments. The ability of pH-kinetics models to describe soil pH changes was dependent on the type of the extracting solution used for pH determination, which could, however, be verified on the field.

Acknowledgement

The authors wish to acknowledge the Soils of Forest Islands in Africa (SOFIIA-FUNAAB) for their support and assistance in the laboratory analyses. SOFIIA is a collaborative research project funded by the UK Government's Royal Society-DFID Africa Capacity Building Initiative. Opinions expressed and conclusions arrived at are those of the authors and are not necessarily to be attributed to the project.

References

Abbasi, M.K., Hina, M., Khalique, A., Khan, S.R. (2007). Mineralization of three organic manures used as nitrogen source in a soil incubated under laboratory conditions. Comm. Soil Sci. Plant Anal., 38: 1691–1711.

Adams, F. (1984). Soil Acidity and Liming, 2nd Edn., America Society of Agronomist, Crop Science Society of America and Soil Science Society of America, Madison, Wisconsin, USA,

Anderson, J.M., Ingram, J.S.I. (1993). Soil organic matter and organic carbon. In Tropical soil biology and fertility: A handbook of methods, 2nd Ed, p62–68. Oxford, UK: CAB International.

Azeez J.O, Van Averbeke, W. (2012). Dynamics of soil pH and electrical conductivity with the application of three animal manures. Comm. Soil Sci. Plant Analy., 43(6): 865–874.

Azeez, J.O., Van Averbeke, W. (2010a). Fate of manure phosphorus in a weathered sandy clay loam soil amended with three animal manures. Biores. Tech., 101: 6584–88.

Azeez, J.O., Van Averbeke, W. (2010b). Nitrogen mineralization potential of three animal manures applied on a sandy clay loam soil. Biores. Tech., 101: 5645–5651.

Bouyoucos, G.H. (1965). A calibration of the hydrometer method for testing mechanical analysis of soils. Agron, J., 43:434–438.

Chadwick, D.R., John, F., Pain, B.F., Chambers, B.J., Williams, J.C. (2000). Plant uptake of nitrogen from the organic nitrogen fraction of animal manures: A laboratory experiment. J. Agric. Sci., 134: 159–68.

Dang, Y.P., Dalal, R.C., Edwards, D.G., Tiller, K.G. (1994). Kinetics of zinc desorption from Vertisols. Soil Sci. Soc. Am. J., 58: 1392–1399.

Eghball, B. (1999). Liming effect of beef cattle feedlot manure or compost. Comm Soil Sci Plant Analy. 30 (19-20): 2563-2570.

Fernandez-Calvino, D., and Baath, E. (2010). Growth rate response of bacteria communities to pH in soils differing in pH. FEMS Microbiol Ecol., 73: 149-156.

Hue, N.V., Craddock, G.R., Adams, F. (1986). Effect of organic acids on aluminum toxicity in subsoils. Soil Sci. Soc. Am. J., 50: 28–34.

Komiyama, T., Kobayashi, A., Yahagi, M. (2013). The chemical characteristics of ashes from cattle, swine and poultry manure. J. Mat. Cycle Waste Manag., 15(1): 106-110.

Lal, R., Ghuman, B.S. (1989). Biomass burning in windows after clearing a tropical rain forest: Effect on soil properties, evaporation and crop yields. Field Crop Res., 22(4): 247–255.

Lege, B.N. (2012). Soil chemical properties as affected by phosphorus and nitrogen – based manure and compost application. Soil Conserv., 21: 411–416.

Mokolobate, M.S., Haynes, R.J. (2002). Comparative liming effect of four organic residues applied to an acid soil. Bio. Fertil. Soil, 35(2): 79-85.

Olowoboko, T.B., Azeez, J.O., Olujimi, O.O., Babalola, O.A. (2018). Comparative Evaluation of Animal Manures and Their Ashes on Soil pH and Electrical Conductivity in some Southwestern Nigerian Soils. Comm. Soil Sci. Plant Anal., 49(12): 1442-1454.

Sajal, R., AbulKashem, M. (2014). Effects of organic manures in changes of some soil properties at different incubation periods. Open J. Soil Sci., 4(3): 81–86.

SAS 1999. The SAS system for windows. Cary, NC: Release 8.0. SAS Inst.

Walkley, A., Black, I.A. (1934). An examination of Degtjareff method for determining soil organic matter and a proposed modification of the chromic acid titration method. Soil Sci., 37: 29-37.

Watanabe, P.H., Thomas, M.C., Pascoal, L.A.F., Ruiz, U.S., Daniel, E., Amorim, A.B. (2013). Manure production and mineral excretion in faeces of gilts fed ractopamine. Acta. Scient., 35(3): 267–272.

Whalen, J.K., Chang, C., Clayton, G.W., Carefoot, J.P. (2002). Cattle manure amendments can increase the pH of acid soils. Soil Sci. Soc. Am. J., 64: 962–966.

Wong, M.T.F., Nortcliff, S., Swift, R.S. (1998). Method for determining the acid ameliorating capacity of plant residue compost, urban waste compost, farm yard manure and peat applied to tropical soils. Comm. Soil Sci. Plant Analy., 29: 2927-2937.

Yan, F., Schubert, S., Mengel, K. (1996). Soil pH increase due to biological decarboxylation of organic anions. Soil Bio. Biochem., 28(4–5): 617–624.

المملكة الأردنية الهاشمية

صندوق دعم البحث العلمي

الجامعة الهاشمية

المجلة الأردنية
لعلوم الأرض والبيئة

JJEES

مجلة علمية عالمية محكمة

المجلد (١٠) العدد (٣)

http:// jjees.hu.edu.jo/

ISSN 1995-6681

المجلة الأردنية لعلوم الأرض والبيئة

مجلة علمية عالمية محكمة

المجلة الأردنية لعلوم الأرض والبيئة: مجلة علمية عالمية محكمة ومفهرسة ومصنفة، تصدر عن عمادة البحث العلمي في الجامعة الهاشمية وبدعم من صندوق البحث العلمي - وزارة التعليم العالي والبحث العلمي، الأردن.

ترسل البحوث إلكترونيا إلى البريد الإلكتروني التالي:

رئيس تحرير المجلة الأردنية لعلوم الأرض والبيئة

jjees@hu.edu.jo

لمزيد من المعلومات والأعداد السابقة يرجى زيارة موقع المجلة على شبكة الانترنت على الرابط التالي:

www.jjees.hu.edu.jo

المملكة الأردنية الهاشمية صندوق دعم البحث العلمي الجامعة الهاشمية

JJEES

المجلة الأردنية لعلوم الأرض والبيئة

المجلد (١٠) العدد (٣)

مجلة علمية عالمية محكمة تصدر بدعم من صندوق دعم البحث العلمي

ISSN 1995-6681 jjees.hu.edu.jo أيلول ٢٠١٩